Università degli Studi di Padova

DIPARTIMENTO DI FISICA E ASTRONOMIA 'GALILEO GALILEI'
Corso di Laurea Magistrale in Astronomia

Tesi di laurea magistrale

The peculiar SN 2013gc: evidence of an eruptive phase before the explosion

Candidato:
Andrea Reguitti
Matricola 1155354

Relatore:
Dott. Stefano Ciroi

Correlatore:
Dott. Andrea Pastorello

Anno Accademico 2017–2018

A mia nonna Enrica,
che ci vede da lassù

Sommario

Le supernovae di tipo IIn si osservano quando il materiale eiettato dall'esplosione incontra e interagisce con del materiale circumstellare circostante, depositato dal progenitore in precedenti episodi di perdita di massa. Lo spettro di questi oggetti presenta un continuo blu, con intense righe di Balmer, in particolare Hα. Il profilo delle righe è caratterizzato dalla contemporanea presenza di una componente larga, dovuta agli ejecta veloci, e di una componente stretta, proveniente dal vento lento. In questo lavoro abbiamo analizzato le curve di luce, di colore, assoluta e bolometrica e gli spettri di SN 2013gc, una supernova di tipo IIn peculiare. Una sorgente variabile è stata identificata alla posizione della supernova in immagini di archivio prese alcuni anni prima. La sorgente ha una magnitudine assoluta oscillante tra -10 e -12 mag, ed è interpretata come l'evidenza di una precedente fase eruttiva della stella massiccia che ha poi prodotto SN 2013gc. SN 2013gc è la prima supernova della classe IId in cui sono stati identificati episodi eruttivi antecedenti all'esplosione terminale del progenitore.

I capitoli 1 e 2 sono una breve introduzione sulla classificazione delle supernovae, sui 'Supernova impostors' e sugli ILOTs. Il capitolo 3 è una sintesi delle conoscenze attuali sulle supernovae di tipo IId, un sottogruppo delle IIn, di cui fa parte anche SN 2013gc. In esso presentiamo anche la fotometria e la spettroscopia inedite della supernova IId SN 2000P. In questo capitolo vengono riportate le informazioni sulla scoperta di SN 2013gc e sulle proprietà della galassia ospite. Il capitolo 4 presenta la strumentazione utilizzata e la tecnica di riduzione dei dati. Nel capitolo 5 vengono descritte la curva di luce, le curve di colore e la curva assoluta ottenute, che vengono confrontate con quelle di altre supernovae IId. Particolarmente importante è la sezione 5.4, ove sono presentate le evidenze osservative di una fase eruttiva, costellata da episodi di outbursts, del progenitore. Nel capitolo 6 si descrivono gli spettri della supernova, con particolare riferimento al profilo della riga Hα, mentre nel capitolo 7 illustriamo la curva di luce bolometrica di SN 2013gc, la determinazione della massa di ^{56}Ni prodotta, assieme alla discussione sui possibili scenari del progenitore e del meccanismo di esplosione. Infine, nel capitolo 8, illustriamo le nostre conclusioni. In appendice si riportano le tabelle con le misurazioni fotometriche di SN 2013gc ottenute.

Abstract

Type IIn supernovae occur when the ejected material from the explosion encounters and interacts with surrounding circumstellar material, produced by the progenitor in previous mass loss episodes. The spectra of these objects present a blue continuum, with strong Balmer lines, particularly Hα. The line profile is characterized by the simultaneous presence of a broad component, from the fast ejecta, and a narrow component, from the slow wind. In this work we analysed the light curves, the colour, absolute and bolometric curves, and the spectra of SN 2013gc, a peculiar IIn supernova. A variable source has been identified at the supernova position in archive images obtained a few years before. The source has absolute magnitude in the range -10 to -12 mag, and has been interpreted as the signature of an eruptive phase experienced by the massive star that later produced SN 2013gc. SN 2013gc is the first type IId event with pre-supernova outbursts observed before the terminal supernova explosion.

The chapters 1 and 2 are a brief introduction on the supernovae classification, on 'Supernova impostors' and on ILOTs. Chapter 3 is a summery of modern knowledge of type IId supernovae, a subgroup of type IIn. In this chapter we present also unpublished photometry and spectroscopy of the supernova SN 2000P. In this chapter, the informations about the discovery of SN 2013gc and the host galaxy properties are reported. Chapter 4 presents the instrumentation we used and the data reduction technique. In chapter 5, the light curve, the colour and absolute curves obtained are described, and are compared with those of other type IId supernovae. Remarkable is the section 5.4, where the observational evidence of an eruptive phase, studded with outbursts from the progenitor, are presented. In chapter 6, the supernova spectra are described, with emphasis on the Hα line profile, while in chapter 7 we illustrate the bolometric light curve of SN 2013gc, our estimate of the synthesised ^{56}Ni mass, along with the discussion on the possible progenitor and explosion mechanism scenarios. Finally, in chapter 8, we report our conclusions. The tables with the obtained photometric measurements of SN 2013gc are reported in the appendix.

Contents

Chapter 1

Introduction

A Supernova (SN) is the final, explosive end of the life of a massive star. Because its luminosity is much larger than that of a classical Galactic Nova, which has an absolute magnitude (M) fainter than -10, such a luminous event was labelled Super-Nova by Baade & Zwicky (1934). The high intrinsic brightness of these objects allows us to observe and study them also in external galaxies. The brightest SNe can exceed at maximum $M = -19$ mag and, for a short period (some weeks), they are as luminous as their host galaxies.

The total kinetic energy released by the SN is of the order of 10^{51} erg, about 1% of which is radiated. This energy is sufficient to expel the outer layers of the star with velocities of some 10^4 km s^{-1}. This generates a shock wave that propagates in the interstellar medium. The importance of SNe in the chemical enrichment of a galaxy is given by the fact intermediate to heavy elements, including iron-peak elements, are produced in the explosion.

After maximum, the SN begins to dim, and the expanding ejecta cool down. At later phases (months after the peak), the light curve is powered by the radioactive decay of heavy metals, in particular ^{56}Ni to ^{56}Co to ^{56}Fe. Then the expelled gas expelled becomes transparent, leaving behind a nebula, and eventually a compact core, i.e. a black hole (BH) or a neutron star (NS).

1.1 Supernova classification

The SN classification is based on the presence/absence of particular spectroscopic features. The first classification scheme, introduced by Minkowski (1941), was based on the identification of Hydrogen (H) lines: if Balmer lines were not visible in the spectrum, the SN was classified as a 'Type I' SN, otherwise the classification was 'Type II' SN. Type I SNe were further subclassified by Porter & Filippenko (1987), depending on the presence or

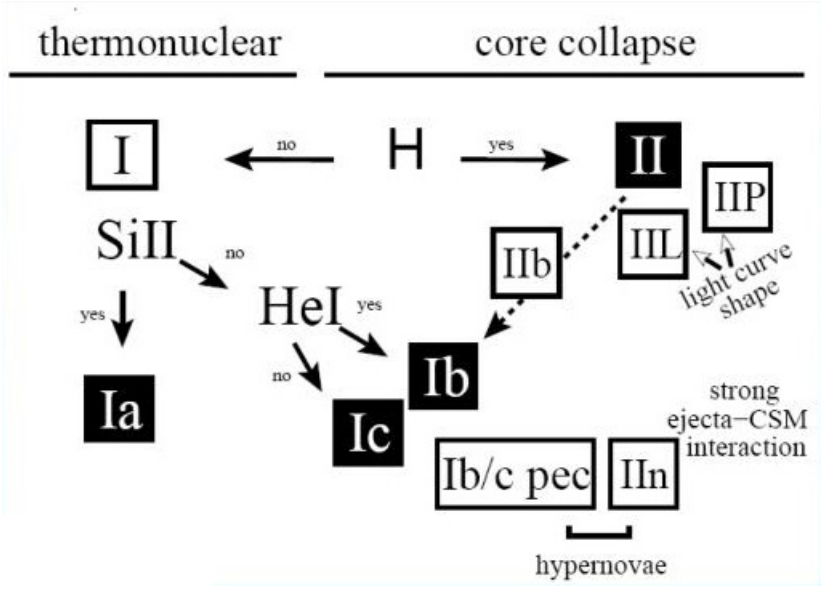

Figure 1.1: The general framework of SNe classification, from Turatto (2003).

not of the Si II λ6355 Å absorption line. If this line is present, the SN is classified as 'Type Ia', while if it is absent the SN is labelled as 'Type Ib'. The further classification as 'Type Ic' was introduced for SNe that also do not show Helium (He) lines in their spectra. Later on, type II SNe were splitted in II-L (linear) and II-P (plateau) types (Barbon, Ciatti & Rosino, 1979), based on the observed post-peak light curves evolution. Figure 1.1 reports the modern scheme of SN classification, while Fig. 1.2 shows typical spectra of different SN types, both at early and late phases.

The physical discrimination between a type Ia and other SN types (Fig. 1.1) is due to the different explosion mechanism.

- The type Ia SN class is homogeneous, with SNe having similar peak luminosities (around $M = -19.5$, Gibson et al., 2000) and spectral evolution. They are observed in all types of galaxies, from ellipticals (Barbon et al., 1999) to spirals and irregulars. When observed in spirals, their positions are not strictly associated with arms or star-forming regions, suggesting that the progenitors of type Ia SNe are members of old stellar populations. SNe Ia are the outcome of the thermonuclear runaway of a degenerate white dwarf (WD). In the single degenerate scenario, a Carbon-Oxygen WD in a binary system accretes material from an evolved star. The most natural candidates are red giants that have expanded beyond their Roche lobe. When the mass of the WD exceeds the Chandrasekar limit ($\sim 1.4 M_{\odot}$), the igni-

tion of Carbon burning triggers the complete destruction of the star, hence no compact remnant is left. Alternatively, a double degenerate scenario is also a plausible explanation: two WDs may merge, with the resulting mass exceeding the Chandrasekar limit. This may trigger the thermonuclear runaway (see Taubenberger, 2017, for a recent review on type Ia SNe).

- Differently, types Ib/c and II SNe are observed only in the arms of spiral galaxies, in the proximity of star forming regions (Barbon et al., 1999). This indicates that the progenitors are young, massive stars (M> $8M_{\odot}$, Smartt, 2009). Type II SNe are heterogeneous, due to diversity in age, chemical composition and final configuration of the progenitors. These explosions are the consequence of a core-collapse event. In the core of a massive star, the nuclear reactions continue until Silicon burns into Iron. When this happens, the gravity is no longer balanced by the radiation pressure, and the core collapses. The gravitational energy is released through a pressure wave, that kicks and heats up the outer layers, powering the so called '*Shock breakout*'. The collapsed core forms a compact degenerate object, which can be a NS or a BH, depending on the initial mass of the star, with very massive stars likely forming a stellar BH.

  It is believed that type II SNe, prior to the explosion, arise from red supergiant (RSG) stars that retain the outer envelope of Hydrogen before the explosion. These stars were originally OB main sequence stars that rapidly evolved towards the RSG phase. In both cases, stars may also be stripped via binary interaction.

  In some cases, the final outcome of binary interaction is a more stellar core totally stripped by Hydrogen. Type Ib are produced by Wolf-Rayet (WR) stars or lower-mass stars in binary systems, whose strong stellar winds have stripped away the Hydrogen envelope, leaving the He-rich layers beneath.

  Finally, type Ic SNe probably have He-poor hypergiants or WR stars as progenitors, that were stripped away by both the H and He layers (Smartt, 2009).

1.2 Type IIn Supernovae

The most interesting SN type for this dissertation was introduced in the early 90s. Type IIn SNe were defined by Schlegel (1990). Their spectra have a blue, almost featureless continuum, and are dominated at all epochs by intense narrow Balmer lines in emission, with Hα being the most prominent feature. The profile of these lines is composite, usually formed by a narrow

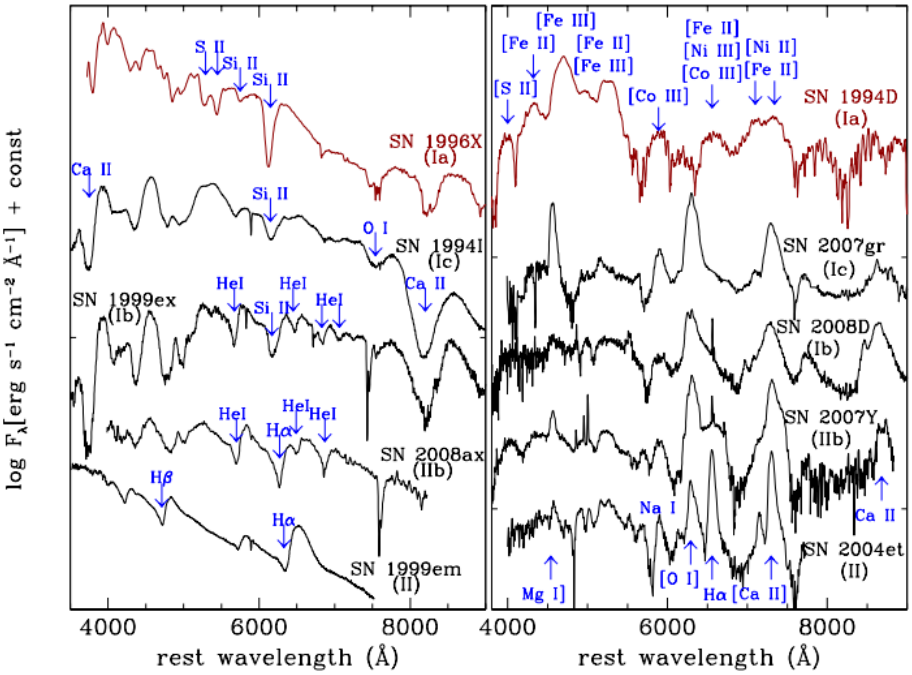

Figure 1.2: Comparison of spectra of different SN types. Left: photospheric spectra. Right: nebular spectra, from Pastorello (2012).

component with full width at half maximum (FWHM) velocities from a few tens to a few hundreds km s^{-1}, superimposed on broader components. The label "type IIn" is due to the remarkable and ubiquitous predence of "narrow" emission lines. Sometimes narrow P Cygni components are visible in absorption, signature of an expanding absorbing H-rich gas shell. Lines of He, Ca II, Na, O (permitted and forbidden) and Fe II can also be found in SN IIn spectra.

A reference object for this class is SN 1988Z (Stathakis & Sadler, 1991; Turatto et al., 1993; Aretxaga et al., 1999), whose spectra always show well-visible lines of the Balmer series. At early phases Hα dominates the spectra, and is characterized by 3 components: broad, intermediate-width and narrow, while absorption components are not detected. After one year, Hα is no longer detectable.

The light curves of IIn evolve slowly with respect to normal SNe II, and there is a very modest color evolution. In addition, the luminosity decline at late phases is slower than that predicted for the radioactive decay of ^{56}Co into ^{56}Fe.

The typical absolute magnitude at the maximum is quite high ($-17 \lesssim$

$M_B \lesssim -19$ mag; Richardson et al., 2014). However, the observed range of magnitudes for SNe IIn is much wider: the faintest objects have an absolute magnitude in V of -16 mag, while the brightest can reach -22 mag. The latter are the so called 'Super-luminous' SNe II (SLSNe, Gal-Yam, 2012; Moriya et al., 2018). Traditional powering mechanisms are no longer adequate to explain these extreme SNe. Examples of SLSNe II are SN 2008am (Chatzopoulos et al., 2011), SN 2006gy (Smith et al., 2007) and PS1-10adi (Kankare et al., 2017).

The shape of the light curve after the early phases is very heterogeneous in SNe IIn. If the post-peak light curve shows a plateau phase, the object is labelled as IIn-P (Fraser et al., 2013b; Mauerhan et al., 2013b), while if a linear decline in luminosity is observed, the SN can be labelled IIn-L (Taddia et al., 2015). In type IIn-P SNe, the plateau allows the object to remain visible for a longer time. The plateau can be linked to a diluted diffusion time of photons or a longer H recombination time scale.

An example of SN IIn-P is SN 2011ht (Fraser et al., 2013b; Mauerhan et al., 2013b). The rise to the maximum was followed by a plateau in the optical bands[1], that lasted ∼120 days. After the plateau, the light curve faded by many magnitudes in ∼10 days. The decline was steeper in the optical bands than in the infrared. The mass of the progenitor is estimated to be 8-10 $M_\odot$ (Mauerhan et al., 2013b), and the electron-capture (EC) mechanism was proposed. This can explain also the relatively modest SN luminosity, having at maximum an absolute magnitude $M_V = -17.4$ mag. We note, however, that this interpretation is controversial (see e.g., Roming et al. (2012) and Humphreys et al., 2012).

SN 2008am reached at maximum an approximate absolute magnitude -22.3 mag and a peak luminosity of $\sim 3 \times 10^{44}$ erg s^{-1}, making it one of the most powerful SNe ever observed. SN 2006gy also was a very bright SN, reaching $M_V = -21.7$ mag. The event was observed in the X-rays with the *Chandra* observatory, and the SN was of the same luminosity as the host galaxy. It was initially proposed to be a Pair-Instability Supernova (PI SN, Smith et al., 2007), but more canonic explanations were later on offered by Agnoletto et al. (2009). PI SNe is predicted to be the end-point of life of very massive stars (at least 130 $M_\odot$), where γ-rays generated in the core can be so energetic to produce electron-positron ($e^- e^+$) pairs. This particle-antiparticle production subtracts energy to the radiation field. Consequently, the radiation pressure decreases and the upper layers of the star collapse under their own gravity. The collapse ignites thermonuclear runaway reactions, powering the first-light shock. The star material is then violently expelled. The runaway is so efficient that no compact residual (NS or BH) is left. Instead, many solar masses of ^{56}Ni and other heavy elements are ejected. Remarkably, many type IIn SLSNe occur in low-metallicity

[1] No plateau is visible in the UV domain

galaxies (Heger et al., 2003). Low metallicity of the star inhibits the mass-loss, and it is kept massive. The very high mass needed to trigger the Pair-Instability processes suggests that massive luminous blue variable stars (see Chapt. 2) are viable progenitor candidates. After the initial peak of SN 2006gy, the powering source maintaining the luminosity to high values (about $M_R = -21$ mag) can be circumstellar material-ejecta interaction (Mauerhan et al., 2013b). Another possible mechanism, in case of PI SN explosion, is the ^{56}Ni decay to ^{56}Co and ^{56}Fe. Large ^{56}Co masses can power the SN high luminosity up to late phases (Smith et al., 2007).

Type IIn SNe are produced when a supernova explodes in a H-rich cocoon, produced by the progenitor in previous mass loss episodes months to decades prior to the SN explosion through strong stellar winds, giant eruptions or even episodic outbursts. Initially, the outer circumstellar material (CSM) is not perturbed by the SN ejecta, and the early spectroscopic evolution is determined by the photoionization of the CSM after the shock breakout. Hence we initially see signs of the slow moving, photoionized wind, through the appearance of very narrow emission lines of H (Chevalier & Fransson, 1994). Later on, the high-velocity ejecta (a few 10^4 km/sec, Smith et al., 2016, for a review) eventually collide with the slow moving CSM. Ejecta-CSM Interacting SNe may also have different spectral appearance, such as in type Ibn, but in this case the CSM is H-poor and He-rich. The resulting spectrum will show narrow He lines in emission instead of the usual narrow H lines (Pastorello et al., 2008).

If the CSM is dense enough, the interaction can contribute to convert the kinetic energy from the shock wave into radiation, that can lead to an additional contribution to the luminosity (hence keeping luminous the light curve). Differences in luminosity, duration and profiles among type IIn SN spectra are due to diversity in the configuration and structure of the CSM around the star (Chugai, 1997).

1.2.1 A connection between LBVs and SNe IIn

SN 2005gl gives a clue of the connection between LBV stars and SNe IIn (Gal-Yam et al., 2007; Gal-Yam & Leonard, 2009). Before the SN explosion a deep *HST* image revealed a luminous progenitor at the SN position. The absolute magnitude determined for this object was $M_V = -10.3$ mag. If this source was a single star in quiescence, only an extreme LBV could be so luminous. Alternatively, this source could also be an episodic outburst during a longer duration eruption of an object fainter than $M_V = -10$ mag (Pastorello et al., 2018a). Also for SN 2010jl, a blue progenitor was detected by archival *HST* images. Its luminosity, 10 years before the SN, was $M_U = -12$ mag (Smith et al., 2011a). Alternative explanations proposed for the source were: a young stellar cluster, an very massive LBV in quiescence or a major stellar outburst.

1.2.2 Type IId Supernovae

A transitional group of interacting SNe shows similarity with both SNe IIn and SNe IIL, and they are sometimes named Type IId. They have line profiles which reveal the existence of a CSM around the exploding star already at early epochs. At early phases, the light curve declines rapidly, while a few months later the interaction between ejecta and CSM becomes predominant. This happens when the SN ejecta encounter substantially higher-density CSM regions. Several objects of this class show plateaus in their light curves sometimes during their evolution. The mean absolute magnitude of SNe IId at peak is $M_V = -17.9 \pm 0.3$ mag (review of Benetti, 2000).

The label SN IId stays for 'double' P Cygni profile, as there is contemporary presence of broad and narrow P Cygni profiles. While the former are SN ejecta signatures, the latter are due to the unshocked CSM. This category includes SN 1994aj (Benetti et al., 1998), SN 1996L (Benetti et al., 1999) and SN 1996al (Benetti et al., 2016). Also SN 1984E could be a member of this class, due to the double-peaked shape of Hα visible in the first spectrum of the object (Benetti et al., 1998). Unfortunately, as very few spectra of the object are available in the literature, the membership of SN 1984E to the type IId SNe cannot be firmly confirmed. Along with the double P Cygni profile, another remarkable feature is the lack of [O I] $\lambda\lambda$ 6300,6364 lines in the late-time spectra. A possible suggestion is that these supernovae had moderate-mass main-sequence progenitors, of $\sim$8 $M_\odot$ (Chugai & Danziger, 1994), or higher-mass progenitors exploding as fall-back SNe (Benetti et al., 2016).

1.3 Supernova 'Impostors'

Some transients mimic the spectro-photometric evolution of weak type IIn SNe, but as a major difference, these transients are non-terminal explosions. For this reason they are labelled "SN impostors" (Van Dyk et al., 2000). They are relatively faint, compared with normal SNe, having absolute magnitudes between -10 and -14 (Van Dyk et al., 2005). Similarly to SNe IIn, the spectra of SN impostors show narrow H emission lines over a blue spectral continuum.

These impostors can be eruptions from LBV stars, analog to the ones of η Carinae, although observed in an outer galaxy (see Sect. 2.2). Generally, SN impostors have luminous, hot, blue progenitors and there are indications that the progenitor stars survived the eruptive events, such as SN 1997bs (Van Dyk et al., 2000) and SN 2000ch (Wagner et al., 2004; Pastorello et al., 2010). LBVs or very massive hypergiants are suitable progenitors of a fraction of type IIn SNe. In some notorious cases, the real SN was preceded years or decades before by stellar outbursts. Initially these transients gained

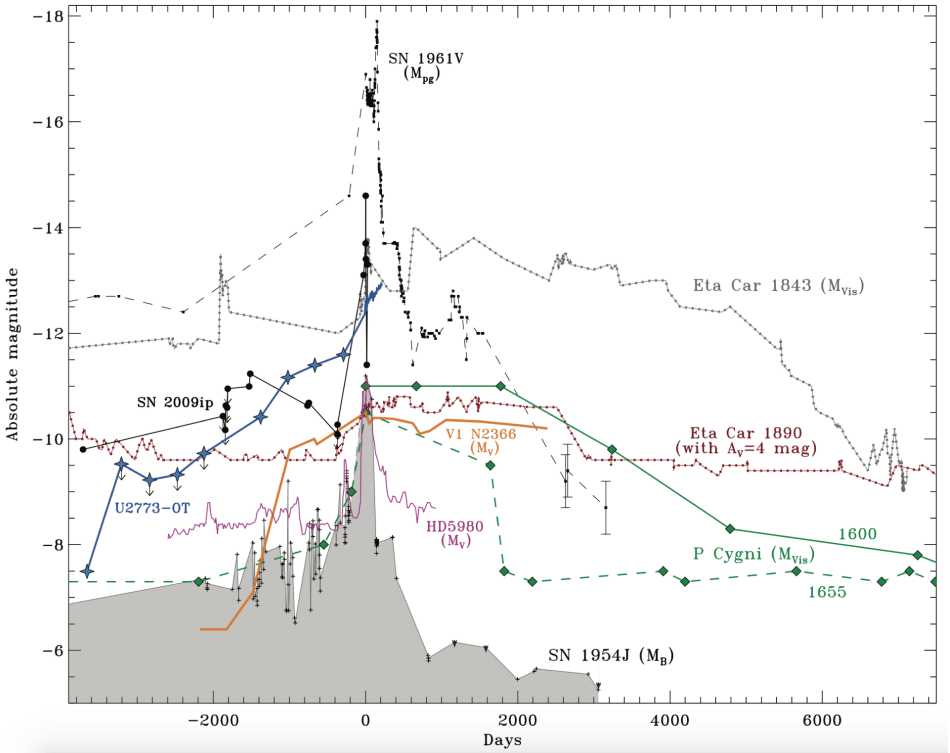

Figure 1.3: Light curves during outbursts of some important SN impostors. Among the others SN 1954J, SN 1961V, SN 2009ip, UGC2773-OT and η Car are present. Graph from Smith et al. (2011b).

the label of faint SNe and then reclassified as SN impostors. According to Ofek et al. (2014), the detection of an outburst years before the explosion should not be uncommon: a 50 % probability to observe an event brighter than $3{\times}10^7$ $L_\odot$ is calculated.

In this section we briefly mention the most important known SN impostors. The light curves of some of them are illustrated in Fig. 1.3.

- SN 1954J was a giant eruption of the bright blue irregular variable V12 in NGC 2403. This LBV outburst was well observed photometrically by Tammann & Sandage (1968) for a decade before the peak in 1954, although no spectra of the outburst were available. Apparently the star survived the event as a faint reddened star (Van Dyk et al., 2005). In the same galaxy, also the type IIn SN 2002kg was observed (Van Dyk et al., 2005), but other authors suggested that this event was in fact a brightening of the LBV V37 in NGC 2403 (Weis & Bomans, 2005)

- SN 1961V was discovered in the galaxy NGC 1058. Along the 'SN

impostors', this object is one of the most controversial, due to its very high luminosity (M at peak was almost -18 mag), blurring any clear distinction between LBV-like eruptions and real core-collapse (CC) Type IIn SNe. The proximity of the host galaxy allows the progenitor to be visible in plates years before the event, with an absolute $M = -12$ mag. Spectra were characterized by narrow (FWHM $\sim$ 2000 km s^{-1}) H, He and Fe II lines in emission and typical colours of F Supergiant, all characteristics of LBV spectra during quiescence (see below). Nowadays it is thought that SN 1961V was a real IIn SN preceded by a giant LBV eruption (Smith et al., 2011b), but for decades the question was debated.

- The spectra of SN 2007sv (Tartaglia et al., 2015) showed a blue continuum and prominent Balmer lines in emission at early phases, for this reason the object was initially classified as a type IIn SN. However, following observations performed at the Asiago Astrophysical Observatory revealed a lack of very high velocity material, expected in supernova ejecta. Also, the absolute magnitude at its discovery ($M_R = -14.25 \pm 0.38$) indicates that the object was likely a SN impostor. The research found a similarity with the prototype SN 1997bs (Van Dyk et al., 2000), and that SN 2007sv was probably a major eruption from a LBV.

- A number of outburst were observed in the irregular galaxy NGC 3432 over the past three decades, likely produced by the same LBV. The most remarkable was NGC 3432 OT2000, aka SN 2000ch (Wagner et al., 2004) that lasted over 2 months. A subsequent series of three eruptive episodes (NGC 3432 OT2008-9) have been observed in 2008-2009 from the same star (Pastorello et al., 2010), covering a temporal span of $\sim$1.5 years. In one of the rebrightenings, an absolute magnitude of -12.7 was reached. All peaks were followed by a temporary decrease in luminosity, minor luminosity oscillations were superimposed to the major brightness changes. Other outbursts were observed in 2017-2018.

  From the spectra, Wagner et al. (2004) derived that the effective temperature of the star during NGC 3432 OT2000 was $\sim$7800 K, and for NGC 3432 OT2008-9 (Pastorello et al., 2010) obtained $\sim$9000 K. The FWHM at maximum ranged from 1200 to 2500 km s^{-1}. P Cygni profiles indicated that absorbing material was probably ejected during the LBV eruptive phase. The approximate radiated energies E_{rad}(NGC 3432 OT2000) $\simeq 10^{47}$ erg, and E_{rad}(NGC 3432 OT2008-9) $\simeq 8.5 \times 10^{47}$ erg were estimated for the two events. As these brightenings are likely major LBV outbursts that belong to the same long-lasting eruptive phase, Kashi & Soker (2010) estimated the total energy to be $\sim$3

times larger than the radiated energies.

- UGC 2773-OT experienced a gradual brightening of 3 magnitudes over 5 years (Smith et al., 2016). The early spectrum of the transient was characterized by a warm continuum (T ∼7000 K), with numerous narrow absorption lines in the blue part, and a relatively weak and narrow Hα emission. The spectrum showed a clear P Cygni profile for Hα, suggesting outflow speeds of around 360 km s^{-1} (Smith et al., 2010). The early spectrum showed also strong absorptions of Ca II H & K, a weak [Ca II] doublet, and a relatively weak P Cygni profile of the Ca II IR triplet (Smith et al., 2010). These spectral features are somewhat similar to those of SN 2008S-like objects. The outflow speeds derived from the widths of the lines are relatively low (200–300 km s^{-1}). UGC 2773-OT is another ILOT showing a progenitor ($M_V \approx -8$ mag, Smith et al., 2010) in archive HST images obtained a decade before the discovery. The progenitor seems to be a luminous yellow star of at least 20 $M_\odot$ and $L = 1.3 \times 10^5 L_\odot$, although the extinction from circumstellar dust could make the star cooler and dimmer.

A collection of spectra of SN impostors and other ILOT types is shown in Fig. 1.4

1.3.1 SN 2009ip-like transients

SN 2009ip in NGC 7259 is the best example of multiple outbursts from an LBV followed after some years by the final SN event. In 2009 a transient was first observed, initially confused with a genuine faint SN (hence the SN designation), then it was classified as a SN impostor (Foley et al., 2011). From *HST* images taken before the eruption a progenitor was seen. This provided an evidence for a very massive star (M>50 $M_\odot$, Smith et al., 2010) as a progenitor, probably a LBV went in a outburst phase. The object underwent multiple explosions in rapid succession in 2009 and in 2011, resembling those of SN 2000ch (Wagner et al., 2004, see next chapter). In some of these eruptions M_R occasionally exceeded −14 mag. This erratic variabliity is typical of giant eruptions of a LBV (Pastorello et al., 2013; Mauerhan et al., 2013a).

In summer 2012, after a rebrightening, the source reappeared in a stronger outburst, labelled "2012a event", with a luminosity of $M = -15$, comparable to that of faint IIP SNe (Mauerhan & Smith, 2012). This outburst was followed by a third ("2012b event") on September 23, the brightest one, in which SN 2009ip reached $M = -18$ (Pastorello et al., 2013). The sequence of events 2012a and 2012b marked the real terminal SN explosion, with ejecta-CSM interaction powering the peak of event 2012b (Mauerhan et al., 2013a). Other scenarios have been proposed. For example Pastorello et al. (2013) suggested that the 2012b event could have been a Pulsational

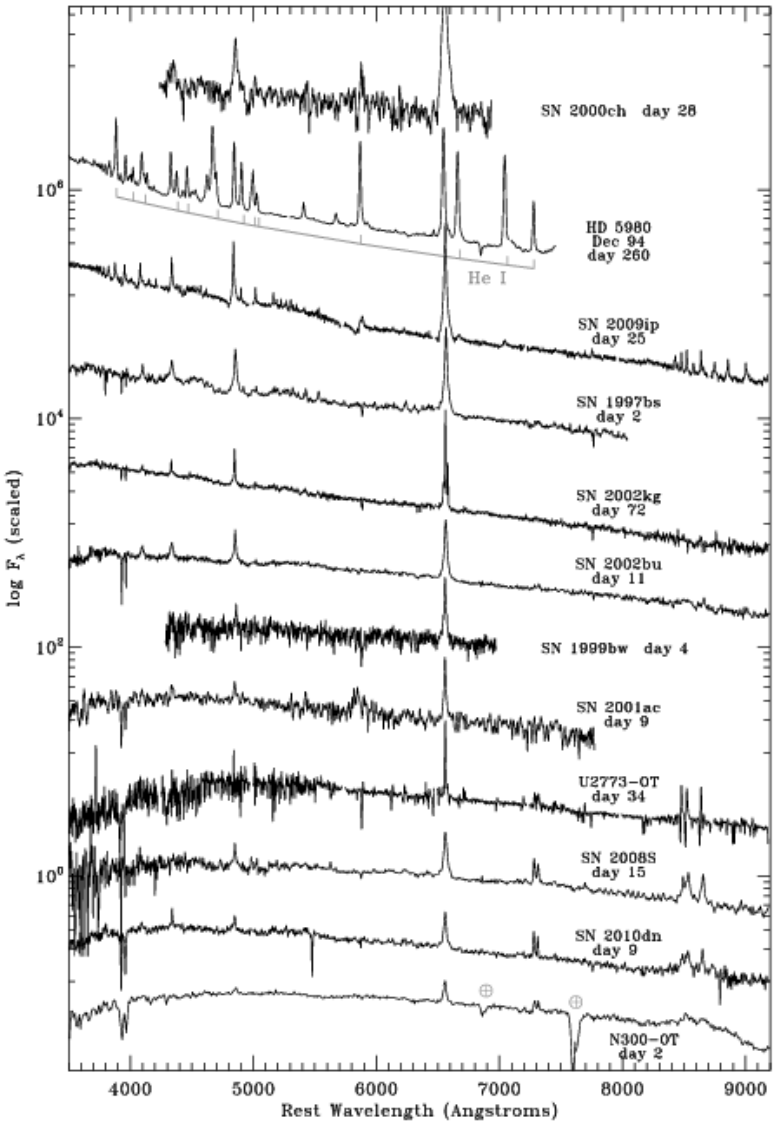

Figure 1.4: A comparison of some SN impostors and other interesting ILOTs, such as SN 2008S, UGC 2773-OT, SN 2009ip and NGC 300-OT. The epochs reported on the right are relative to the maximum light. Graph from figure 12 of Smith et al. (2011b).

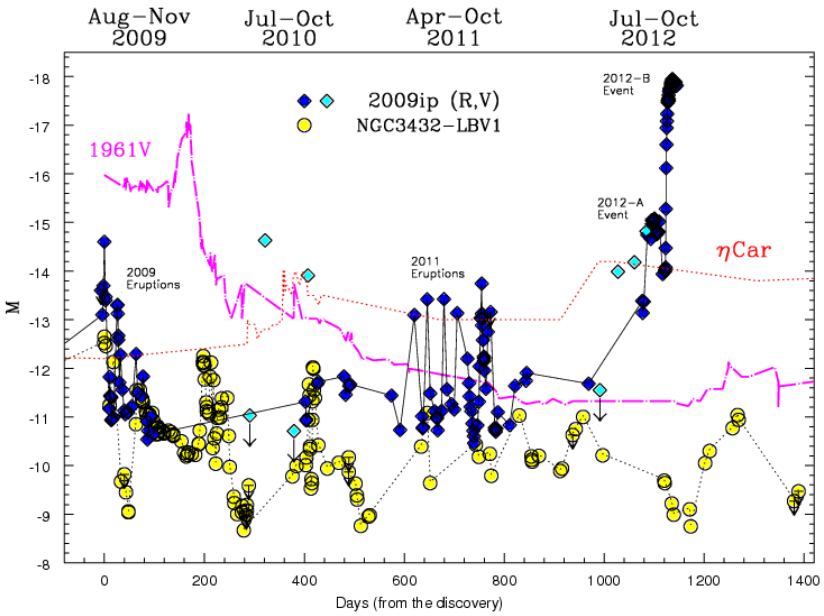

Figure 1.5: The light curve of SN 2009ip is compared with those of other objects, such as SN 1961V, η Carinae and NGC3432-OT. The large late-time brightening is believed to be a real Type IIn SN explosion. Graph from Pastorello et al. (2013).

Pair-Instability (PPI) SN, and that the progenitor has survived the last outburst. Differently from a pair instability SN, the destabilization from the electron-positron pair production is not sufficient to completely unbind the star. Instead, it triggers violent pulsation episodes, in which many solar masses are ejected from the inner envelope, without destroying the star, that is expected to explode later as a CCSN. In the case of a PPI SN event, no ^{56}Ni mass is ejected (Woosley et al., 2007). The SN scenario is supported by the fact that in 2011 an outflow velocity of $\sim$13000 km s^{-1} was measured, along with an extreme variability (in terms of peak luminosity, magnitude variation and time scale) was observed during the three years period before the final explosion. (Fraser et al., 2013a; Margutti et al., 2014; Graham et al., 2014). The light curve of SN 2009ip from the first outburst of 2009 up to the 2012b event is plotted in Fig. 1.5, where it is compared with other reference objects.

SN 2009ip is the prototype of a class of objects, that includes: LSQ13zm (Tartaglia et al., 2016), SN 2015bh (Thöne et al., 2017), SNhunt151 (Elias-Rosa et al., 2018), SN 2016bdu (Pastorello et al., 2018a). As an example for

all of them, here we describe LSQ13zm.

In 2013 LSQ13zm experienced a first eruptive episode, reaching $M_R = -14.9$ mag, comparable with those of SN impostors, followed by a much brighter outburst, a sequence of events similar to what was observed for SN 2009ip in 2012. The second rebrightening peaked at $M_R = -18.5$ mag, in the luminosities range of interacting supernovae (Tartaglia et al., 2016). The spectra of the second event show a blue continuum with prominent narrow Balmer lines in emission, and signs of interaction, i.e. an intermediate-width component in Hα. These characteristics reveal the presence of a dense, photoionised unshocked CSM, probably produced in previous mass-loss events, or in the first outburst.

Chapter 2

Non-terminal interacting stellar transients

2.1 Intermediate Luminosity Optical Transients

Intermediate Luminosity Optical Transients (ILOTs) (see e.g. Berger et al., 2009) have optical luminosities between those of novae (that can reach an absolute magnitude of about −10 mag, Aydi et al., 2018) and type II SNe, with an absolute magnitude brighter than −15 mag. This observational category includes multiple astronomical objects, such as different types of faint SNe (for example, Pastorello et al., 2004; Valenti et al., 2009; Spiro et al., 2014), major eruptions of hypergiant stars, including Luminous Blue Variables (LBVs, Smith et al., 2011b), Luminous Red Novae (LRNe, Pastorello et al. 2018, submitted to MNRAS), and Intermediate-Luminous Red Transients (ILRT, Botticella et al., 2009; Kasliwal et al., 2011; Prieto et al., 2008; Cai et al., 2018).

In the next paragraphs we will summarize the observed properties of the above four categories of ILOTs.

2.2 Outbursts of Luminous Blue Variables

LBVs are evolved, hot early spectral type supergiants, with extremely high luminosities ($M_{bol} < -10$ mag, or more than $5 \times 10^5 L_\odot$, and up to some $10^6 L_\odot$) and high masses (M> $30 M_\odot$). They are located in the upper part of the Hertzsprung-Russell (HR) diagram, as shown in Fig. 2.1. These stars present irregular variability in their light curves, and spectra with prominent H lines (see Humphreys & Davidson, 1994, for a review). Because of their high luminosity, they may occasionally exceed the Eddington luminosity

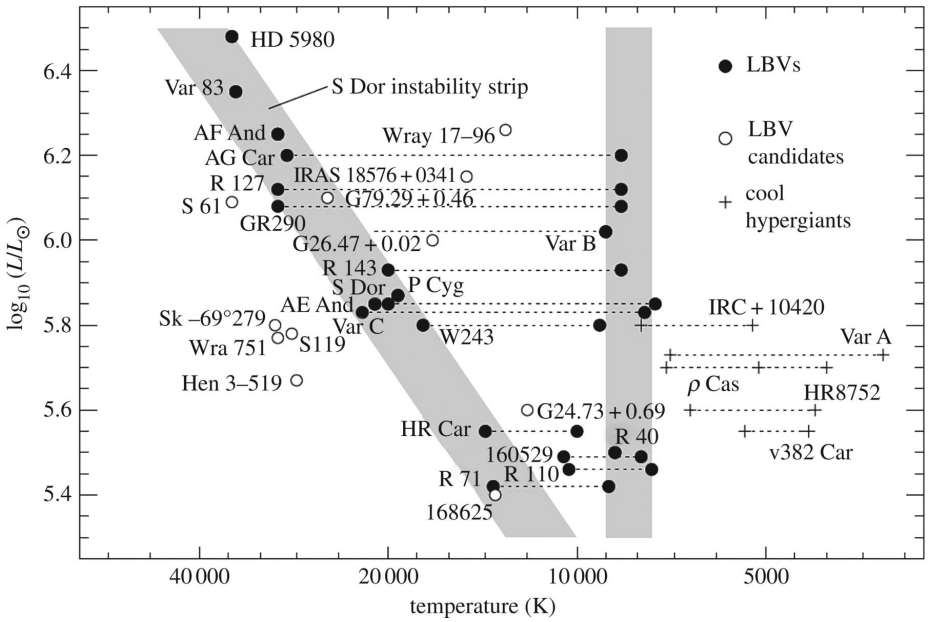

Figure 2.1: Position in the HR diagram of known (filled circles) and candidate (empty circles) LBVs in the Local Universe. Graph from Smith (2017), an adaptation of figure 9 of Humphreys & Davidson (1994).

limit, defined as:

$$L_{Edd} = \frac{4\pi cGM}{k} \tag{2.1}$$

with M being the mass of the star and k being the opacity per unit mass. L_{Edd} is the maximum luminosity for a star in hydrodynamical equilibrium. When the star exceeds this limit, it can erupt, driven by super-Eddington winds.

During quiescence, the stellar mass-loss rate is about 10^{-7} to $10^{-6} M_{\odot}$ yr^{-1}, but during eruptions it can reach 10^{-5} to $10^{-4} M_{\odot}$ yr^{-1} (Humphreys & Davidson, 1994). In giants eruptions, this value can be much higher, exceeding $10^{-3} M_{\odot}$ yr^{-1} (Smith & Hartigan, 2006). When this happens, a large fraction of stellar mass is violently expelled (up to 10 $M_{\odot}$).

S Dor variables are LBVs that experience normal eruptions, during which they eject a small portion of external layers. The visual luminosity of the star rises by 1-2.5 magnitudes in some years to decades, with an increase of mass loss (Wolf, 1989). The photosphere expands and cools, leading to a higher bolometric correction, with bolometric luminosity remaining nearly constant. Namely, a normal eruption leads simply to a shift in the Spectral Energy Distribution (SED) from the UV to visual wavelengths (Smith, 2014), and the star moves almost horizontally along the HR-diagram. The

increase of the mass-loss rates during S Dor variability is not enough to create a pseudo-photosphere, but it favours the extension of the photospheric radius, probably driven by radial pulsation (Van Genderen et al., 1997).

In contrast, in a major eruption the LBV brightness increases rapidly (in less than a month) by over 3 magn, (even up to 6 mag), and the absolute magnitude of the star can reach -14 mag (Humphreys & Davidson, 1994). These events are accompanied to the ejection of a significant fraction of the stellar envelope. The eruptions may last years or even decades, followed by a long period of quiescence.

During the quiescent phase, LBVs are spectroscopically similar to OB stars, with surface temperatures from 12 to 30 kK. Their spectra show features like strong H, He I, Fe II and [Fe II] lines, with P Cygni profiles indicating an expansion velocity of the gas of few hundreds km s^{-1}, while He II lines are weak (Humphreys & Davidson, 1994). When an LBV is in outburst, it can be confused with a SN IIn event, for this reason they are frequently labelled as SN impostors (see Chapt. 1). During the outburst phase, the spectra resemble those of cooler stars, like A of F supergiants, because the pseudo-photosphere expands (with a low velocity of 100-200 km s^{-1}) and cools to a temperature of about 7000-8000 K. After the expelled layers have expanded, prominent Balmer lines in emission appear, that resemble those observed in type IIn SNe.

A famous Galactic LBV is η Car. In the middle of 19th century the star experienced a major eruptive episode, known as the Great Eruption (GE), during which the star luminosity reached ~ -13 mag value (Davidson & Humphreys, 2012). In 1843, the apparent magnitude of the system rised from about 3 up to -0.4, becoming the second brightest star in the sky. In that decade, the star experienced an enormous mass loss, that lately formed the so called Homunculus Nebula, that now obscures the star, as shown in Fig. 2.2. Now the star has faded to mag $\sim$6, but it is still variable.

Also the P Cyg star, in which the notorious P Cygni spectral line profile was first identified, had undergone a major eruption during 17th centrury (Kashi, 2010). Another famous LBV is the variable S Dor in the LMC galaxy, that is the prototype of a variability of LBVs, called S Doradus phase. The S Doradus phase is defined as a photometric variable phase and radius variations with more or less constant luminosity (Van Genderen et al., 1997). A normal S Doradus phase, with a period of some years (6.8 for the prototype, Van Genderen et al., 1997) is superimposed on a very long-term variability, lasting decades (De Groot et al., 1996). The variability of S Dor was already known at the beginning of 20th century, along with other characteristic LBV observables, such as the Balmer lines with P Cygni profiles. In the '50s, it was noticed its similarity with the Hubble-Sandage variables (Hubble & Sandage, 1953) found in M31 and M33, today classified as classical LBVs. From the '80s, the study and the interest to this type of star has grown, and the same variability was found in other stars in the

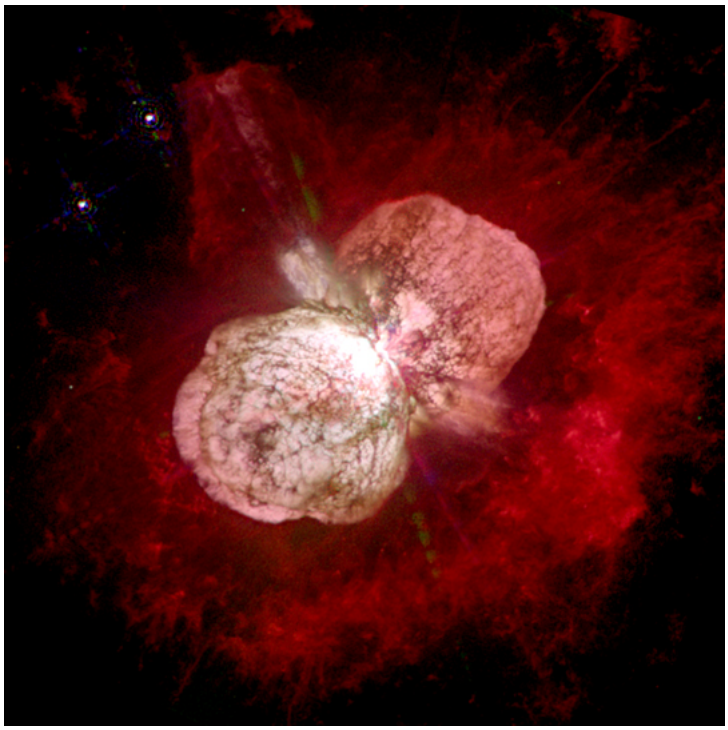

Figure 2.2: The Homunculus Nebula, produced by the star η Carinae during the Great Eruption of 1843. The star is located behind the bright spot, in the centre. Image taken by the Hubble Space Telescope.

Nearby Universe, like R 127 in the LMC, or AG Car in the Milky Way.

2.3 Luminous Red Novae

The most famous Red Novae (RN) are V838 Monocerotis (Munari et al., 2002; Soker & Tylenda, 2003), and V1309 Scorpii (Tylenda et al., 2011). The total energetics involved in these events is of the order of 10^{48} erg (Kashi & Soker, 2010), while the absolute magnitude at the maximum of V838 Monocerotis is ~ -10 mag. A red continuum, narrow Balmer emission lines and iron-peak elements absorptions are the main spectral characteristic of RNe. Their light curves have a double-peaked shape: first a blue peak, then a red one, reached a few months later.

V1309 Sco gave evidences that a merging event had occurred. Its pre-outburst photometric evolution showed a slow trend of increasing luminosity, characterized by numerous small ($\sim$0.5 mag) and modulated oscillations. Prior to the outburst, Tylenda et al. (2011) observed a shortening of the photometric variability period, that was initially of 1.4 days, implying that

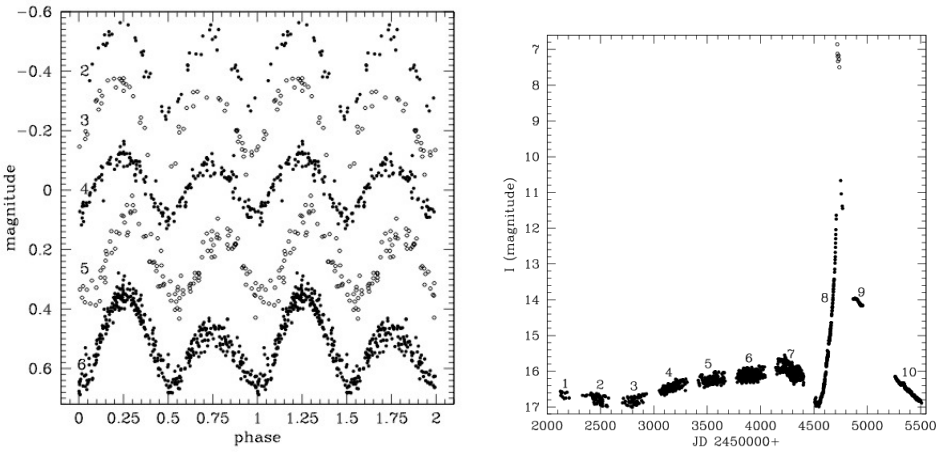

Figure 2.3: Left: the modulation of the light curve of V1309 Scorpii from 2002 to 2006, a few years before the outburst. The short-period modulated light curve is typical of a contact binary system. Right: the light curve of the stellar-merger V1309 Scorpii. Graphs from Tylenda et al. (2011).

the system was a contact binary system whose stars were approaching to each other. The two components were main sequence stars, with a total estimated mass of 1-3 $M_{\odot}$. The motion of the components in the common envelope created friction, reducing the angular momentum and causing the orbit radius to shrink. During the main outburst, the object brightened by $\sim$10 mag, i.e. by a factor of 10^4, but the orbital-timescale magnitude variability disappeared (Pejcha et al., 2017) as a consequence of the common envelope ejection that veiled the stellar system. The light curve of V1309 Sco in the years before and after the merging process is shown in Fig. 2.3.

Following Soker & Tylenda (2006), the envelope violently ejected by the primary star produced an initial, low-luminosity peak in the light curve. Then, the secondary star began to accrete onto the primary. Finally the stars cores merged and the shock kinetic energy of fast ejecta, colliding with a slower outflow, was converted into radiation that powered the second light curve peak. The final outcome of this process had the spectral appearance of an M-type star.

Near to the maximum, RNe have a continuum-dominated spectrum, similar to that of yellowish stars. It does not resemble that of novae, for the absence of high excitation lines and lower expansion velocities (few hundred km s^{-1}, Kashi & Soker, 2010). The strongest emission lines are those of the Balmer series, while absorption lines are identified as neutral or singly ionized metals, in particular Fe-peak elements. After the coalescence, the merger shows broad and strong molecular absorption bands of CO, H_2O, VO, TiO (Kashi & Soker, 2010), as visible in the spectra plotted in Fig. 2.4.

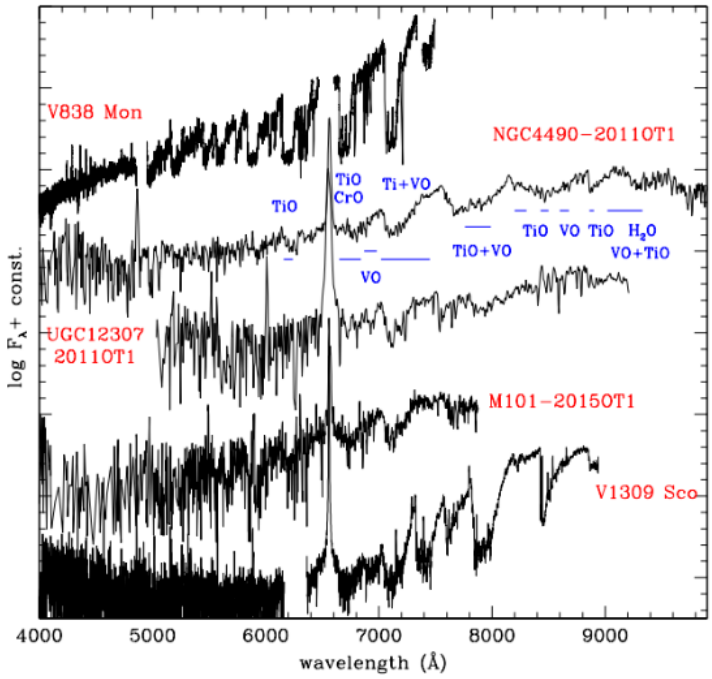

Figure 2.4: Molecular bands detected in the late spectra of some RNe and LRNe. The Hα and Hβ emission lines have been cut in the spectrum of V838 Mon to emphasize the region of the broad molecular absorption bands. Graph from Pastorello et al., 2018, submitted to MNRAS.

Nowadays, we are discovering extragalactic ILOTs with the same double-peaked light curve and similar photometric evolution as RNe, but more luminous. We label them Luminous Red Novae (LRNe, Pastorello et al. 2018, submitted). The conventional distinction between RNe and LRNe is made on the basis of the luminosity: if the absolute magnitude does not exceed that of V838 Mon, the object is considered a RN, while if the object is brighter than V838 Mon ($M_V \leq -11$), it is a LRN.

Differently from RNe, the progenitors of LRNe are probable yellow hypergiants of 20-30 $M_\odot$. In some cases, like NGC4490-2011OT1 or M101-2015OT1, a lower-luminosity outburst was observed before the major brightening. At maximum, the absolute magnitude of the objects peaked at around -13 mag. The early spectra of LRNe are similiar to the lower luminosity counterparts, also for the presence of P Cygni profiles. During the second peak, instead, Hα become dimmer, while a forest of absorptions from metal lines emerges.

NGC 4490-OT1 is the best observed member of this class. A progenitor

with an absolute magnitude of −6 mag was observed (Fraser et al., 2011). Because of its high luminosity, and the resemblance of the spectrum during the blue peak with that of type IIn SNe, the transient was firstly classified as a SN impostor. The pseudo-bolometric luminosity calculated for both peaks was $L_{BVRI} \sim 10^{41}$ erg s^{-1}. At late phases, molecular absorption features of VO and TiO were observed, in analogy with RNe, while Balmer lines became weaker (see, also, Fig. 2.4). At even later phases the colour of the objects becomes much redder. In particular, an IR excess was observed by Smith et al. (2016) in *Spitzer* images, and this was a plausible indication of dust formation.

RNe and LRNe probably originate from the same physical process, the ejection of the common envelope and eventually the coalescence of two stars (Kochanek et al., 2014).

2.4 Intermediate-Luminous Red Transients

Intermediate-Luminous Red Transients (ILRTs) are likely linked to evolved stars, such as Super-Asymptotic Giant Branch (S-AGB) stars (Prieto et al., 2008). NGC 300 OT2008-1 (Berger et al., 2009) and SN 2008S (Botticella et al., 2009) are prototypical objects for this class. NGC 300 OT2008-1 reached a bolometric absolute magnitude of −12 mag, while SN 2008S at maximum had a luminosity of 10^{41} erg s^{-1}, equivalent to −14 mag (Prieto et al., 2008). These are comparable with the luminosity of the faintest type II-P SNe (Pastorello et al., 2004; Spiro et al., 2014). The transients themselves are likely weak electron-capture SNe (Botticella et al., 2009; Thompson et al., 2009) or non-terminal eruptions of ∼8-15 $M_{\odot}$ stars (Bond et al., 2009) embedded in a dusty CSM.

The light curves of AT 2017be (Cai et al., 2018), SN 2008S and NGC 300 OT2008 transients are very similar, and resembles those of faint type IIP or IIL SNe. There is evidence that these objects are real SN explosions: Firstly, SN 2008S had similar total radiated energy as faint SNe, and it shows moderate expansion velocities of the ejecta of about 3000 km s^{-1} (Botticella et al., 2009). This one is difficult to explain with an LBV-like or a non-destructive stellar outburst. Secondly, Botticella et al. (2009) detected a late dimming phase with a decay slope matching that of radioactive ^{56}Co decay. Finally, late-time *Spitzer* IR observations showed that the progenitors of SN 2008S and NGC 300-OT have likely disappeared (Adams et al., 2016).

The spectral continuum of ILRTs becomes redder with time, and shows strong Balmer emission lines, the Ca II near-infrared triplet and the characteristic [Ca II] $\lambda\lambda$ 7291,7324 doublet. The width of the [Ca II] lines indicates velocities of 600-800 km s^{-1}, significantly lower than those of both classical novae and SNe. [Ca II] lines are a distinctive feature, which always characterizes ILRTs from very early phases (Fig. 2.5). Instead, their optical

spectra do not show molecular bands at any phase.

All ILRT candidates are observed in spiral galaxies of late morphological types, with the remarkably exception of M85 OT2006 (Kulkarni et al., 2007a), which occurred in a lenticular galaxy, though with a residual star formation. This object had a peak luminosity of $\sim 2\times10^{40}$ erg s^{-1} and total radiated energy of E_{rad}(M85 OT2006) $\simeq 6\times10^{46}$ erg over ~3 months. The progenitor's mass was estimated to be $< 8\ M_{\odot}$ (Pastorello et al., 2007b), but the interpretation of the outburst is controversial. It was suggested by Kulkarni et al. (2007a) that the origin of M85 OT2006 is a stellar merger. They also estimated that the effective temperature and the stellar radius at the time of peak luminosity were $T_{eff} \simeq 4600$ K and R $\simeq 3600\ R_{\odot}$ respectively. Pastorello et al. (2007b) proposed a faint SN interpretation, suggesting that M85 OT2006 was a ILRT (Adams et al., 2016; Cai et al., 2018). This can have implications on physical properties of the progenitors, statistically favouring high mass stars, hence consistent with S-AGB stars.

In the context of ILOT events, we will analyse the case of SN 2013gc. It was classified as a Type IIn SN, although its luminosity was quite low for a classical SN. We will see that this is explained with its late discovery, about 2 months after the brightness peak. More importantly, a few faint outbursts were discovered a posteriori in images taken a few years before the real SN explosion, suggesting that SN 2013gc is one of the rare cases of real SN IIn with a pre-SN impostor detection.

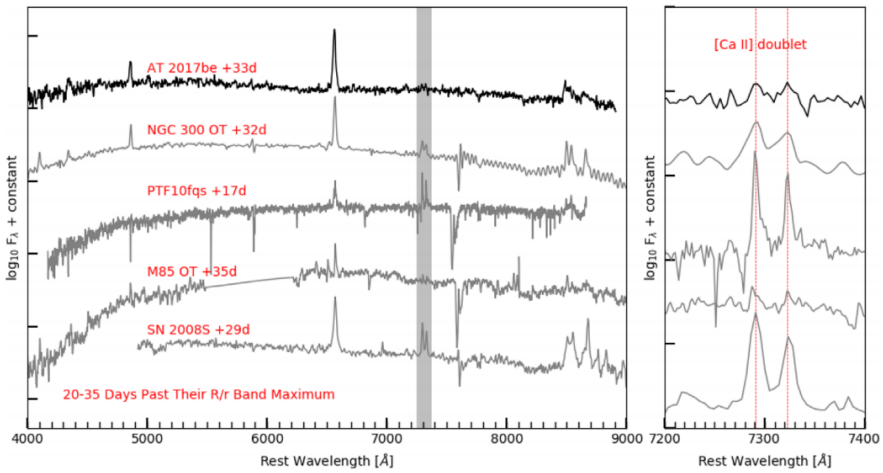

Figure 2.5: Comparison of ILRTs spectra obtained around one month after their maximum. The [Ca II] doublet lines are marked with the grey shaded area in the left panel. The right panel shows a blow-up of the profiles. Graph from figure 10 of Cai et al. (2018), references therein.

Chapter 3

Type IId supernovae: the sample

The main goal of this dissertation is the study of SN 2013gc, that will be introduced later in this chapter. Here, we will introduce our sample of type IIn/IId comparison objects, including: SN 1994aj, SN 1996al, SN 1996L and SN 2000P. SN 1984E is likely another member of this family, but a suitbale dataset is not available for this object (Benetti, 2000).

- The absolute magnitude of SN 1994aj (Benetti et al., 1998) at maximum is $M_V = -17.8 \pm 0.3$, intermediate between those of 'regular' ($M \sim -16.8$, on average) and 'bright' ($M \sim -18.9$) SNe IIL (Valenti et al., 2016). The initial luminosity decline of SN 1994aj is 4.4 mag $(100\ \mathrm{d})^{-1}$, consistent with that of SNe IIL. Then, at 100–120 d, the luminosity decline becomes much slower, marking the onset of the interaction between SN ejecta and CSM. The decline rate in this phase is around 0.5 mag $(100\ \mathrm{d})^{-1}$, flatter than the ^{56}Co decay rate.

  SN 1994aj has spectra with double P Cygni line profiles at early phases, similar to those of SN 1984E. For the latter, a super-wind with a velocity of 3000 km s^{-1} is proposed to explain the narrow P Cygni feature (Dopita et al., 1984). The Hα profile shows a broad emission component, on top of which a narrow P Cygni component (FWHM=25 Å) sits. No broad P Cygni absorption is visible. Na I D, Ca II NIR triplet and Fe II lines (multiplet 42) lines are present in the early spectra. Later on (phase 100–200 d), the emission lines grow in strength, with Hα line being the most prominent feature. Hβ also shows a narrow P Cygni absorption. After one year, Hα is still visible, while the classical [O I] $\lambda\lambda$ 6300,6364 feature, usually detected in CC SNe, is not present.

  The multi-component Hα profile and the high luminosity of SN 1994aj suggest the presence of a dense circumstellar medium. The SN observables are explained through the conversion of kinetic energy into

radiation, due to the interaction between the SN ejected material and the CSM.

- The light curve of SN 1996L (Benetti et al., 1999) shows a linear post-peak decline, with a slope of 6 and 5.2 mag (100 d)$^{-1}$ in the B and V bands, respectively, consistent with the values inferred for SNe IIL. At around 3 months, when the main powering source is the ^{56}Co to ^{56}Fe decay, the light curve is expected to decline with a rate of 0.98 mag (100 d)$^{-1}$. However, at 90 days after maximum, the decline rate slows down to 0.15 mag (100 d)$^{-1}$. This low value implies the existence of an additional source of energy that powers the light curve (likely ejecta-CSM interaction, see below). At +300 days, the decay rate increases again to 1.4 mag (100 d)$^{-1}$. The absolute magnitude at maximum is $M_V = -17.4 \pm 0.1$ mag, very similar to that of SN 1994aj.

  SN 1996L has been originally classified as a type II SN because of the presence of Balmer lines in emission on a very hot ($T_{bb} \sim 16000$ K) continuum. But the line profiles show 2 main components: one broad ($v_{FWHM} = 3500$ km s^{-1}) and one narrow ($v_{FWHM} = 500$ km s^{-1}). There is no evidence of a broad P Cygni absorption component in Balmer lines. After about two months, the continuum temperature declines, while Hα develops a symmetric P Cygni profile, with the broad component becoming even broader, reaching a FWHM of 6000 km s^{-1}. Fe II and Ti II lines are visible in the SN spectra, while the broad Na I D absorption is not detected. The expansion velocity of the narrow P Cygni component, as derived from the absorption minimum, is 1700 km s^{-1}. The spectra hence reveal the presence of a slowly expanding CSM shell. This shell probably originated by a strong progenitor wind during a previous mass-loss episode. At 270 days, the narrow P Cygni disappears, and the broad component decreases its velocity to 3700 km s^{-1}. After 1 year, Hα is still the dominant feature, while [Ca II] and [O I] lines are weak. He I emission lines are also clearly detected in this phase.

  Benetti et al. (1999) suggested that the narrow Balmer emission lines in the early spectra are produced by the recombination of the CSM ionized by the shock break-out ionizing radiation. The additional source of energy that sustains the luminosity of the SN between 90 and 270 days is the interaction between the SN ejecta and the CSM. When the CSM is swept away, the SN luminosity rapidly fades.

- SN 1996al (Benetti et al., 2016) is the best studied SN IId, with an observational campaign that lasted 2 years in photometry, and 15 years in spectroscopy. In 1988 (8 years before the explosion), significant Hα flux was detected at the position of the SN. This provided strong clues about the nature of the progenitor, which was a very massive star,

most likely an LBV.

The absolute magnitudes of SN 1996al at maximum are $M_B \sim -18.6 \pm 0.4$ and $M_V \sim -18.2 \pm 0.3$ mag. The B-band decline rate is 4.8 mag $(100\ \mathrm{d})^{-1}$, compatible with that of SNe IIL. Between +150 and +320 days, the decline rate fairly matches that of ^{56}Co decay. This decline is followed by a plateau, with a minor (0.1-0.2 mag) rise in brightness both in the V and R bands. Later on, from +450 days, the light curve of SN 1996al experiences a monotonic decline, with a slope similar to that observed at 150-300 days.

The spectra of SN 1996al cover 15 years of observations, from +23 to +5542 days, with an optimal coverage and cadence. The early spectra show a hot, blue continuum ($T_{bb} \sim 12000$ K) that becomes redder with time, reaching a temperature of about 7000 K at +60 days. In this phase, the spectra are dominated by broad Balmer lines. Their profile is complex, and its decomposition into Gaussian or Lorentzian components can constrain the geometry of the emitting material (CSM and ejecta). The wind velocity, as inferred from the minimum of the narrow P Cygni of the Fe II lines, is about 500-600 km s^{-1}. The narrow lines likely arise from a dense CSM, which was previously ionized by the X-UV flash in the shock break-out, and/or interaction with lower density inner CSM. The spectra do not change during the first few weeks. After one month, a few lines of He I and Ca II IR triplet became visible.

The Balmer lines have a multi-component profile that evolves with time. Between +23 and +43 days, Hα is fitted with a broad Lorenzian, plus a narrow P Cygni on top of it. The FWHM velocity drops from the maximum value of 7000 km s^{-1} down to 5600 km s^{-1}. Then, between +53 and +101 days, the broad component is reproduced with a Gaussian, whose FWHM decreases to 3200 km s^{-1}. A blue wing is now visible, which extends to $\sim$11000 km s^{-1}. In this phase, the Hα/Hβ ratio increases, indication of collisionally excited Hα emission. At +142 days, the narrow lines arising in the unshocked CSM disappear. The Hα is now fitted by 3 Lorenzian components (up to +523 days, while at later epochs the 3 components became Gaussian), labelled as Blue, Red and Core. The names refer to the fact that these components are blue-shifted, red-shifted and at rest-frame. Their FWHM are nearly identical. The 3 components remain visible for years.

The He lines, in particular λ7065, present a composite profile similar to that of Hα, suggesting that Hydrogen and Helium transitions occur in the same asymmetric, He-rich region. The energy necessary to produce the He line emissions comes from the powerful CSM/ejecta interaction, that is operating at all phases, due to the proximity of the

dense CSM layers to the SN progenitor.

Because of the faintness of the bolometric luminosity during the first 100 days, a low ejected mass (1.15 $M_{\odot}$, 0.15 $M_{\odot}$ of which is H and 1 $M_{\odot}$ is He) is inferred, which is in contrasts with the high mass of the progenitor (M_{ZAMS} = 25 $M_{\odot}$). From the bolometric light curve, a modest upper limit of 0.018 $M_{\odot}$ of ^{56}Ni is calculated, lower than normal CC SNe. This suggests that the internal layers likely fall back onto the collapsing stellar core, forming a black hole. The fall-back naturally explains the lack of [O I] $\lambda\lambda$ 6300,6364 lines in the late spectra, as the O and Fe-rich layers has fallen into the black hole. A low ^{56}Ni mass is expected in the fall-back scenario because this element, synthetized in the inner mantle of the star, is not ejected by the SN explosion.

The 3D geometry of the surrounding CSM is structured: it has an overall spherically symmetric shape in proximity of the exploding star. The ejecta interact with an equatorial disc, that is responsible of the Red and Blue bumps of Hα: the blue-shifted component arises from the approaching side of the disc, while the red-shifted component originates in the receding part. The disc has an extension of over 0.15 pc, as deduced rom the long-duration of the interaction (to 15 yr after the explosion). The disc is then embedded in a spherically symmetric, clumpy CSM. The clumpiness of this region is deduced by the enhance of the He lines strength: when the ejecta reach the clumps, the interaction heats the gas allowing the emission from the He-rich gas.

- The photometric and spectroscopic data of SN 2000P are published for the first time in Reguitti et al. (2018). They will be described in Section 3.1.

3.1 SN 2000P

3.1.1 Discovery and host galaxy

SN 2000P was discovered on 2000 March 8 by the amateur astronomer R. Chassagne at R.A.=$13^h07^m9^s.88$ and Dec=$-28°13'59".3$ (J2000). The SN was located about 16" east and 21" south of the center of the spiral galaxy NGC 4965 (Colas & Yamaoka, 2000). A confirmation image was taken at the Pic du Midi Observatory. The magnitude at discovery was 14.1. A finding chart of the object is shown in Fig. 3.1. The original classification as type IIn SN was obtained through an optical spectrum taken on 2000 March 10 with the ESO La Silla 1.54-m Danish telescope+DFOSC (Cappellaro et al., 2000). The redshift of the galaxy and the mean distance modulus, as reported

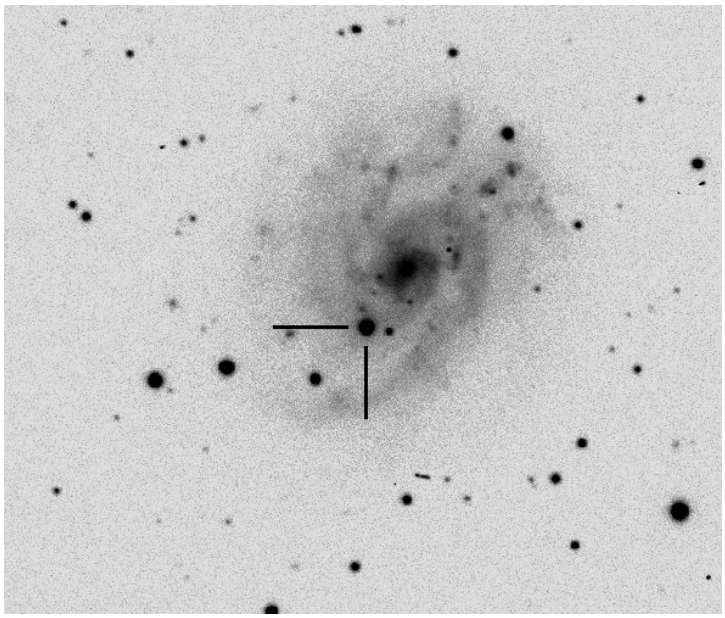

Figure 3.1: An R-band image of the host galaxy, NGC 4965, with SN 2000P. The image was obtained 2 days after the discovery, with the Danish telescope. The location of the SN is marked.

by the NASA/IPAC Extragalactic Database (NED)[1], are $z = 0.007542 \pm 0.000017$ and $m - M = 32.83 \pm 0.77$ mag, respectively. NGC 4965 is an emission-line galaxy, morphologically classified as SAB(s)d, according to De Vaucouleurs et al. (1991). Basic informations on type IId SNe properties and their host galaxies, obtained from NED, are summarized in Table 3.1.1.

[1] http://nedwww.ipac.caltech.edu/

Table 3.1: Main parameters of the type IId SNe sample, including SN 2000P.

SN name	SN 1994aj	SN 1996L	SN 1996al	SN 2000P
Host galaxy name	anonymous	PGC 36065	NGC 7689	NGC 4965
Morphological type	Sc	Sa	SAB(rs)cd	SAB(s)d
Distance Modulus (mag)	35.72±0.15	35.76±0.15	31.93±0.13	32.83±0.77
Distance to Galaxy Core (kpc)	4.9	20.4	3.5	4.7
A_V (mag)	0.115	0.255	0.032	0.209
Peak absolute mag	$M_R = -17.8$	$M_V = -17.5$	$M_B = -18.6$	$M_R = -18.8$

3.1.2 Light curve of SN 2000P

SN 2000P was initially followed photometrically by amateur astronomers, mostly in white light. These observations were scaled to R-band magnitudes. Later on, we started a multi-band photometric campaign in the optical bands, while the NIR campaign started at about +80 days. During the first week, the SN shows a decline in luminosity. This indicates that the rising phase and the light curve maximum are not observed. For this reason, the phases reported in this dissertation are referred to the first detection date, and not to the maximum.

At early phases, the SN is brighter in U than in other bands, then the U-band light curve declines rapidly for 80 days, with a mean decline rate of 5 mag $(100\ \mathrm{d})^{-1}$. In the same period, the R apparent magnitude of SN 2000P increases from 14 to 18 mag. Between +270 and +400 days a plateau is observed in the R and I bands at around 21 mag, while in B and V the light curves are still slowly declining. At +900 days ($\sim$2.5 years after maximum) the SN field has been imaged with NTT in the R and the narrow-band Hα filters, but only an upper limit of 21.7 mag is measured. At 1168 days (over 3 years) after discovery, SN 2000P has been targeted with the VLT+FORS1 telescope, and a residual source is identified at the SN location. The object was so faint that only an 8-meter-class telescope could achieve such observation. The magnitudes of that source range between 22.8 mag in I and 24.7 mag in B.

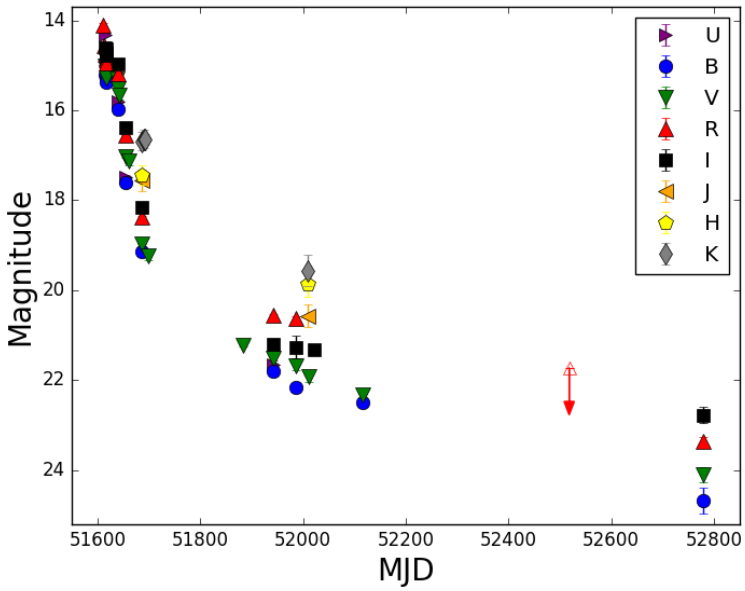

Figure 3.2: Optical and NIR light curves of SN 2000P, spanning about 3 years of observations. The magnitudes are not corrected for line-of-sight extinction. The red down-arrow indicates an upper limit in the R band.

The complete *UBVRIJHK* photometry of SN 2000P is presented in Tab. 3.2, and the optical+NIR light curves are plotted in Fig. 3.2.

3.1.3 Spectral evolution of SN 2000P

SN 2000P has an excellent spectroscopic dataset. The technical informations on the spectra are provided in Tab. 3.3. In the table, we added also information on the polarization spectrum of SN 2000P from Hoffman et al. (2005). In Fig. 3.3, we plot the spectral sequence and the logarithmic evolution of the Hα profile of SN 2000P.

Hα is characterized by a very narrow P Cygni absorption and an extended Lorentzian red wing. A similar narrow P Cygni feature is also visible in the Hβ and Hγ lines, with the latter being visible only during the first week. Many bumps, likely due to Fe II, are observed in the SN spectra. It is worth comparing the spectra and the Hα profile evolution of SN 2000P with those of SN 1996al (Fig. 5 and 7 of Benetti et al., 2016). In the spectra of SN 2000P obtained a very few days after the maximum light, the blue continuum indicates a high gas temperature. We fitted the continuum with a black-body, but the shape is compatible with the Rayleigh-Jeans approximation, and a physical temperature cannot be obtained. The large flux at the blue wavelengths is consistent with the high U-band luminosity. The decline of the light curve soon after the discovery indicates that the peak luminosity was not observed, although the high U-band luminosity and the shape of the spectral continuum suggest that the SN exploded only a few days before our first detection.

In the early spectra, Hα and Hβ show a double P Cygni profile, while a broad feature in emission at $\sim$5900 Å is likely a blend of He I λ5876 plus Na I D. At +30 days, many bumps due to metal lines arise and the Ca II triplet becomes quite prominent. From this epoch, a blue-shifted Hα component starts to develop with an intermediate-width (FWHM $\sim$1100 km s^{-1}), and grows in strength with time. After one year from maximum, Hα remains the only observable feature, and the blue-shifted component is more prominent than that at the rest frame.

Table 3.2: Optical and NIR photometry of SN 2000P. Amateur astronomers measurements are also included for completeness.

Date	MJD	phase[a]	U	B	V	R	I	J	H	K	Telescope[b]	Observer
2000-03-08	51611.03	0.0				14.10(04)					0.3 meter	Chassagne
2000-03-09	51612.12	1.1				14.57(05)					Pic	Colas
2000-03-10	51614.18	3.2	14.31(03)	15.20(02)	15.01(02)	14.76(02)	14.61(02)				Dan	Turatto
2000-03-12	51616.24	5.2	14.68(03)	15.30(02)	15.10(02)	14.86(02)	14.64(02)				Dan	Turatto
2000-03-13	51616.64	5.6			15.17(05)		14.79(05)				0.25 meter	Kiyota
2000-03-13	51617.24	6.2	14.91(03)	15.37(02)	15.29(02)	14.94(02)	14.73(02)				Dan	Turatto
2000-04-04	51638.01	27.0			15.30(10)						KAIT	Li et al. (2002)
2000-04-07	51641.08	30.1	15.82(05)	15.98(05)	15.52(02)	15.20(03)	14.98(07)				EF2	Pastorello
2000-04-09	51643.04	32.0			15.67(10)						KAIT	Li et al. (2002)
2000-04-19	51654.00	43.0	17.48(03)	17.60(03)	17.04(03)	16.56(02)	16.39(02)				TNG	Benetti
2000-04-26	51661.25	50.2			17.12(10)						KAIT	Li et al. (2002)
2000-05-23	51687.00	76.0		19.14(05)	18.96(02)	18.37(02)	18.17(05)				TNG	Benetti
2000-05-23	51687.09	76.1						17.55(24)	17.44(21)	16.69(20)	SOFI	Salamanca
2000-05-26	51690.95	79.9								16.64(20)	SOFI	Grosbol
2000-05-27	51691.95	79.9								16.65(12)	SOFI	Grosbol
2000-06-05	51699.50	88.5			19.23(10)						KAIT	Li et al. (2002)
2000-12-06	51884.60	273.6			21.22(02)[c]						HST	Li et al. (2002)
2001-02-02	51942.37	331.3	21.65(08)	21.80(09)	21.51(08)	20.56(03)	21.20(06)				EF2	Pastorello
2001-03-17	51985.35	374.3		22.17(10)	21.69(08)	20.62(04)					Dan	Pastorello
2001-03-18	51986.29	375.2					21.26(26)				Dan	Pastorello
2001-04-09	52008.30	397.3						20.57(25)	19.85(30)	19.56(34)	SOFI	Spyromilio
2001-04-12	52012.15	401.1			21.92(12)						Dan	Pastorello
2001-04-23	52022.10	411.1					21.33(03)[d]				HST	Li et al. (2002)
2001-07-26	52117.02	506.0		22.49(04)	22.33(05)						VLT1	Cappellaro
2002-08-31	52518.15	907.1				>21.72					EF2	Pastorello
2003-05-20	52779.02	1168.0		24.67(29)	24.10(16)	23.36(11)	22.78(18)				VLT2	Zampieri

[a] Days after the discovery

[b] Pic = Gentili 1.05m Pic du Midi, Dan = ESO Danish 1.54m+DFOSC, EF2 = ESO 3.6m+EFOSC2, TNG = TNG 3.6m+OIG, SOFI = ESO NTT+SOFI, VLT1 = VLT (UT1) 8.2m+FORS1, VLT2 = VLT (UT4) 8.2m+FORS2

[c] HST+F555W

[d] HST+F814W

Table 3.3: Spectroscopic observations of SN 2000P.

Date	MJD	phase[a] (d)	Range (Å)	Resolution[b] (Å)	Telescope	Instrument
2000-03-11	51614.2	3.2	3900-6840	4.7	ESO 1.54m	DFOSC (gr7)
2000-03-13	51616.3	5.3	3350-9800	9.3	ESO 1.54m	DFOSC (gr4+gr5)
2000-03-14	51617.2	6.2	3860-6820	5.1	ESO 1.54m	DFOSC (gr7)
2000-03-25	51629.0	17.0	4400-6800	?	Keck 10.4m	LRIS (Hoffman et al., 2005)
2000-04-07	51641.1	29.1	3370-9800	16	ESO 3.6m	EFOSC2 (gr11+gr12)
2001-02-02	51942.3	331.3	3360-7450	9	ESO 3.6m	EFOSC2 (gr11)
2001-07-27	52117.0	506.0	4230-8920	11	VLT UT1 8.2m	FORS1
2003-05-20	52779.0	1168.0	3400-9600	10	VLT UT4 8.2m	FORS2

[a] Days af the discovery
[a] FWHM of the night sky lines.

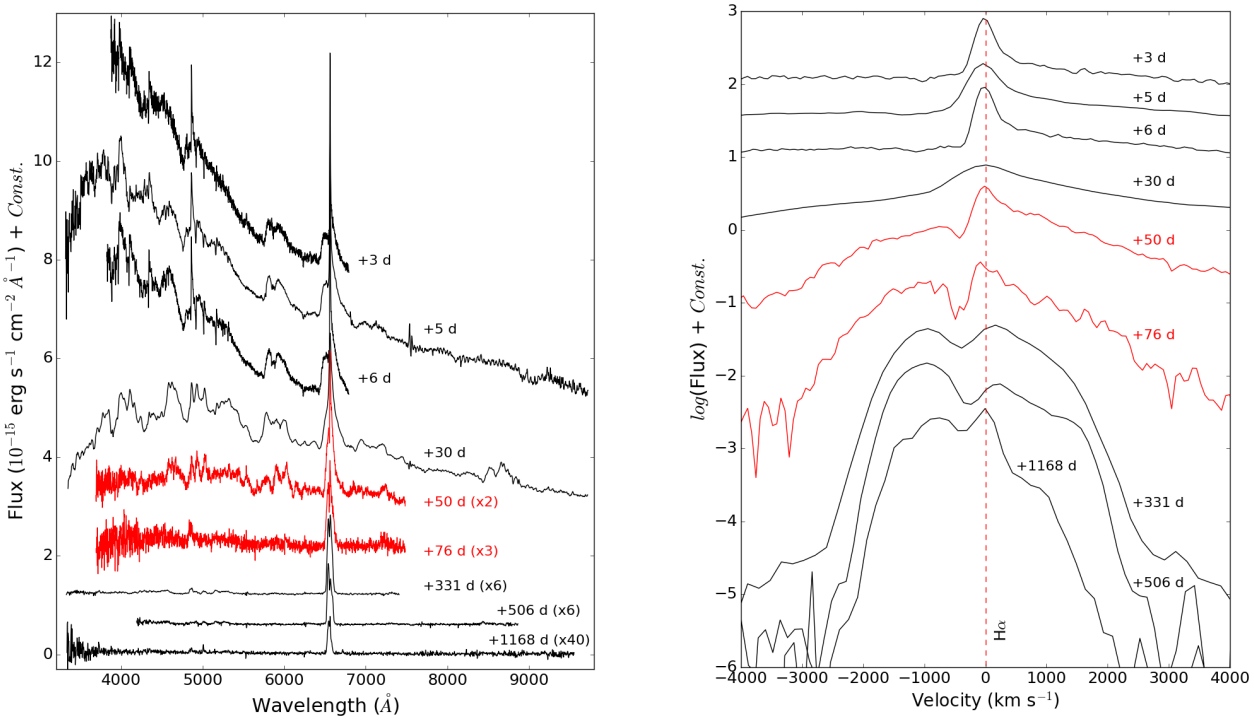

Figure 3.3: Left: Time sequence of optical spectra of SN 2000P, spanning about 3 years. The flux of the spectra are scaled to match the R-band or, if not available, the V-band photometry of the closest night. The spectra plotted in red colour are taken from the CfA Supernova Data Archive (https://www.cfa.harvard.edu/supernova/SNarchive.html), to fill the time gaps of our sequence. Right: Evolution of the Hα profile in the same spectral sequence. The logarithm of the specific flux is reported on the y-axis. The velocity with respect to the rest-frame is shown in the x-axis. In both graphs the phases are relative to the discovery.

3.2 SN 2013gc

The study of SN 2013gc is the main goal of this thesis. We studied this object both in photometry and spectroscopy, to understand the physical processes triggering and powering the explosion, and unveil the nature of the progenitor.

3.2.1 Discovery

SN 2013gc (=PSN J08071188-2803263) was discovered on 2013 November 7 at RA=$08^h07^m11^s.88$ and Dec=$-28°03'26".32$ (J2000), 43.3" east and 18.0" south of the nucleus of the galaxy ESO 430-20 (a.k.a. PGC 22788, Antezana et al., 2013). The SN had a magnitude of 16.7. The discovery chart is in Fig. 3.4. The discovery was done by the CHilean Automatic Supernova sEarch survey (CHASE; Pignata et al., 2009), using the Panchromatic Robotic Optical Monitoring and Polarimetry Telescopes (PROMPT; Reichart et al., 2005), at the Cerro Tololo Inter-American Observatory (CTIO).

The CHASE survey started in 2007 with the goal of discovering young SNe in the southern hemisphere. The survey utilizes four of the six PROMPT telescopes. They were designed to get prompt observations of the optical counterparts of Gamma Ray Bursts, and are an ideal tool to carry out a search of nearby SNe, in which the instrument has to move quickly from one galaxy to another. A limiting magnitude ∼18.0 can be reached with a 40 seconds exposure. This limits the distance galaxy sample in which to search for SNe can be performed to radial velocity <3000 km s^{-1}. Target selection, data acquisition, download and reduction are fully automated. This guarantees a real-time performed search, which is necessary to find very young SNe. The observational cadence is of 3-4 days for each galaxy in the sample. On average, the six telescopes observe ∼250 galaxies per night. Untilt 2012, the survey had discovered more than 130 SNe (Hamuy et al., 2012).

The original spectral classification indicated that SN 2013gc was a type IIn SN (Antezana et al., 2013). The spectrum, discussed in Chapter 6, was obtained soon after the discovery with the Las Campanas 2.5-m du Pont telescope (+WFCCD), and cross-correlated with a library of SN spectra using the "Supernova Identification" code (SNID; Blondin & Tonry, 2007). SN 2013gc was classified as a type IIn SN similar to SN 1996L (Benetti et al., 1999) at about two months after the explosion.

3.2.2 Host galaxy

The host galaxy ESO 430-20 is a member of a small group of galaxies (Crook et al., 2007). The morphological classification, from the RC3 Catalogue (De Vaucouleurs et al., 1991), is SAB(s)d. Details on the host galaxy obtained from NED are summarized in Tab. 3.4. The type II SN 2013ak was also

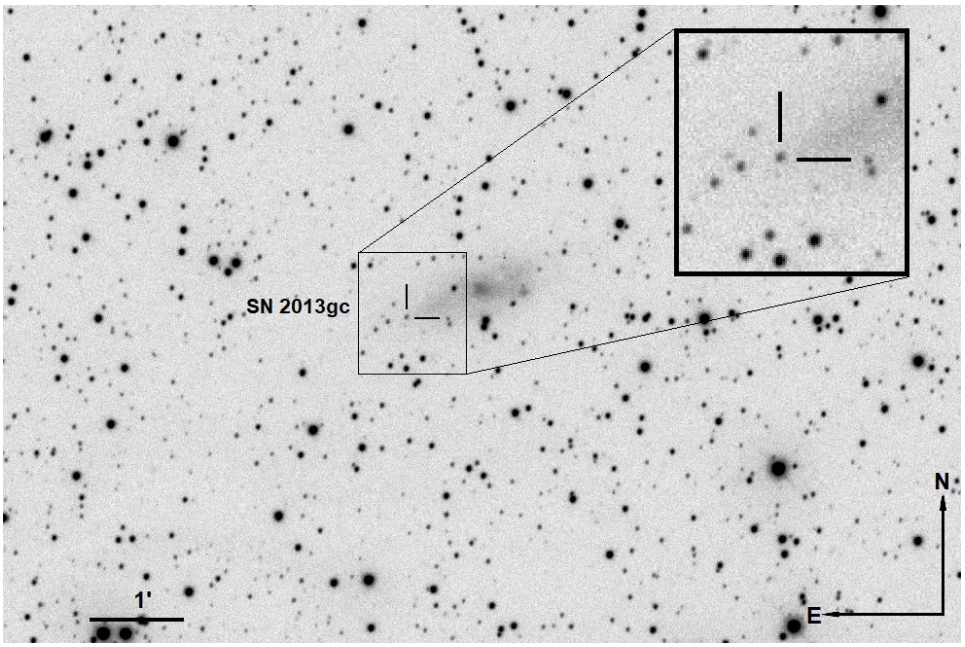

Figure 3.4: Discovery image of SN 2013gc taken on 2013 November 7 with the PROMPT-3 telescope and clear filter. A blow up of the SN location is shown in the top-right inset.

discovered in this galaxy, on 2013 March 9 (Carrasco et al., 2013), at magnitude 13.5. The location of SN 2013gc is far from the galaxy center: with a distance of 12.37 Mpc, the SN is 2.81 kpc from the nucleus, while the radius of the galaxy is 3.4 kpc. Due to the relatively large radial distance from the galaxy center, the local dust contamination is likely small.

3.2.3 Distance

The distance of ESO 430-20 is controversial. The Virgo + Great Attractor + Shapley velocity ($v = 942 \pm 20$ km s^{-1}, Tab. 3.2.2), assuming $H_0 = 73$ km s^{-1}Mpc^{-1}, provides a distance $d = 12.90 \pm 0.27$ Mpc, hence $\mu = 30.55 \pm 0.05$ mag. Crook et al. (2007) determined a distance of 13.36 Mpc, equal to $\mu = 30.63$ mag. The HyperLeda catalogue reports a radial velocity corrected for Virgo Cluster infall $V_{Vir} = 793 \pm 2$ km s^{-1}, hence a distance $d = 12.0^{+10.6}_{-5.6}$ Mpc and $\mu = 30.40 \pm 1.37$ mag.

Theureau et al. (2007) gave three different distance estimates of the host galaxy through photometry in 3 NIR bands, and applying the Tully-Fisher (TF) relation: $d = 11.4$ Mpc from J observations, $d = 11.5$ Mpc from H, $d = 12$ Mpc from K, providing μ 30.29±0.46, 30.31±0.47, 30.40±0.45 mag, respectively.

More recently, Tully et al. (2016) estimated $d = 6.95$ Mpc for ESO 430-

Table 3.4: Properties of ESO 430-20

α (J2000)	$08^h07^m08^s.6$
δ (J2000)	$-28°03'08".8$
morphological type	SAB(s)d
Diameter[1]	1.90×0.78 arcmin
redshift[1]	0.003402±0.000007
v_{Hel}[1]	1020±2 km s^{-1}
$v_{Virgo+GA+Shapley}$[2]	942±20 km s^{-1}
Distance Modulus[3]	30.46±0.19
A_V	1.253 mag

[1] Theureau et al. (1998)
[2] Mould et al. (2000)
[3] adopted

20, corresponding to $\mu = 29.21 \pm 0.54$ mag, obtained from the TF relation, calibrated on a sample of galaxy clusters. The discrepancy with the previous determinations is very large, so we do not take it in account this result in the choice of the distance to adopt.

For the distance, the mean of the three TF determinations obtained by Theureau et al. (2007), and the two kinematical velocities reported in Tab. 3.2.2 are considered. We hence adopt $d = 12.37 \pm 1.07$ Mpc and $\mu = 30.46 \pm 0.19$ mag through-out this thesis.

3.2.4 Reddening

The Galactic reddening A_V, from Schlafly et al. (2011), is reported in Tab. 3.4. Assuming $R_V = 3.1$ (Fitzpatrick, 1999), a colour excess $E(B-V) = 0.404$ mag is derived. We adopted the Cardelli, Clayton & Mathis (1989) extinction law. The extinction is quite large due to the low Galactic latitude of the galaxy ($\sim 2.3°$). This makes the reddening value very uncertain. We warn that the inaccuracy of the Schlafly extinction maps can lead to inaccuracy on the intrinsic distance and absolute magnitude of the object.

On the other hand, we are not able to estimate the internal reddening of the host galaxy. We notice that the spectra do not show the narrow Na ID doublet features at the redshift of the host galaxy, because of the modest flux of the continuum at these wavelengths. The host galaxy reddening is hence assumed to be negligible, which is consistent with the location of the SN in the outskirt of ESO 430-20.

Chapter 4

Observations and data reduction

4.1 Photometry set-up

Johnson-Cousins *BVRIJHK*, Sloan *ugrizy*, narrow Hα filter and unfiltered photometric images were obtained with a large number of observing facilities, whose technical notes are summarized in this chapter. For the photometry, we used:

- The PROMPT facility, located at CTIO, consists of six 0.41-m Ritchey-Chrétien robotic telescopes developed by the University of North Carolina. They are installed on rapidly slewing mounts, ideal to respond rapidly to GRB alerts (Reichart et al., 2005). The optical imagers are Alta U47+s by Apogee, which uses a back-illuminated E2V 1024×1024 CCDs with a 10' field of view (FOV) and a pixel scale of 0.6"/pixel. Sloan *u'g'r'i'z'* and Johnson *BVRI* filters are available. The filters are positioned in 2 wheels. Clear filter is also available.

- The TRAnsiting Planets and PlanetesImals Small Telescope (TRAPPIST) is a robotic 0.5-m Ritchey-Chrétien telescope located at ESO La Silla Observatory (Gillon et al., 2011). The instrument is a high-quality, Peltier-cooled commercial camera equipped with a Fairchild 3041 back-illuminated 2k×2k CCD. The pixel scale is 0.64"/pixel, the field of view is 22'×22'. It was installed in 2010, with the goal of studying exoplanets and comets. Johnson-Cousins *BVRI* filters are available.

- The New Technology Telescope (NTT) 3.6-m telescope at La Silla is equipped with the ESO Faint Object Spectrograph and Camera (EFOSC2) attached at the Nasmyth B focus[1]. It is used for low resolution spectroscopy and imaging. The detector of the instrument is a

[1] https://www.eso.org/sci/facilities/lasilla/instruments/efosc.html

Loral/Lesser CCD, thinned, AR coated, UV flooded with 2048×2048 pixels and a pixel size of 0.12". The filter wheel contains Bessell *UBVR*, Gunn *griz*. From the NTT telescope we used also the Son of Isaac (SOFI), a NIR spectrograph and imaging camera, with a HgCdTe 1024×1024 pixels detector.

- The Southeastern Association for Research in Astronomy (SARA) is a consortium of colleges that operates some remote facilities, including a 0.6-m telescope on Cerro Tololo, in Chile (Keel et al., 2017). The instrument is equipped with a 2048×2048 pixel E2V CCD. The pixel scale is 0.44"/pixel, with a FOV of 15'. The camera is cooled to a temperature of −110°C. The filter set include Johnson *UBVRI* and *SDSS ugriz*.

- The SMARTS 1.3-m Cerro Tololo Inter-American Observatory (CTIO) telescope, with the ANDICAM detector. Two instruments can perform optical and NIR images. The CCD is 1024×1024 pixels wide, and has a pixel scale of 0.37"/pixel.

- The Gemini-South 8.1-mtelescope at Cerro Pachón, with the GMOS instrument, that is an imager, long-slit and multi-slit spectrograph, with a FOV of over 5.5 square arcminutes. It is equipped with a EEV CCD, with a pixel scale of 0.08"/pixel.

- The 1.2-m "S. Oschin" Schmidt telescope at Palomar Observatory, during the Palomar Transient Factory (PTF, PI Law) survey. The survey is performed with a 12k×8k CCD mosaic. The pixel scale is 0.1"/pixel. These data were retrieved through the web interface `http://irsa.ipac.caltech.edu/applications/ptf/`.

- The 1.8-m telescope on Haleakala, Hawaii, during the Pan-STARRS 1 (PS1) survey (Chambers et al., 2016; Magnier et al., 2016), with the Gigapixel Camera 1 (GPC1). The camera is composed of an array of 60 back-illuminated CCDs, with a 7 square degrees field-of-view. The pixel scale is 0.258"/pixel. The survey is performed with *grizy* filters.

- The European Southern Observatory (ESO) 2.6-m Very Large Telescope (VLT) Survey Telescope (VST) at Cerro Paranal[2], with OMEGACAM. The camera is composed of a mosaic of 32 2k×4k pixels CCDs, with a total of 268 megapixels and a field of view of 1 square degree. The pixel scale is 0.215"/pixel. Up to 12 filter can be used. The camera is cooled down to −140°C.

[2]during the VST photometric Halpha and broad-band survey of the Southern Galactic Plane (VPHAS+, program ID 177.D-3023, PI Drew).

4.2 Spectroscopy set-up

We obtained 5 optical spectra of SN 2013gc with the following two instrumental configurations:

- The 4.1-m "SOAR" telescope at CTIO, with the Goodman Spectrograph[3] at CTIO (PI F. Bufano). It has a 7.2' diameter FOV (with a 0.15 "/pixel scale), and can take spectra at various resolutions from the atmospheric UV cutoff all the way out to 850nm. It employs Volume Phase Holographic (VPH) gratings. Two cameras are offered: a Blue and a Red Camera; we used the Red Camera. The Spectrograph can also do imaging with *SDSS* and Bessell filters. The Red Camera is equipped with a 4096×4112 pixel, back-illuminated, deep-depleted, astro-multi-2 coating, E2V 231-84 CCD. The CCD has a high and almost flat Quantum Efficiency (>90%) through the entire optical range, from 400 to 800 nm.

- The Du Pont telescope at Las Campanas Observatory with the WFCCD/ WF4K-1 instrument[4] (PI P. Lira). The camera covers a 25' field, with a scale of 0.484"/pixel. The detector has 4064×4064 pixels.

The acquisition images of these instrument were also used for photometry. The first spectrum, taken one day after the discovery, was used for the spectral classification. The second spectrum is dated 2013 November 17, during the first dimming phase. The last two spectra were obtained after the second luminosity peak, on 2014 May 5 and May 12. On 2014 May 12 a mid resolution spectrum around the Hα region was also taken.

4.3 Photometric data reduction

For the data reduction, we used a dedicated pipeline called SNOoPY (Cappellaro, 2014). SNOoPy is a package designed to facilitate the task of producing SN light curves from multi-band photometric observations obtained with a generic collection of telescopes. It is developed by Enrico Cappellaro. A package description can be found at `http://sngroup.oapd.inaf.it/snoopy.html`. SNOoPY is a collection of python scripts calling standard IRAF[5] scripts through `pyraf`. The goal is to make source extraction also in complex background environments, measuring the source magnitude via PSF fitting. A key feature is the ability to automatically match and compare the photometry of stars in the SN field obtained in different nights (and typically with many different telescopes). This allows us to calibrate

[3] http://www.ctio.noao.edu/soar/content/goodman-red-camera
[4] http://www.lco.cl/telescopes-information/irenee-du-pont/instruments/
[5] http://iraf.noao.edu/

a sequence of local standard stars and to adjust the photometric zero point for non photometric nights.

The images must be first pre-reduced (corrected for bias, flat-field, overscan and dark current, if necessary). The starting operation is the compilation of a file, called SNOOPY.DEFAULT, that contains all necessary information about the telescope and the mounted camera, such as site location, the dynamical counts range of the CCD (i.e. the saturation level), gain, read-out noise (RON), filter, Julian date and time of the observation, pixel scale. A file that contains the celestial coordinates of the SN is also needed.

The first operation consists in combining all the images of SN field, taken in the same night, with the same telescope and filter. This is done with `ecdither`. The software ask the user to choose more than 3 stars in a reference image and select the same stars in all other images. The images are then combined in a stacked frame, taking in account for dithering, rotation and image scale. This is useful when the source is particularly faint to measure the signal to noise ratio (SNR).

The following step is measuring the seeing of the image with `ecseeing`. The task can do it interactively or automatically. The program picks up some bright, non-saturated stars in the image, possibly isolated, to calculate the mean FWHM in pixel and, adopting the pixel scale reported in "SNOOPY.DEFAULT", convert it to arcseconds.

If the image is not astrometrically calibrated, we astrometrize it with `ecastro`. The software asks to select more than 2 stars in the image. Then, it loads a star catalogue of astrometric standards, with precise coordinates (USNO-A2.0 or 2MASS catalogues). The user have to find the same stars previously identified in a new image, whilst the stars of the catalogue are shown in the display. The software performs the calculation to match the real coordinates of the stars with the image positions. If the rms is larger than 0.3", the astrometric calibration is considered bad, and we repeat the operation changing the identification of the reference stars.

The most important task is `ecpsf`, which constructs the PSF model using the stars in the image. The PSF is obtained by averaging the profiles of isolated field stars automatically (or manually, if requested) selected in the observed frame. The fitted target is removed from the original frames, then a new estimate of the local background is derived, and the fitting procedure is iterated. In typical runs, the residuals are visually inspected to validate the fit. Some parameters are required to optimise the measurements. The first one is the distance threshold: if a companion is located at a distance smaller than the threshold (measured in units of the seeing FWHM), the star is rejected from the PSF model. This threshold is fixed to avoid contaminants that can degrade the optimal shape of the PSF. The second is the brightness threshold: the program accounts only for the stars with a SNR higher than the imposed limit. Finally, the software automatically identifies and excludes saturated stars, bad pixels, cosmic rays or background galaxies, that are

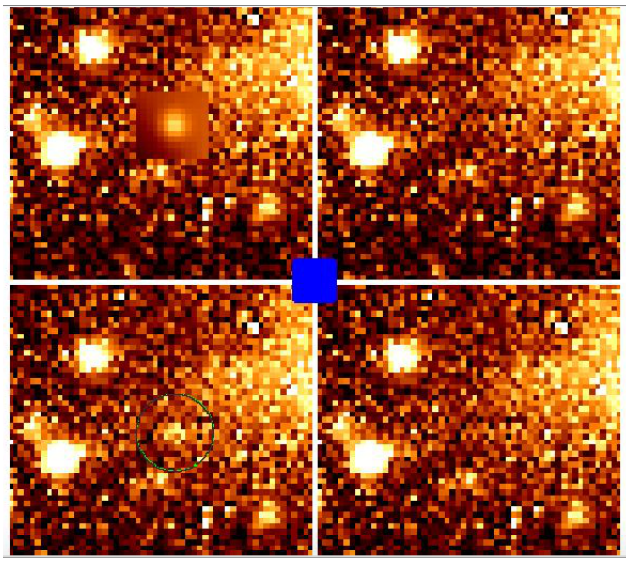

Figure 4.1: An example of the output of `ecsnfit`. On the left-bottom panel the identification of the source. In the top left the source flux is modelled. In right panels the image after the subtraction of the SN model (top), and after the subtraction of SN model+background (bottom).

rejected in modelling the PSF. We modified the parameters, so that about 100 stars are used to model the PSF in each image. At the end of the process, the program creates a catalogue with coordinates and instrumental magnitudes of all measured field stars.

The photometry of the source is obtained from `ecsnfit`. The source magnitude is measured using the PSF-fitting technique, first subtracting the sky background estimated using a low order polynomial fit (typically, a 2nd order polynomial) on the surrounding region. The task creates two concentric boxes centered on the coordinates of the object, and we can choose the sides of the boxes. The inner box delimits the region within which we measure the flux of the object. The region between the inner and the outer box is used for computing the mean counts of the sky background, to be subtracted from the SN flux. In Fig. 4.1 an example of the output of the program is shown. Error estimates are obtained through artificial star experiments (with `ecarterr`) in which a fake star, of magnitude similar to that of the SN, is placed in the PSF-fit residual image in positions close but not coincident to that of the real source. The simulated image is processed through the PSF fitting procedure, and the rms of measurements out of a number of experiments, is taken as an estimate of the instrumental magnitude error. This is combined (in quadrature) with the PSF-fit error.

If the object is not visible in the frame, because the atmospheric con-

ditions are not optimal or the source is too dim, an upper limit to the luminosity is derived with `eclimit`. The procedure subtracts a simulated star from the image with a SNR given by the user. We adjusted this value until an over-subtraction became clearly visible in the frame. All passages from `ecpsf` to `ecarterr` or `eclimit` can be done in a single step using `ecall`. This is a faster way, but the user has less control on the operations performed by the software.

The magnitudes we measure are instrumentals, and are calculated from the counts of electrons. Then we convert them into standard magnitudes in a defined photometric system. For this aim we calibrate them through the comparison with catalogue standard stars of well-known magnitudes. For this goal, some standard fields have been observed during photometric nights. Then we calculate zero-points and color-terms of each night. The calibrated apparent magnitude of the source is calculated from the equation:

$$\Delta m = m_0 - m = ZP + CT \times (colour) \tag{4.1}$$

for a given pass-band, where Δm is the difference between the measured and calibrated magnitudes of the standard star, m_0 is the reference magnitude of the standard star, m is the instrumental magnitude obtained for the star, ZP is the instrumental zero point and CT is the color term. Observations in two different filters are needed, to determine the color term. ZPs and color terms of the nights are derived from the images taken during photometric nights using `ecph` and with a set of standard stars from Landolt (1992) or SDSS catalogues.

With `ecrefstar`, we create a local sequence of calibrated stars, directly from the SN field images. Alternatively, the local sequence can be obtained using the `eczeropoint` task. The latter permits to produce a local standard Sloan sequence (if the SN field is covered by the SDSS survey). An *UBVRI* Johnson-Cousins sequence is obtained by converting the Sloan magnitudes, if the information on the $g-r$ or the $r-i$ colour is available, with the Chonis & Gaskell (2008) relations:

$$\begin{aligned} B &= g + (0.327 \pm 0.047)(g-r) + (0.216 \pm 0.027) \\ V &= g - (0.587 \pm 0.022)(g-r) - (0.011 \pm 0.013) \\ R &= r - (0.272 \pm 0.092)(r-i) - (0.159 \pm 0.022) \\ I &= i - (0.337 \pm 0.191)(r-i) - (0.370 \pm 0.041) \end{aligned} \tag{4.2}$$

Because the observations are spreadly distributed in time, the seeing and transparency of the sky change from night to night, we have to correct the magnitudes for ZPs obtained in non-photometric nights.

To calibrate the magnitudes of the local standards measured in non-photometric nights the package used is `ecnightcal`. It compares these magnitudes with those obtained in photometric nights, and calculates the shifts to apply to the ZPs.

Finally the calibrated apparent magnitudes are generated by the command `ecsncal`, who requires the CTs and the correction to be applied to the instrumental magnitudes. The output is a file containing, for each night, the standard magnitudes in all filters used. With this output file, we can construct the light curve, that is discussed in Chapt. 5.

Only a single epoch of J, H and K imaging of the SN, along with a few additional NIR frames of the SN field taken before the explosion, are available. Clean sky images were obtained by median-combining multiple dithered images of the field, and consequently subtracted to individual images. Sky-subtracted images were finally combined to increase the SNR. PSF-fitting photometry was also performed on the NIR sources, and the final SN magnitudes were calibrated using the 2MASS catalog as reference.

4.4 Spectroscopic data reduction

The spectra of SN 2013gc were reduced using standard IRAF[6] packages. For each night, standard calibration frames were taken: bias, flat-fields, along with spectra of comparison arc lamps and spectro-photometric standard stars. The latter two are necessary for wavelength and flux calibrating the SN spectra.

Firstly, we trimmed the flat-field frames, removing the overscan strip and keeping only the portion without spurious reflections. Then, we trimmed the other images obtained in the same night with the same instrumental configuration. The task for trimming the 2D spectra, and correcting for overscan/bias and normalised flat field is `ccdproc`, contained in the package `noao > imred > ccdred`. The bias frames were median-combined to create a Master-bias. This Master-bias was removed from the scientific and from the flat-field images. The resulting flat-field frames were averaged into a Master-flat. The Master-flat was normalized to to the unity using the task `response`. The spectra of the SN, the standard star and the lamp were divided by the normalized Master-flat.

The 1D spectra were optimally extracted from the 2D images with the task `apall`, while the spectra of the comparison lamps were extracted with `apsum`. For the SN we extracted the source with a narrow aperture, to increase the signal-to-noise ratio (SNR) and reduce the contaminants from the surrounding regions of the galaxy. The much more luminous spectra of the standard stars were extracted using a larger aperture, to avoid flux losses from the star.

The wavelength calibration was performed through the spectra of comparison lamps, identifying the lines using a line atlas usually available in

[6]IRAF is distributed by the National Optical Astronomy Observatory, which is operated by the Associated Universities for Research in Astronomy, Inc., under cooperative agreement with the National Science Foundation.

the manual of the instruments. The IRAF task used is `identify`. As first step, we marked the brightest lines at the extremes of the lamp spectrum, a preliminary dispersion function was obtained with a low-order polynomial fit. With `reidentify`, all known line positions of the lamp were loaded, and a better dispersion function was derived. The task `refspec` assigned the reference spectrum of the lamp to the scientific spectra, while `dispcor` performed the wavelength calibration to the spectra of the objects. The resulting wavelengths of some sky emission lines, such as [O I] λ 5577, $\lambda\lambda$ 6300,6364 and Na I D $\lambda\lambda$ 5890,5896, were checked using the IRAF task `splot`. If necessary, we rigidly shifted the spectra until the observed wavelengths of the night sky lines matched the laboratory values.

The task `standard` allowed to calibrate the specific flux of the spectra. The program needed the calibrated specific magnitudes of the standard stars, that was downloaded from the ESO website[7]. The atmospheric extinction curve of the observing site was also required; for the CTIO observatories the curve was contained in the IRAF database. The task `sensfunc` created the observed sensitivity function. With `calib`, we flux-calibrated the scientific spectra. The spectral fluxes were scaled to match the R-band photometry of the closest night. The comparison with the broad-band photometry was performed using the task `calcphot`.

Strong telluric absorption bands are present in the red spectral region, in the intervals 6850-6930 Å, 7145-7335 Å, 7570-7750 Å, 9275-9680 Å. Using the spectra of the spectroscopic standard taken during the night and the package `telluric`, we could remove the telluric band contamination. Finally, the five spectra are corrected for redshift and reddening, adopting the values of z and A_V given in Tab. 3.2.2, using the IRAF tasks `dopcor` and `deredden`.

[7] `https://www.eso.org/sci/observing/tools/standards/spectra/stanlis.html`

Chapter 5

Photometry of SN 2013gc

5.1 Light curves

Our photometric follow-up campaign of SN 2013gc spans 7 years, starting from March 2010. The first detection of the SN is on 2013 August 26, ∼1.5 months before the discovery announcement. With only one observation during the rising phase, it is not possible to precisely determine the explosion epoch. The last non-detection is dated 2013 June 19, hence the SN must be exploded between the above two dates. As we will detail in Sect. 7, we assume 2013 August 16 (MJD 56520) as explosion date. The object has been followed for about 2 years, up to June 2015. Pre-explosion images and those obtained at very late phases are unfiltered. Clear filter magnitudes from PROMPT are treated as Cousins R-band magnitudes, because the wavelength efficiency peak of the detector is similar to that of the R filter response curve. The multi-band optical magnitudes are reported in Appendix, in Tab. 8.1 and the infrared (IR) ones in Tab. 8.2 for, while unfiltered magnitudes are listed in Tab. 8.3.

The photometric coverage of the SN evolution in the *BVRIJHK* and *gzy* bands is shown in Fig. 5.1 and Fig. 5.2. Magnitudes are not corrected for the line of sight extinction. We assume MJD 56544±7 as an indicative epoch for the maximum luminosity, that is 4 days before the brightest V band magnitude (MJD 56548) and 20 days before the brightest point in the I band (MJD 56564). This agrees with the estimate of Antezana et al. (2013).

The light curve shows a fast linear decline after maximum, with a rate of 6.6 ± 0.2, 7.5 ± 0.3 and 6.1 ± 0.2 mag $(100\ \mathrm{d})^{-1}$ in the V, R and I bands, respectively. Such decline rates are typical of the 'Linear' subclass of type II SNe (Valenti et al., 2016). Two EFOSC2 observations has been performed 3 and 4 days after our estimated maximum, when the SN was at $V = 15.1$ mag (hence, $M_V \sim -16.6$ mag).

The initial linear decline is followed by a slower decline in all bands. This phase, lasting ∼20 days, is well sampled in the R band with a slope of 1.02 ± 0.11 mag $(100\ \mathrm{d})^{-1}$. This decline slope is consistent with that expected from the decay rate of ^{56}Co into ^{56}Fe. The second decline ends at phase ∼90 days. Assuming that this short-duration phase is powered by radioactive decays, this fraction of the light curve will be used to guess an upper limit on the ^{56}Ni mass ejected by SN 2013gc (see Sect. 7). But, we will note in Sect. 6 that the CSM/ejecta interaction features are present in every phase of the SN evolution.

Later on, the light curve shows a sort of plateau at around 20.5, 19.0 and 18.5 mag in the V, R and I bands, respectively. The plateau lasts about 70 days. We believe that the abrupt stop of the luminosity decline at +120 d marks the onset of a new, stronger ejecta-CSM interaction episode, that hereafter will become the primary source of energy for the SN. Later on, a rebrightening in the R and I bands is observed, with a rise of 1 mag. A secondary peak in I-band is reached on MJD 56738 (+194 days). Then, the light curve rapidly fades.

From +300 to +630 days, the light curve presents a well-defined linear decay, with a slope of 0.43 ± 0.05 mag $(100\ \mathrm{d})^{-1}$, flatter than the decay rate of ^{56}Co. However, the SN is detected only in the R band. Around 2 years after the explosion, due to the faintness of the object, the photometric measurements are very close to the detection limits.

The SN field was imaged again by the DECam Plane Survey (DECaPS, PI Rau), with the 4-meter 'V. Blanco' telescope at CTIO, between January and April 2017. From this survey, we collect 3 stacked images in the Sloan grz bands, one of which is shown in Fig. 5.5. The images are calibrated using the PANSTARRS DR1 catalog. We detect a faint source at the position of SN 2013gc at $g = 23.57 \pm 0.22$ mag, $r = 22.63 \pm 0.18$ mag, $z = 22.62 \pm 0.24$ mag. These detections are over 1 mag fainter than those of the outbursts observed in 2010 to 2013, and this can be used as an argument to support the terminal explosion of the progenitor star.

5.2 Colour curves

We compare the $(B-V)_0$, $(V-R)_0$ and $(R-I)_0$ colour curves of SN 2013gc with those of type IId SN 1994aj (Benetti et al., 1998), SN 1996L (Benetti et al., 1999), SN 1996al (Benetti et al., 2016) and SN 2000P in Fig. 5.3. The photometry of SN 2000P is published in Reguitti et al. (2018). For SN 1996al, we used the reddening and the distance reported in Benetti et al. (2016) ($\mu = 31.80 \pm 0.2$ mag, $E(B-V) = 0.11 \pm 0.05$ mag), while for SN 1994aj, SN 1996L and SN 2000P we adopted the values reported in Tab. 3.1.1. All values are obtained with the assumption $H_0 = 73$ km s^{-1}Mpc^{-1}.

Soon after maximum, the objects have colour indices around 0 mag. At

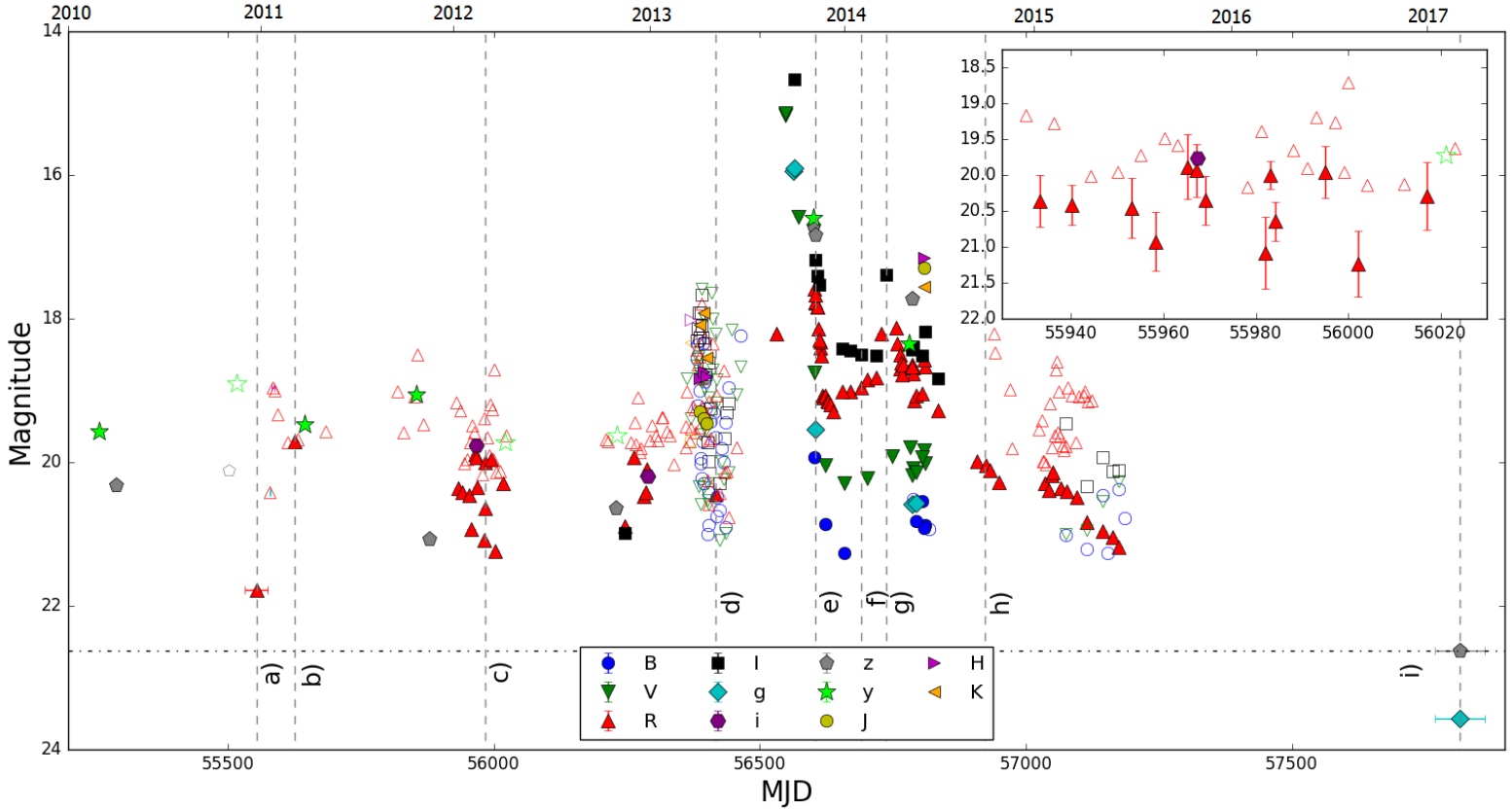

Figure 5.1: The full 7-year coverage of the optical and NIR light curves of SN 2013gc. For sake of clearness, error bars are not reported here. A blow-up on the light curve of the transient during the 2012 variability period (see Sect. 5.4) is shown in the top-right inset. The purple, dashed vertical lines mark the epochs imaged in the panels in Fig. 5.5. The horizontal line indicates the magnitude of the brightest detection of 2017, showing that the object has faded with respect to the pre-SN eruptive-phase.

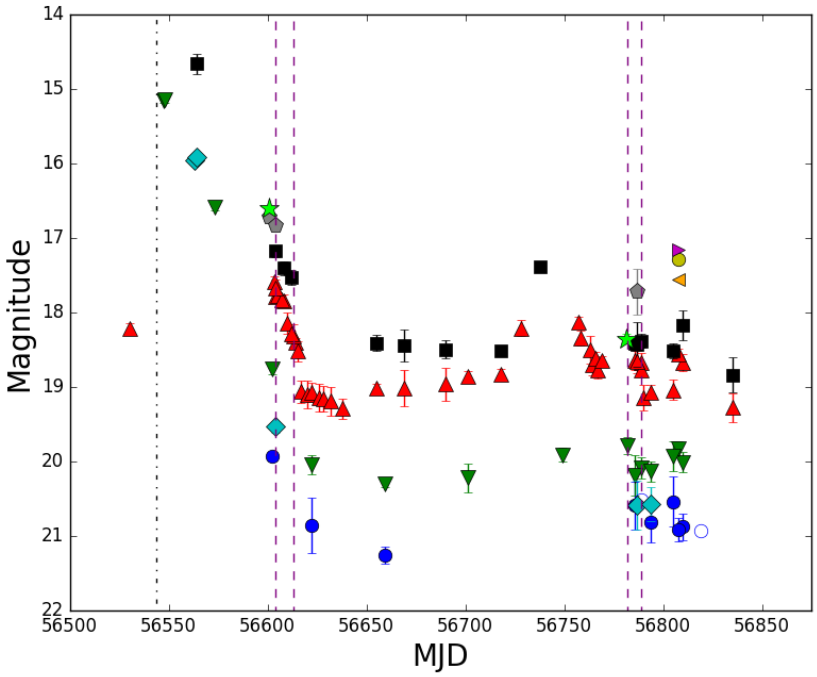

Figure 5.2: Blow-up on the post-explosion evolution of the light curve of SN 2013gc. The purple, dashed lines mark the epochs of the available spectra, while the black dot-dashed line marks the date of the assumed maximum. Upper limits are indicated as empty symbols. For each band, a different symbol is used.

early phases the $(B-V)_0$ and $(V-R)_0$ colour curves of our SN IId sample shows an evolution to redder colours which is initially fast (up to 60 d), and then slower (up to 150 d), as expected from a cooling photosphere (see Fig. 5.3). At 150 d the $(V-R)_0$ colour reach $\sim$1 mag. The $(R-I)_0$ colour for SN 1996al, SN 1996L and SN 2000P remains almost flat around 0 mag. SN 2013gc seems to match the average behaviour of SNe IId. However, the colours curves have not a monotonic trend and, at late phases (>240 days), oscillations of 0.3 mag are observed, but the error bars are quite large.

5.3 Absolute light curves

With the distance adopted in Sect. 3.2.1 and the extinction reported in Tab. 3.4 for SN 2013gc, we obtain $M_I \sim -16.5 \pm 0.25$ mag for the brightest observation (without accounting for the error on the reddening and on the host galaxy extinction). This value is close to the mean luminosity of 'normal'

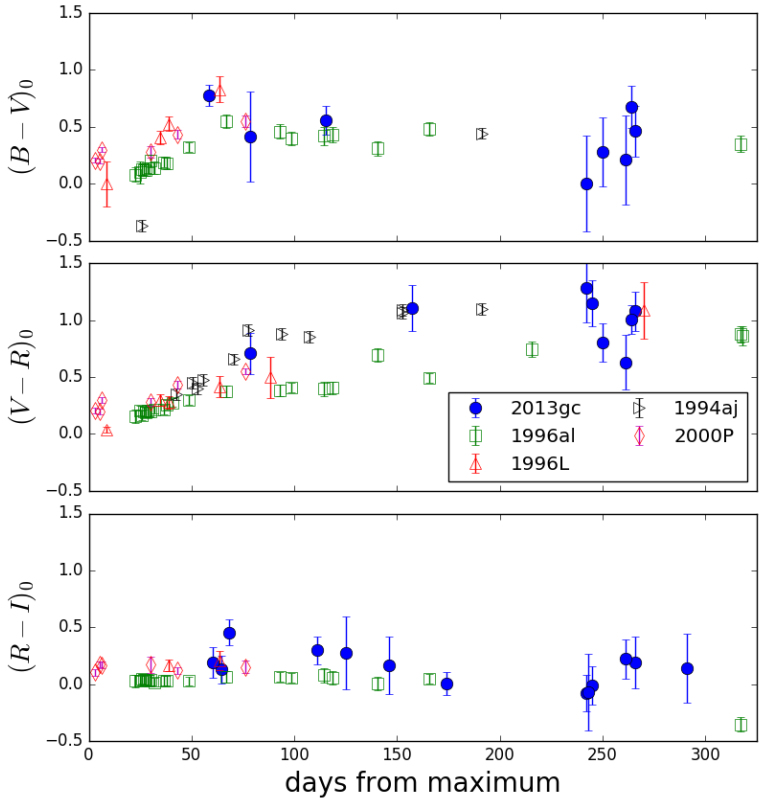

Figure 5.3: Colour curves of SN 2013gc (blue circles), corrected for extincion, shown with those of the comparison SNe 1996al (green squares), 1996L (red triangles), 1994aj (black triangles) and 2000P (purple diamonds). The phase of SN 2000P is from the discovery date, not from the maximum, that probably was not observed (Fig. 3.2). $(B-V)_0$ is in the upper panel, $(V-R)_0$ in the middle panel and $(R-I)_0$ in the bottom panel. Error bars are reported for all objects.

SNe IIL $\langle M_B \rangle = -16.8 \pm 0.5$ (Valenti et al., 2016) but, as discussed before, our brightest detection is not coincident with the real maximum.

The R-band absolute light curves of SN 2013gc and the type IId SNe 1996al, 1996L, 1994aj and 2000P are compared in Fig. 5.4. From this comparison, we note that the whole absolute light curve of SN 2013gc is fainter than those of comparison SNe by about 2 mag (but see Chapt. 7). However, the decline (between 40 and 70 days after maximum) of SN 2013gc is quite similar to the average of the sample.

Because of the low Galactic latitude of the host galaxy, the Milky Way

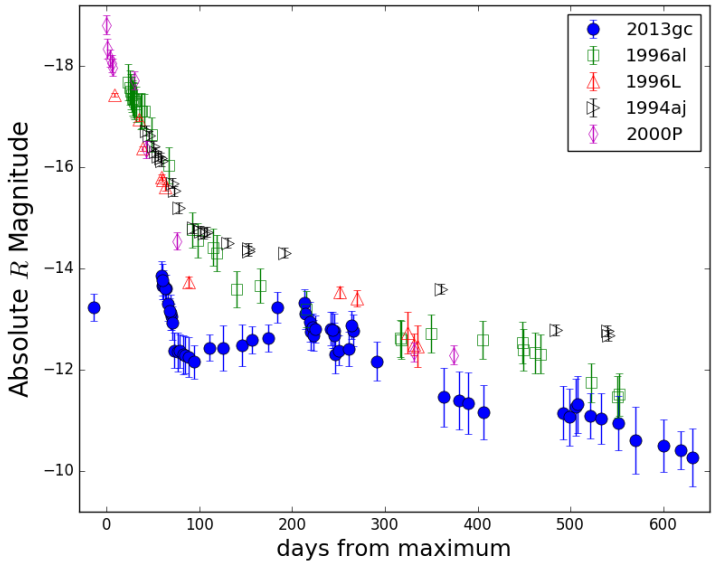

Figure 5.4: Absolute R-band light curves of SN 2013gc (blue circles) and comparison objects. Error bars are reported. The different symbols indicate the same SNe as in Fig. 5.3.

extinction is uncertain. Shifting upwards SN 2013gc by 2 mag, a fair agreement between SN 2013gc and other SNe IId would be found, with the exception of the late rebrightening of 1 mag (lasting 40 days) which remains a distinctive feature of SN 2013gc.

The source detected in the DECam images in 2017, with $M_r \approx -8.9$ mag and an intrinsic colour $(g-r)_0 \approx 0.5$ mag, can be a contaminant background H II region or even a residual signature of the SN.

5.4 Analysis of pre-SN data

The SN field was sparsely monitored for more than 3 years before the explosion. We found several archival images taken between 2010 and early 2013 with a detection of a source at the SN position, although in some cases with large error bars. This is very likely an indication that the SN 2013gc progenitor experienced a long-lasting luminosity variability, most likely a major eruption started a few years before the SN explosion. Selected secure detections, along with images witnessing the principal phases of the SN evolution, are shown in Fig. 5.5.

The PS1 survey sparsely monitored the field between 2010 and 2013. The first PS1 images of March 2010, in the z and y bands, show a source

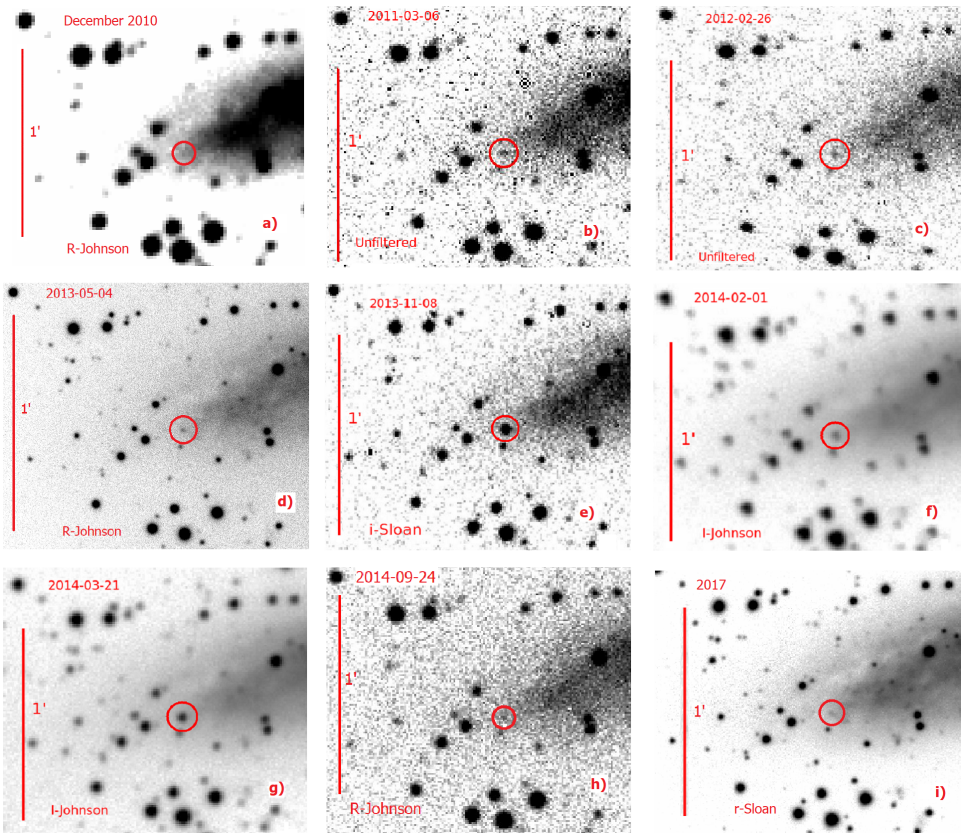

Figure 5.5: Images of the field of SN 2013gc obtained at selected crucial phases. Panel a) the stacked December 2010 frames from the PTF survey. b) The 2011 March 6 brightening. c) The 2012 February 26 flare. d) The Gemini image witnessing the 2013 May 4 detection. e) The I-band luminosity peak. f) An I-band image during the plateau. g) The I-band image at the second peak. h) A late R-band detection after the second peak. i) The deep post-explosion r-band image of the DECaPS survey.

with a magnitude of about 20. Then, a stack of the nine best-quality frames taken between 2010 December 2 and 2011 January 14 from the PTF survey has been produced. In this deep image, we detect a very faint source at R ∼21.8 mag, which is close the bona-fide limiting magnitude of the survey. The absolute magnitude of the source is only $M_R \sim -9.65$ mag. From the same survey, we combine the images obtained from 2011 January 17 to 19, and from 2011 January 21 to 27. The seeing of those nights was quite poor (3 arcsec), and only upper limits are obtained.

We found a few images taken later in 2011, with only one detection on 2011 March 06 (MJD 55626). For this event we estimate $M_R = -11.74 \pm 0.35$ mag, although we cannot constrain the duration of the outburst. In fact, in frames obtained 12 days before and 6 days after the burst, nothing is visible at the same magnitude.

On early 2012, the field was well monitored, and a few additional sparse detections are found (see the top-right box in Fig. 5.1). This provides additional evidence of the long-lasting photometric instability of the SN progenitor. The faintest detections are at 21 mag, corresponding to $M_R \sim -10.5$ mag, but in other cases the source has an apparent mag between 20 and 21. The source has also been detected by PS1 on 2011 October 20 in the y band, at 19 mag, which is almost 3 mag brighter than the faintest PTF detection measured 9-10 months before. We now describe a sequence of events: on 2012 February 25 (MJD 55982), the source is hardly visible. The day after, the object is in flare, showing a brightening of 1 mag. Then, on 2012 February 27, the transient has faded again by 0.5 mag. This sequence highlights a scenario with a short-duration flares occurring during a long eruptive phase. The absolute magnitude estimated for this flare is $R = -11.41 \pm 0.40$ mag, similar to that observed in LBV-like outbursts, such as SN 2000ch (Wagner et al., 2004). The upper limits measured in a number of lower-quality images are not very deep (<20 mag), hence they are not very constraining.

After some months without images due to the heliac conjunction, the monitoring campaign restarted in late 2012, and the object was detected in several frames. In one of them, on 2012 December 1, the object reaches $M_R = -11.51 \pm 0.50$ mag. In March 2013, the explosion of SN 2013ak in the same galaxy triggered a vast observational campaign, and tens of multi-band images of the field are hence available. In one of those images, taken with the Gemini South telescope, a brightening is clearly revealed on 2013 May 4 at $R = 20.45$ mag ($M_R \sim -11.00 \pm 0.23$ mag). Also this event is probably a short-duration flare. In fact, the source is not detected in images taken one day before and one day after. However, the quality of these images, taken with the PROMPT telescopes, is lower than the image of the Gemini South telescope. We remark that the peak luminosity of the four impostor events described above is very similar. This behaviour is remarkably similar to that observed in 2008-2009 by the same star that produced SN 2000ch (Pastorello

et al., 2010). After June 2013, the region was again in heliac conjunction. Then, when the field became again visible at around mid-August 2013, the SN was already visible.

Chapter 6

Spectroscopy of SN 2013gc

The spectroscopic observational campaign of SN 2013gc provided 5 spectra, between November 2013 and May 2014. Technical details of the five spectra are reported in Tab. 6.1.

6.1 Line identification

The low-resolution calibrated spectra, with line identification, are shown in Fig. 6.1, while the medium-resolution spectrum is plotted in Fig. 6.2.

A weak, red continuum (T_{bb} ∼4000 K) is present in the early spectra. Absorption features of metals, and Balmer lines in emission are also observed. Hα is the most prominent feature in all spectra, and its profile is described in detail in Sect. 6.3. Hβ has a similar profile as Hα. Hγ is not clearly detected, although the spectra have a low SNR at the blue wavelengths. He lines are weak in early spectra, but become more intense later. He I λ7065 is the stongest line, followed by λ6678 and λ4922. He I 5876 is blended with the Na ID doublet in emission.

To evaluate the evolution of the He lines, we measure the flux ratio Hα/He I λ7065 in all spectra. We choose the He I λ7065 line because it is isolated and not significantly blended with other lines. In the first two spectra, the ratio is around 90 ± 10. In the +238 d spectrum, the ratio is lowered to ∼30, and in the +245 d spectra it goes down to only 18 ± 2.

We identify Fe II features (multiplets 40, 42, 46, 48, 49, 199). The Fe II (46) λ6113 line is observed in absorption at early phases, while it is in emission at late epochs. A blow-up of the first and last spectrum in the 4800-5600 Åregion with the identified lines of Fe II multiplets, is shown in Fig. 6.3.

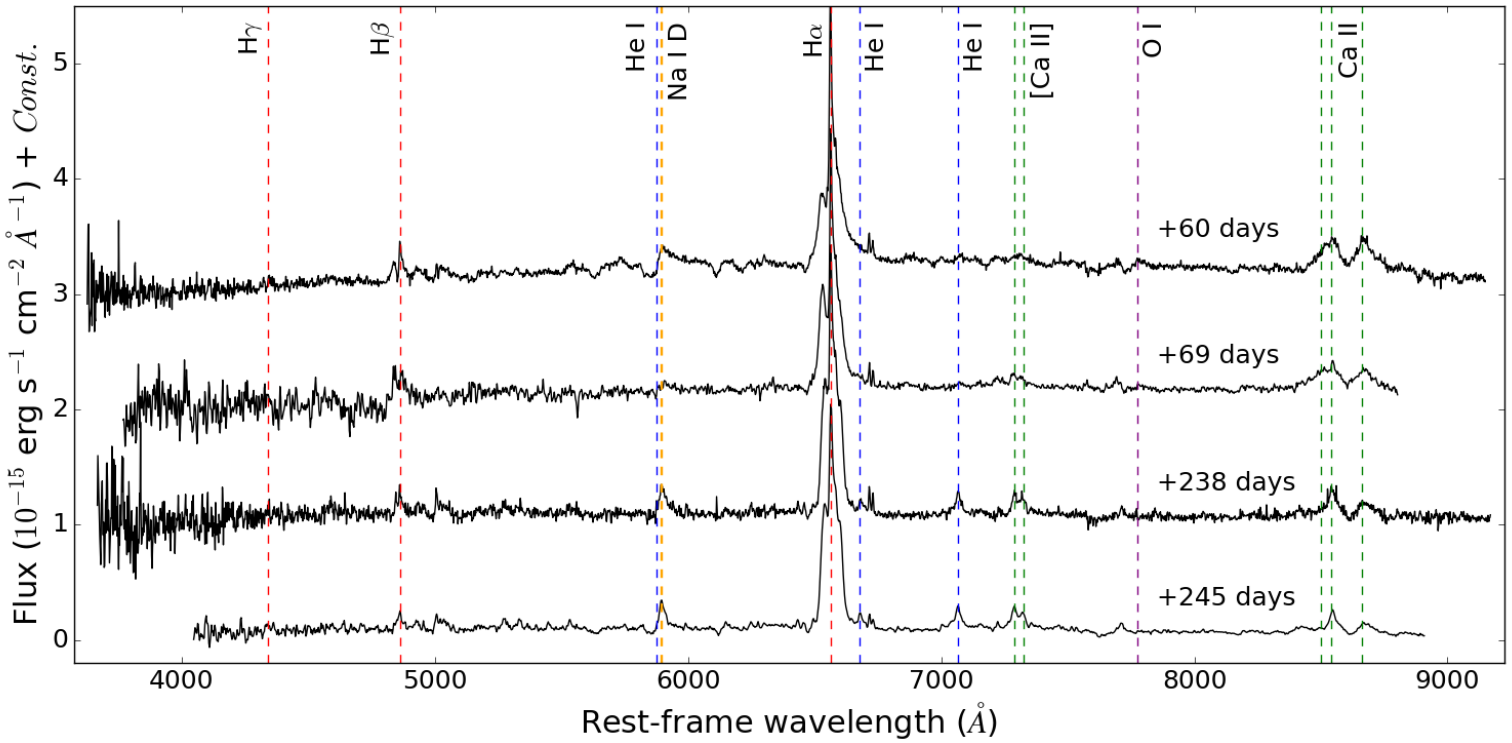

Figure 6.1: The 4 low-resolution spectra of SN 2013gc, corrected for redshift and reddening. The most prominent lines are identified in figure.

Table 6.1: Basic information of the 5 spectra of SN 2013gc. The phase is with respect to the adopted maximum (MJD 56544). To evaluate the instrumental resolution, we measured the FWHM of the [O I] night sky lines.

Date	MJD	Phase (d)	Instrument	sky lines FWHM (Å)	spectral range (Å)	exp. times (s)
2013 November 8	56604.20	+60	WFCCD+blue grism	8.2	3620-9180	2×900
2013 November 17	56613.17	+69	Goodman Spectrograph	5.0	3765-8830	2×3600
2014 May 5	56782.09	+238	WFCCD+blue grism	7.7	3630-9200	2×1000
2014 May 11	56788.98	+245	Goodman Spectrograph	7.6	4050-8940	2×2700
2014 May 12	56789.05	+245	Goodman Spectrograph	1.7	6250-7500	2700

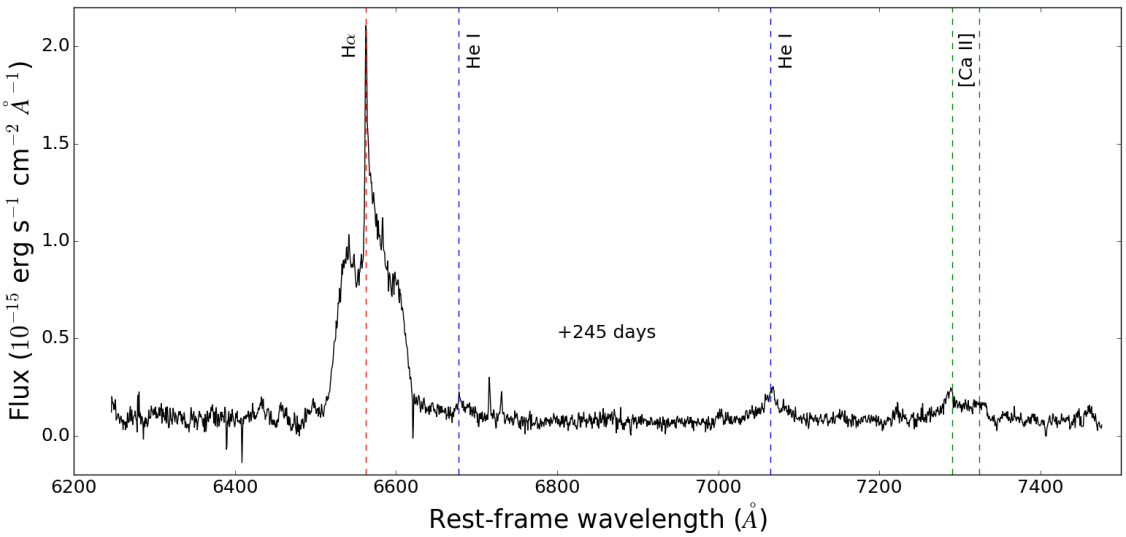

Figure 6.2: The mid-resolution spectrum of SN 2013gc, dated 2014 May 12. The spectrum covers 1200 Å around the Hα line. The main identified lines are marked.

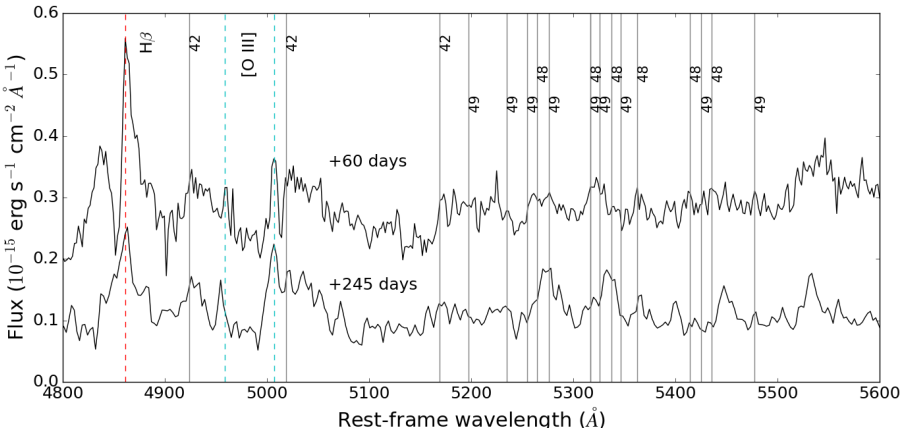

Figure 6.3: Blow-up of the +60 and +245 days low-resolution spectra in the region 4800-5600 Å. The rest-frame positions of the Fe II lines from the 42, 48, 49 multiplets are marked. Hβ and [O III] $\lambda\lambda$ 4959,5007 are also reported.

At late phases, the flux contribution of the spectral continuum is negligible, and the line profiles have changed. We identify the Ca II IR triplet lines, detected as broad emission. The FWHM of the Ca II λ 8662 line is 3400±100 km s^{-1}. There is a possible detection of O I λ7774 in the first spectrum. More in general, we note an increasing number of emission lines, especially from forbidden transitions. In particular, we identify: [N II] $\lambda\lambda$ 6548,6584 lines (although blended with the Hα line), [S II] $\lambda\lambda$ 6716,6731 lines, [Ca II] $\lambda\lambda$ 7291,7324 lines, which seem to become stronger with time. The narrow [S II] and [N II] lines likely arise from unresolved background contamination. In fact, in a 2012 image taken by the VST telescope equipped with OMEGACAM and a narrow Hα filter during the VPHAS+ survey (PI Drew), a diffuse, elongated source is visible. This object can be a foreground H II region.

6.2 Comparison with similar objects

Our spectra are compared with those of SN 1996al, SN 1996L, SN 1994aj and SN 2000P obtained at around the same phases. All spectra of SN 2000P are presented for the first time in Reguitti et al. (2018).

The early spectra of SN 2013gc are similar to those of SN 1994aj, SN 1996al and SN 1996L taken at 60-70 days after maximum, in particular with respect to the Hα profile and the Na ID P Cygni line. In all these SNe, Hα and Hβ show a narrow P Cygni absorption over a broader P Cygni component. The main difference at early times is that SN 1996L has a hotter

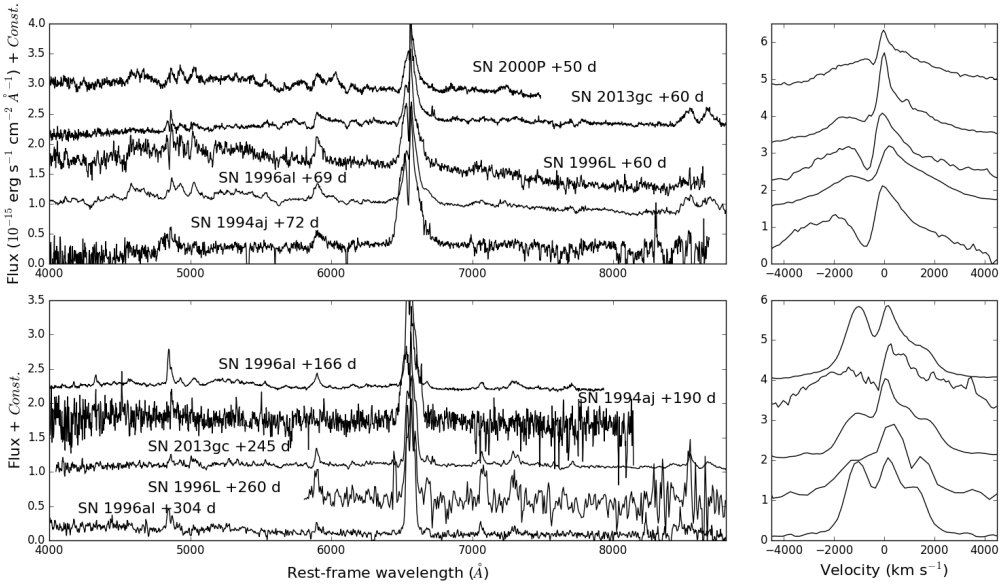

Figure 6.4: Comparison of the +60 (top) and +245 (bottom) days spectra of SN 2013gc with those of reference SNe IId at approximately the same phase. On the right panel, the same comparison is done for Hα profiles at the same epochs.

continuum, peaking around 5000 Å, giving a black-body temperature T_{bb} of ∼6000 K.

One of the most interesting comparison is with SN 2000P, which has an excellent spectroscopic dataset. As for SN 2013gc, Hα is characterized by a very narrow P Cygni absorption and an extended Lorentzian red wing. Hβ has a similar narrow P Cygni feature. Many bumps, likely due to Fe II, are observed in the spectra of both objects. It is worth comparing the spectra and the Hα profile evolution of SN 2000P (Fig. 3.1.3) with those of SN 1996al (Fig. 5 and 7 of Benetti et al., 2016). In the spectra of SN 2000P obtained a very few days after the maximum light, the blue continuum indicates a high gas temperature. Hα and Hβ show a double P Cygni feature, along with a broad emission from He I λ5876 and Na ID lines. At phase +30 days, many bumps from metals arise and the Ca II triplet becomes well visible, similar features are visible in the first spectrum of SN 2013gc. From this epoch, a blue-shifted Hα bump starts to develop at an intermediate-width, and grows in strength with time. One year after the maximum, Hα is nearly the only observable feature, and the blue-shifted component is more prominent than that at the rest frame.

The late-time spectra of SN 2013gc and SN 2000P are not sufficiently close in phase to make a reasonable comparison. A comparison of the spectra of SN 2013gc with other SNe IId at similar phases is provided in Fig. 6.4. In the comparison of early-time spectra, we note that Hβ is quite prominent, with the Balmer decrement Hα/Hβ being higher in SN 2013gc than in other SNe IId. In particular, for SN 1996al at $\sim$ +60 days, Benetti et al. (2016) found an Hα/Hβ ratio of 5, while for SN 2013gc we infer a ratio of around 10. In the late spectra the ratio increases to $\sim$20. This comparison with SN 1996al supports the possibility that the reddening in the direction of ESO 430-20 may have been underestimated.

6.3 The Hα profile

The analysis of the Hα profile can provide information on the CSM around the SN. The Hα profile is complex, and consists of multiple components (see Fig. 6.5). In the early spectra, a narrow P Cygni absorption is superposed on a broad component. The line is asymmetric, with an extended red wing. The simultaneous presence of a broad component from the fast ejecta and a narrow P Cygni profile from slow circumstellar wind is a characterizing feature of type IId SN spectra. The Hα profile shows an evolution from the early (+60 d) to the late (+245 d) epochs, with the velocities of the broader components progressively decreasing with time. In order to identify the different line components, we deblended the Hα profile, following Benetti et al. (2016). We considered the spectra obtained +69 and +245 days. The results are illustrated in Fig. 6.6, and the velocities of the different line components are reported in Tab. 6.2.

At the early epoch, the relatively broad Hα component has a velocity of 3400 km s^{-1}, which is very similar to the FWHM velocity (v_{FWHM}) of the Ca II λ8662 line. The FWHM of this component can be considered representative of the SN ejecta velocity. In the late spectrum, Hα has been deblended using 3 distinct intermediate-width emission components, with comparable v_{FWHM} ranging between 1300 and 1800 km s^{-1}. These components correspond to 3 distinct emitting regions: a first (blue shifted from the rest-wavelength) one moving towards the observer, a second (red shifted) one produced by receding gas, and a third one, centered at the rest-frame.

In principle, from the velocities of the ejecta and the CSM, one can infer the time of ejection of the CSM which later interacts with the SN ejecta. We adopt the velocities derived from the first spectrum, because it is the closest available to the explosion. We adopt 3400 km s^{-1} for the ejecta (from the FWHM of the broad component), and 560 km s^{-1} for the wind (from the minimum of the narrow P Cygni component). Although the velocity at the explosion should be used for freely expanding ejecta, those of SN 2013gc are likely shocked already soon after the explosion, hence the value

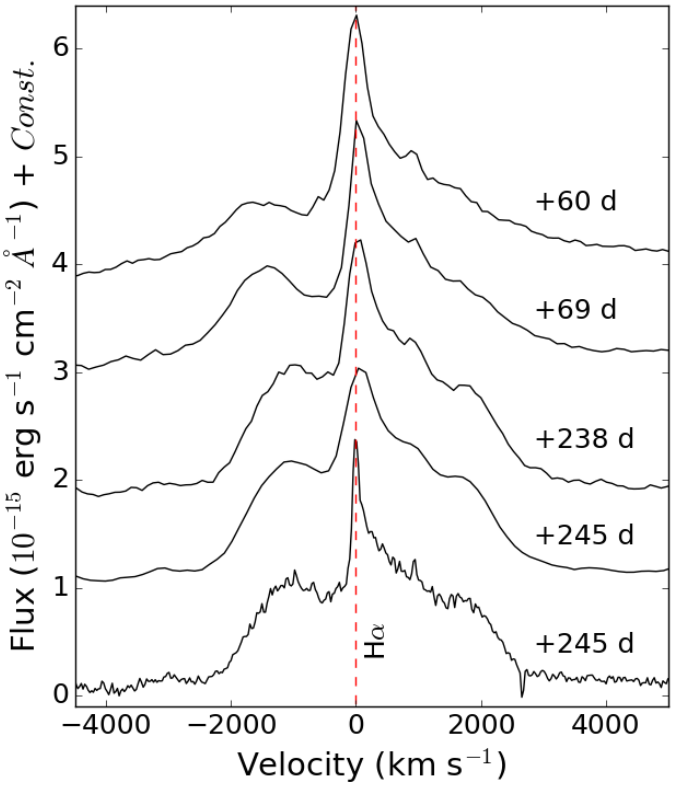

Figure 6.5: Blow up of Hα line in the 5 available spectra. Velocities with respect to the rest frame are reported in abscissa. The zero velocity is marked with a dotted line.

inferred from the first spectrum is a fair approximation of the ejecta velocity. The explosion epoch is unknown, but it is constrained between MJD 56463 (the last non-detection) and MJD 56530 (the first SN detection). Assuming that the collision of the SN ejecta with a dense circumstellar shell marks the onset of the light curve plateau (MJD 56640±10), the material would have been ejected between MJD ∼55560 (December 2010-January 2011) and MJD ∼55970 (February 2012) for the above two constraints on the explosion epoch, respectively. On the other hand, at about MJD 56720±10, we note a major brightening of the light curve, which is an evidence of enhanced CSM-ejecta interaction. With the same velocities and the explosion time interval, the second shell would have been ejected between MJD ∼55150 (November 2009) and MJD ∼55560 (December 2010-January 2011). The above constraints on the mass loss epochs are consistent with the timing of the pre-SN detections, and favour an explosion occurring soon after the

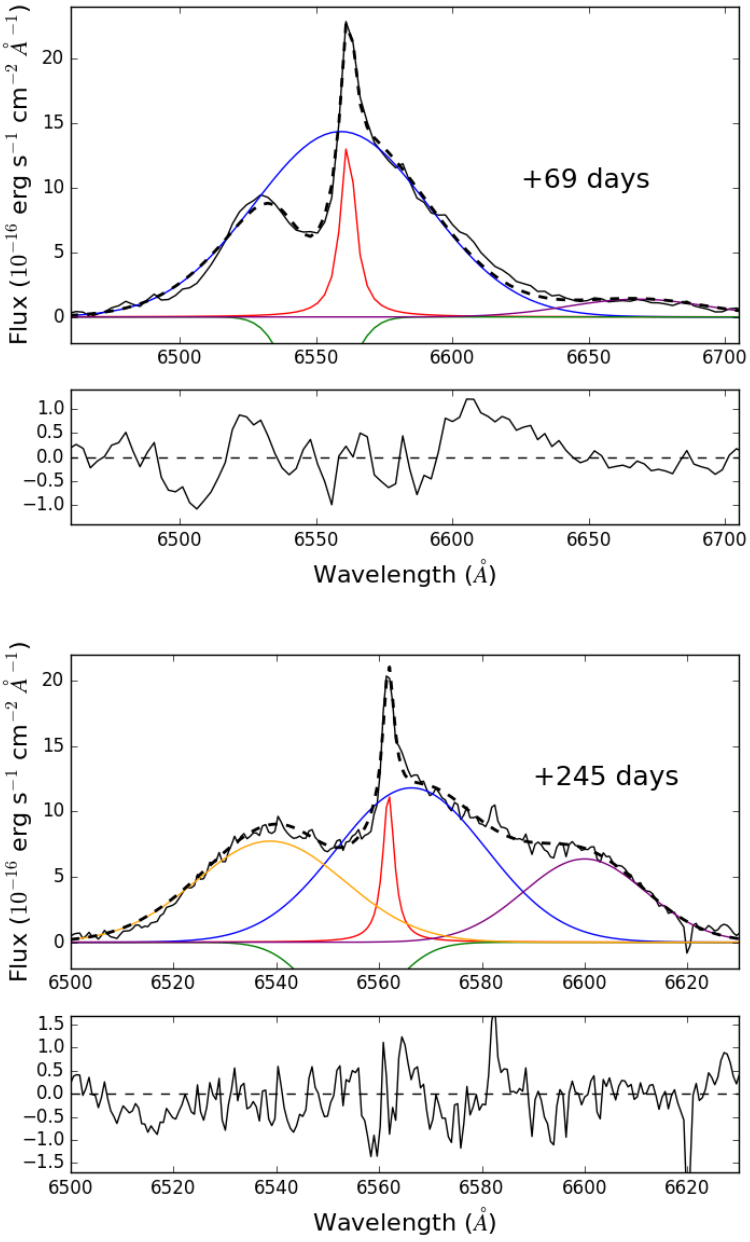

Figure 6.6: Decomposition of the Hα profile through multiple components. Top: In the +69 days spectrum the profile is well fitted using a broad Gaussian emission (blue), on top of which a narrow Lorentzian emission (red) stands, and a Gaussian absorption (green) is necessary to model the P Cygni profile. The bump due to the He I λ6678 is also fitted with a Gaussian emission (purple). Bottom: In the medium-resolution (FWHM=1.7 Å) +245 days spectrum, the Hα profile consists of an intermediate-width Gaussian emission (blue), a narrow Lorentzian emission (red) and a Gaussian absorption for the P Cygni (green). Two additional Gaussian components are required, red-shifted (purple) and blue-shifted (orange). In both graphs, the sum of the 4 components is shown with a black dashed line. Residuals between the data and the fit are reported on the bottom panles.

Table 6.2: FWHM and central wavelengths of the various components of the Hα profile in all spectra. For the P Cygni component, the velocity of the minimum with respect to the rest-frame is reported.

Phase	$(\mathrm{Em})_{broad}$	$(\mathrm{Em})_{narrow}$	$(\mathrm{Ab})_{PCygni}$	Red Wing	Blue Wing
	v_{FWHM}; λ_c	v_{FWHM}; λ_c	Min. vel.	v_{FWHM}; λ_c	v_{FWHM}; λ_c
(d)	(km s^{-1});(Å)	(km s^{-1});(Å)	(km s^{-1})	(km s^{-1});(Å)	(km s^{-1});(Å)
+60	3400±100; 6559	300±15; 6561.7	560		
+69	3450±100; 6557	340±20; 6561.7	470		
+238	1600±50; 6565	420±20; 6561.2	420	1800±50; 6598	1600±50; 6540
+245	1600±50; 6566	350±20; 6563.5	460	1650±50; 6598	1600±50; 6542
+245	1550±50; 6566	120±5; 6561.8	380	1300±30; 6600	1550±50; 6539

last non-detection (Sect. 5.4 and Fig. 5.1). From March 2010, we directly witnessed the outbursts that produced the SN CSM and determined the type IIn/IId observables.

Chapter 7

Discussion

The composite Balmer line profiles, with the simultaneous presence of broad and narrow components with P Cygni profiles, makes SN 2013gc a member of the IId sub-class of type IIn SNe (Benetti, 2000). This fact is supported by the comparison of the colour and absolute light curves of SN 2013gc with those of known SNe IId which show a similar evolution. In particular, the onset of strong ejecta-CSM interaction in SN 2013gc (between 120 and 140 days after the explosion), is compatible with that observed in similar SNe (typically between 100 and 150 days, Benetti, 2000).

7.1 Bolometric luminosity and the ^{56}Ni mass

We calculated the pseudo-bolometric light curve of SN 2013gc accounting for the contribution in the $BVRI$ bands only. For epochs without observations in some bands, we made an interpolation to the available data using the R-band light curve as reference, and assuming a constant colour index. The maximum is not covered by R-band images, hence to constrain the peak luminosity, we calculated the pseudo-bolometric light curve in the $gVIz$ bands. We assumed the $V-I$ and $V-z$ colours to be constant between 30 and 80 days after the explosion, at 1.5 and 2.0 mag, respectively, as derived from the closest photometry of 2013 November 7. Instead, we assumed that the $g-V$ colour has increased from 0.2 to 0.6 mag during this period. We fixed the explosion date on MJD 56520±7, about 10 days before the first SN detection. This implies a rise-time of 23±7 days from the explosion to the maximum.

Then, a first steep decline is observed. In order to estimate an upper limit to the ejected ^{56}Ni mass, we focus on a light curve portion having a decline slope similar to that of ^{56}Co. We identify a very short time interval during which the decline slope is compatible with the ^{56}Co decay rate, i.e. between 97 and 118 days after explosion.

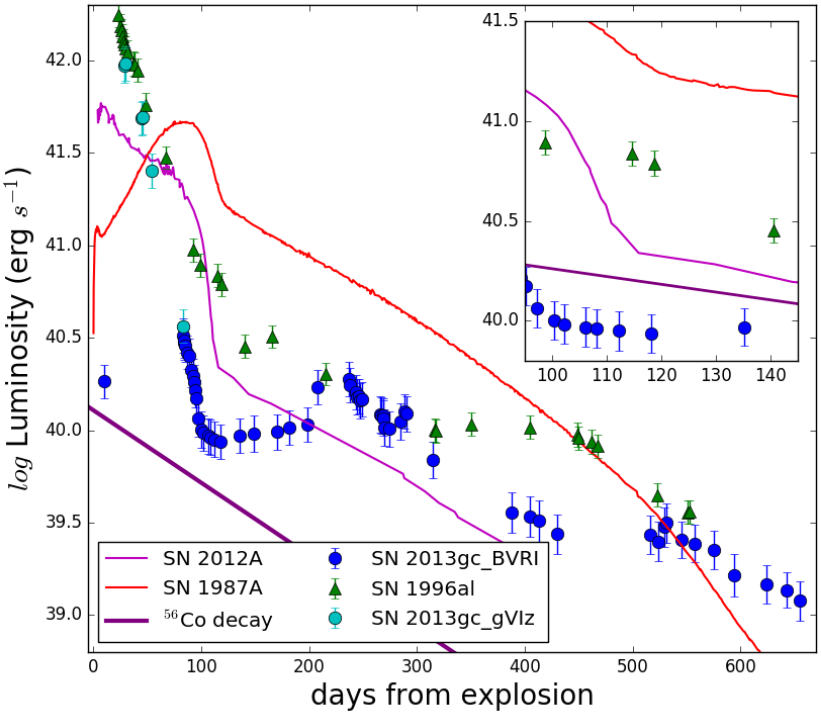

Figure 7.1: Quasi-bolometric ($BVRI$) light curves of SNe 1987A, 1996al, 2012A and 2013gc. The inset shows a blow-up of the region between 95 and 145 days after the explosion, in which there is evidence of ^{56}Co radioactive decay. The decay slope of ^{56}Co (0.98 mag (100 d)$^{-1}$) is reported with a purple line for comparison. The early phase ($gVIz$) bolometric light curve is plotted with cyan dots.

As a comparison, we selected the classical core-collapse SN 1987A, and a type II SN with a shorter plateau, SN 2012A (Tomasella et al., 2013). The choice of SN 2012A was motivated by the fact that the putative ^{56}Co decay occurred started early in SN 2013gc, at ∼100 d, while typical type IIp SNe are still in the plateau phase, or during the steep post-plateau decline. In contrast, SN 2012A was a short-duration IIp, which was already following the ^{56}Co decay at 100 d. Hence, this is a better comparison object to estimate the ^{56}Ni mass of SN 2013gc. SN 1996al is also considered as a comparison object. The bolometric light curves of the four objects are compared in Fig. 7.1, with a blow-up on the portion of the SN 2013gc light curve with a decline rate barely consistent with the ^{56}Co decay.

The estimated ^{56}Ni mass of SN 1987A is 0.085 $M_{\odot}$ (Utrobin & Chugai, 2011), while for SN 2012A the estimate is 0.011±0.004 $M_{\odot}$ (Tomasella et

al., 2013). We calculated and averaged the bolometric luminosity ratio of SN 2012A and SN 2013gc at three epochs after the explosion, at +112, +118 and +135 days. These three epochs were selected because at the same phases SN 2012A was declining with a rate consistent with the ^{56}Co decay. The M_{Ni}^{56} is obtained from the following relation:

$$\frac{L_{bol}(2012A)}{L_{bol}(2013gc)} = \frac{M_{Ni}^{56}(2012A)}{M_{Ni}^{56}(2013gc)} = 2.5 \pm 0.6 \tag{7.1}$$

From this value, and propagating the errors, the ^{56}Ni mass estimated for SN 2013gc is $5.0(\pm 2.7) \times 10^{-3} M_{\odot}$. We remark that this inferred value has large uncertainties, because at 135 d the ejecta-CSM interaction becomes stronger, and the light curve becomes flatter than the ^{56}Co decay. For this reason, the above value of the ^{56}Ni mass should be regarded as an upper limit. On the other hand, we cannot rule out that an optically thick shell is hiding interior emission, leading us to underestimate the ^{56}Ni mass. It is worth noting that for SN 1996al Benetti et al. (2016) constrained an upper ^{56}Ni mass limit of 0.018 $M_{\odot}$, a factor of about 4 higher than that inferred for SN 2013gc.

This ^{56}Ni mass constrained for SN 2013gc is definitely modest, also accounting that other photometric indicators (in particular, the plateau and the second brightening) suggest that the main luminosity powering mechanism is the interaction between the SN ejecta and surrounding material, acting at all phases. For this reason, the ^{56}Ni mass ejected by SN 2013gc is most likely very low, comparable with that inferred for some under-luminous type II SNe (Pastorello et al., 2004; Spiro et al., 2014).

7.2 The progenitor star

The interest for SN 2013gc lies in the fact that a prolonged variability phase was observed in the progenitor site before the SN explosion. So far, only one possible eruptive event was claimed for the progenitor of a SN IId. It was a single detection of a luminous source at the position of SN 1996al in archival Hα images obtained 8 years before the SN explosion (Benetti et al., 2016). For SN 2013gc, the indications of pre-SN stellar activity are much more robust, as we witnessed a complex, long-lasting eruptive phase prior to the explosion. As seen in Sect. 5.4, the variability of the progenitor in 2010-2012 resembles those observed in other SN impostors. In particular, the pre-SN stages of SN 2009ip (Pastorello et al., 2013; Mauerhan et al., 2013a) and SNhunt 151 (Thöne et al., 2017; Elias-Rosa et al., 2018), and the current evolution of SN 2000ch (Pastorello et al., 2010). The bright absolute magnitude of the source in pre-SN images ($M \sim -11$ mag) rules out the possibility that the progenitor was in a quiescent phase.

The deconvolution of the Hα profile, in particular from the last spectrum, allows us to reconstruct the structure of the CSM and to constrain the physics of the explosion, and the nature of progenitor star.

The fast initial (50-80 d) drop of the light curve implies small ejected H mass. A modest ejected mass is consistent with two SN scenarios: the low-energy explosion of a relatively low mass progenitor (7-8 $M_{\odot}$) or, alternatively, a very massive progenitor ($M_{ZAMS} > 25\ M_{\odot}$) ending its existence as a fall-back SN. Assuming a low-mass progenitor scenario, the pre-SN eruptive phase can be attributed to binary interaction or, alternatively, to a super-AGB phase during which a star loses mass generating a circumstellar cocoon, before exploding as an electron-capture SN (e.g., Nomoto, 1984; Kitaura et al., 2006; Pumo et al., 2009). In the massive progenitor scenario, the star core collapses into a BH, as most of the stellar mantle falls back onto it. In this way, only the most external layers are ejected. A fall-back SN is also consistent with the low ejected ^{56}Ni mass (Zampieri et al., 1998; Moriya et al., 2010), because the inner regions of the star rich in heavy elements remain bound to the collapsed core. A fall-back SN produces a faint explosion. The absence of [O I] $\lambda\lambda$ 6300,6364 lines in the late spectra is also in agreement with the expectations of the fall-back SN scenario (Valenti et al., 2009), but can be alternatively explained as due to an optically thick region of ejecta-CSM interaction that obscures the O-rich ejecta.

High mass stars, such as LBVs and WR stars, are known to experience severe mass loss via super-winds during the final stages of their life. When they finally produce a core-collapse SN, the material ejected by the SN will interact with the composite circumstellar environment. LBVs are suitable progenitor candidates for types IIn/IId SNe. Such LBV candidates would pass through an eruptive phase with many alleged outbursts, that create a complex and structured CSM. The interaction of the SN ejecta with this CSM would produce unusual features in the light curve, like the plateau and the observed rebrightening.

A third, somewhat different scenario, is a non-terminal explosion event. The precursor activity exhibited by SN 2013gc shares some similarities with the pre-explosion variability of SN 2009ip. The nature of this object and its fate after the two 2012 events, are still somewhat disputed, and a non-terminal mechanism has also been proposed (Pastorello et al., 2013; Margutti et al., 2014). This scenario would be consistent with many characteristics of SN 2013gc, including no ^{56}Ni production, the lack of [O I] lines and the faint absolute magnitude. Indeed, the source detected in the 2017 DECAPS images might be what remains of the survived progenitor. In this framework, the brightest event was a SN impostor (like the objects described in Chapt. 2), that generated a fast moving shell. The following photometric evolution was dictated by the shell-shell collision.

We propose two physical mechanism that possibly driven the precursor variability. Pulsational mass-loss in very massive stars can be accompanied

by large luminosity variations. Another plausible scenario is a LBV binary system in eccentric orbits. When the secondary approaches the periastron, the tidal forces can strip away part of the material of the primary, enhancing the mass losses and the luminosity (Pastorello et al., 2010). A similar framework has been proposed for η Car (Sect. 1.3). If this is the case, a modulation would be observable in the light curve. The observations do not strongly support either scenarios, because of the lack of the adeguate accuracy and cadence.

7.3 The explosion scenario

From the decomposition of the Hα profile, we can constrain the geometry of the CSM. The presence of multi-component Hα line profiles both at early and late-epoch spectra reveals that the CSM-ejecta interaction is likely active from the early phases of the SN evolution, suggesting that progenitor's mass loss has continued until a very short time before the SN explosion. In this context, the above claim is supported by the evidence that the progenitor in outburst was observed until May 2013, only $\sim$100 days before the SN explosion. The light curve plateau and the rebrightening at about 200 days have to be considered as enhanced interaction with a denser CSM regions.

The Hα profile in the late spectra has a composite profile, with three intermediate-width components (with v_{FWHM} exceeding 10^3 km s^{-1}): a blue-shifted component peaking at -1000 km s^{-1}, a redshifted one centered at $+1600$ km s^{-1}, and a third one in the middle, centered at the rest wavelength of the transition, atop of which a narrow emission is observed with v_{FWHM} of a few 10^2 km s^{-1}. This suggests a complex and structured CSM geometry.

The two components shifted from the rest wavelength reveal a bipolar emitting structure of the CSM, expanding with a core velocity in the range 1300-1800 km s^{-1}. The difference of the measured expansion velocities can be explained with an intrinsic difference in the ejection velocity of the two lobes, or possibly by a mismatch between the line of sight and the polar axis of the bipolar nebula. Similar spectral features were observed in the SN IIn 2010jp, although in that case a jet-like explosion in a nearly spherically symmetric CSM was proposed (Smith et al., 2012), and the velocities involved were in fact one order of magnitude larger. The kinetic energy of SN 2013gc is much smaller, and is consistent with a fall-back SN scenario (see Sect. 7.2). A spherically symmetric CSM expanding at much lower velocity is revealed through the presence of a narrow Hα component, while a nearly spherical shell, shocked by the interaction, produces the central, intermediate-width component. The material shocked by the ejecta is optically thick, and hides (at all epochs) the underlying SN features. A sketch of the proposed CSM structure is illustrated in Fig. 7.2, adapted from Smith

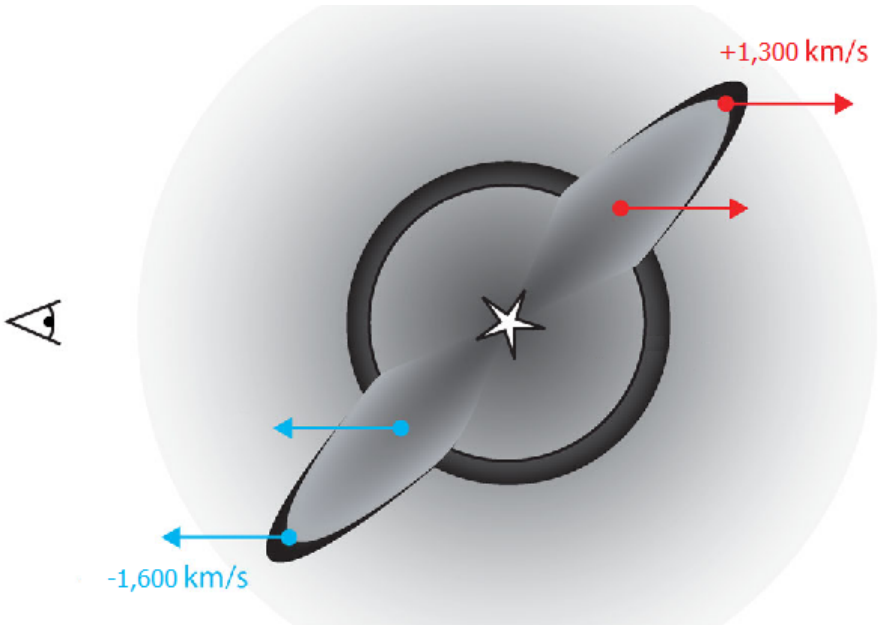

Figure 7.2: A sketch of the probable CSM structure around SN 2013gc. The original model was elaborated for the type IIn SN 2010jp. An inclined, bipolar structure is surrounded by a shocked shell and a spherical CSM. The velocities reported are the observed radial motions of the blue-shifted and red-shifted components in the last spectrum. An adaptation from Fig. 9 of Smith et al. (2012).

et al. (2012). This structure was originally proposed for SN 2010jp.

This CSM configuration shares some similarity with that proposed by Benetti et al. (2016) for SN 1996al, consisting of an equatorial circumstellar disc producing the Hα profile with two emission bumps shifted from the rest wavelength. That material was surrounded by a spherical, clumpy component producing the Hα emission at zero velocity. The clumpiness of the SN 1996al CSM was deduced from the evolution of the He lines, that became more prominent with time. In analogy with SN 1996al, the spectra of SN 2013gc show an increasing strength of the He lines from the early to the late phases, which may indicate the presence of higher-density clumps heated by the SN shock in its lower-density, spherically symmetric CSM component. We also note that the radial velocities of the Hα bumps of SN 1996al and SN 2013gc are comparable, supporting an overall similarity in the gas ejection scenarios for the two objects. SN 1996al was characterized by low ejecta mass and a modest kinetic energy. The ejecta interaction with a dense CSM embedding the progenitor determined the light curve features at all phases, and was still active 15 years after the explosion. The proposed CSM structure around SN 2013gc is composed by an equatorial disc with a complex

density profile, and ejecta-CSM interaction being always present. When the ejecta reach the first CSM equatorial density enhancement, the conversion of kinetic energy into radiation gives rise to the observed plateau, while the encounter with an outer layer with higher density powers the second peak. Later on, ejecta-CSM interactions weakens and the SN light curve finally starts the fast decline.

Chapter 8

Conclusions

In this work we analysed the photometric evolution and the spectra of SN 2013gc, and compared our data with a sample of objects that share some observational similarity. We conlcude that SN 2013gc is a member of the type IId SN class, a subgroup of type IIn SNe whose spectra are characterized by double, broad and narrow, P Cygni Hα components. This family includes also SN 2000P, whose data are shown here for the first time. The light curve of SN 2013gc experiences a first peak followed initially by a fast decline, and later a slower decline rate which is consistent with that of the ^{56}Co. This short-lasting phase is followed by a sort of plateau. Later on, a sudden rebrightening is observed, a sign of enhanced CSM/ejecta interaction, and finally the SN luminosity fades. The comparison of the absolute light curves reveals that SN 2013gc is fainter than the other SNe IId. The intrinsic faintness is in agreement with a fall-back SN scenario, but can be also due to an underestimated dust contribution.

SN 2013gc can be considered a scaled-down version of SN 1996al, triggered by the same physical process: a fall-back SN from a highly massive star. SN 2013gc is the first object of this sub-group showing a long-duration progenitor's eruptive phase lasting a few years (at least, from 2010 and 2013), and continued until a very short time before the SN explosion. The object showed significant variability, with oscillations of 1-2 mag in very short timescales (days to months). The multiple flares and the long-duration major eruption are best suited with a massive progenitor in its final evolutionary stages, very likely an LBV. We deconvolved the Hα complex profile with multiple Gaussian components, to estimate the velocities of the ejecta and the circumstellar wind. The explosion epoch is constrained to be between the last non-detection and the first SN detection, and we assume the begin of the plateau and the subsequent rebrightening to mark the onset of the strong interaction episode, started when the fast ejecta reached the pre-existing CSM material. We calculated the ejection time of the shell with a

simple linear model, taking the velocities of the ejecta and the CSM from the FWHM of the broad component and the wavelength of narrow blue-shifted P Cygni absorption, respectively. We constrained the explosion epoch to be between the last non-detection and the first SN detection, and assumed the onsets of the plateau and the rebrightening as the on-set of a stronger interaction phase. The found dates are consistent with the epoch of the observed eruptive phase. The pre-SN activity observed some years before, if spotted while occurring, should be considered an impostor, very likely an LBV-like eruption, that heralded the SN explosion.

The outbursts formed a structured CSM around the progenitor (and very close to it), and the SN ejecta interact with it from soon after the SN explosion. When the ejecta collide with denser CSM layers, the interaction powered the observed light curve plateau and the second peak. The CSM is likely clumpy, as deduced from the evolution of the He lines, and is composed of a spherically symmetric component, two denser shells and a further bipolar CSM component. The fall-back scenario of a massive star is supported by the low ^{56}Ni mass found from the bolometric light curve, the low luminosity of the SN, the lack of [O I] lines in the spectra and the detection of numerous pre-SN outbursts from the progenitor. However, the pre-SN variability, the modest ^{56}Ni mass ejected and a detection 3.5 years after the explosion can also be explained by a non-terminal explosion. The discovery of similar SNe with signs of pre-SN activity, the subsequent detailed follow-up campaigns and, finally, the deep imaging of the region years after the putative SN explosion may help in predicting the final fate of massive stars. The future generation of survey telescopes, the LSST in primis, will play a major role in achieving those goals.

Appendix

In this appendix, we report the tables containing all the Optical Johnson-Cousins, Sloan, NIR and clear filter photometry magnitudes obtained for SN 2013gc. The time coverage spans about 7 years.

Table 8.1: Optical Johnson-Cousins and Sloan photometry of 2013gc.

Date	MJD	B	V	R	I	g	z	y	Telescope[a]
2010-03-02	55257.32							19.57(0.37)	PS1
2010-04-04	55290.24						20.32(0.15)		PS1
2010-11-02	55517.61						>20.11		PS1
2010-11-17	55517.61							>18.90	PS1
2010-12-24	55554±22			21.78(0.40)					PTF
2011-01-18	55579±1			>20.42					PTF
2011-01-24	55585±3			>18.96					PTF
2011-03-25	55645.24							19.47(0.30)	PS1
2011-10-20	55854.65							19.06(0.16)	PS1
2011-11-14	55879.60						21.06(0.29)		PS1
2012-02-10	55967.37				19.76(0.08)[d]				PS1
2012-04-04	56021.24							>19.72	PS1
2012-10-29	56229.63						20.64(0.31)		PS1
2012-10-30	56230.65							>19.62	PS1
2012-11-14[e]	56245.36			20.89(0.16)[b]	20.99(0.25)[b]				VST
2012-12-28	56289.54				20.19(0.18)[d]				PS1
2013-03-11	56362.28		>18.83						NTT
2013-03-19	56370.16		>19.39						NTT
2013-03-29	56380.98	>18.55	>18.65	>18.44	>18.31				PROMPT
2013-04-01	56383.18	>18.37							PROMPT
2013-04-01	56383.98	>19.21	>18.56	>18.64	>18.13				PROMPT
2013-04-02	56384.14		>20.33						NTT
2013-04-02	56384.98	>18.30	>18.52	>18.13	>17.91				PROMPT
2013-04-04	56386.97	>19.00	>18.76	>18.52	>18.26				PROMPT
2013-04-05	56387.98	>19.95	>18.82		>17.91				PROMPT
2013-04-06	56388.08		>20.58						NTT
2013-04-07	56389.01	>20.01	>19.61						PROMPT
2013-04-08	56390.00	>20.22	>18.84	>19.22	>18.09				PROMPT
2013-04-08	56390.97		>17.58	>17.79	>17.66				PROMPT
2013-04-10	56392.98	>19.71	>18.85	>18.82	>18.26				PROMPT
2013-04-11	56393.97	>18.33							PROMPT
2013-04-12	56394.98	>20.28							PROMPT
2013-04-13	56395.05		>20.35						NTT
2013-04-14	56396.03			>21.85[f]		>22.37			VST
2013-04-14	56396.04	>18.87	>18.97	>19.28	>18.34				PROMPT
2013-04-14	56396.96	>18.81	>18.00	>18.27					PROMPT
2013-04-16	56398.96	>19.25	>19.56	>19.35	>18.78				PROMPT
2013-04-19	56401.02		>20.29						NTT
2013-04-19	56401.98	>20.99	>20.52	>20.24	>19.72				PROMPT
2013-04-20	56402.96	>20.42	>20.59	>20.58	>19.98				PROMPT
2013-04-22	56404.05	>20.87	>19.09	>19.15	>18.60				PROMPT
2013-04-25	56407.98	>19.42	>19.33	>19.67	>19.25				PROMPT
2013-04-28	56410.08		>17.64						PROMPT
2013-04-28	56410.96		>17.99	>18.34					PROMPT
2013-04-29	56411.96		>18.70						PROMPT
2013-05-01	56413.95	>19.30							PROMPT
2013-05-04	56416.06	>19.64	>18.20						PROMPT
2013-05-04	56416.96			20.45(0.14)					GEMINI
2013-05-05	56417.99	>20.74	>18.84						PROMPT
2013-05-07	56419.01	>20.48	>19.16	>19.07					PROMPT
2013-05-11	56423.96	>20.66	>21.07	>20.43	>20.29				PROMPT
2013-05-15	56427.96	>19.80	>19.99						PROMPT
2013-05-19	56431.96	>19.99	>20.23	>18.71					PROMPT
2013-05-20	56432.97			>20.13	>19.67				PROMPT
2013-05-22	56434.97	>20.90							PROMPT
2013-05-23	56435.96	>19.44	>20.99						PROMPT
2013-05-24	56436.96			>20.12	>19.30				PROMPT
2013-05-29	56441.96	>18.96	>20.13	>20.75	>19.17				PROMPT
2013-06-03	56446.94		>18.15						PROMPT
2013-06-12	56455.95		>19.06	>19.79					PROMPT
2013-06-19	56462.94	>18.23	>18.66						PROMPT
2013-08-26	56530.39			18.21(0.08)					SOAR
2013-09-12	56547.36		15.16(0.02)						NTT
2013-09-13	56548.36		15.14(0.04)						NTT
2013-09-28	56563.38					15.95(0.05)			PROMPT
2013-09-29	56564.40				14.66(0.14)[b]	15.91(0.06)			PROMPT
2013-10-08	56573.29		16.59(0.05)						NTT
2013-11-04	56600.65						16.71(0.02)	16.60(0.03)	PS1
2013-11-06	56602.28	19.93(0.04)	18.75(0.08)						SARA
2013-11-08	56604.30			17.67(0.11)[b]	17.18(0.08)[b]	19.54(0.08)	16.83(0.06)		PROMPT
2013-11-12	56608.31			17.84(0.07)	17.41(0.10)				TRAP
2013-11-16	56612.26			18.29(0.05)	17.53(0.10)				SARA
2013-11-18	56614.25			18.40(0.06)					SOAR
2013-11-26	56622.28	20.86(0.37)	20.04(0.13)						SARA
2013-12-29	56655.17			19.01(0.06)	18.41(0.11)				SARA

Date	MJD	B	V	R	I	g	z	y	Telescope[a]
2014-01-02	56659.22	21.26(0.12)	20.30(0.04)						TRAP
2014-01-12	56669.19			19.02(0.24)	18.44(0.21)				TRAP
2014-02-02	56690.17			18.96(0.22)	18.49(0.12)				TRAP
2014-02-13	56701.15		20.22(0.19)	18.85(0.05)					TRAP
2014-03-02	56718.11			18.83(0.07)	18.52(0.07)				TRAP
2014-03-22	56738.05				17.38(0.04)				TRAP
2014-04-02	56749.00		19.91(0.09)						TRAP
2014-05-04	56781.24							18.35(0.07)	PS1
2014-05-05	56782.09		19.79(0.11)						PONT
2014-05-08	56785.97	20.59(0.32)	20.18(0.27)	18.64(0.13)	18.41(0.09)				SARA
2014-05-09	56786.99			18.66(0.15)[b]	18.43(0.30)[b]	20.59(0.33)	17.72(0.30)		PROMPT
2014-05-11	56788.98	>20.52	20.09(0.14)	18.68(0.14)	18.38(0.09)				TRAP
2014-05-11	56788.99			18.77(0.06)					SOAR
2014-05-16	56793.98	20.82(0.27)	20.13(0.14)			20.58(0.23)			SARA
2014-05-27	56804.96	20.54(0.33)	19.93(0.20)	19.04(0.13)	18.52(0.10)				SARA
2014-05-30	56807.98	20.91(0.16)	19.83(0.10)	18.56(0.08)					SMARTS
2014-06-01	56809.97	20.88(0.18)	20.01(0.13)	18.67(0.11)	18.18(0.20)				TRAP
2014-06-10	56818.97	>20.93							TRAP
2014-06-26	56834.97			19.28(0.19)	18.84(0.23)				SARA
2015-02-22	57075.05	>21.01	>21.00		>19.46				TRAP
2015-04-02	57114.02	>21.21	>20.94	20.84(0.46)	>20.34				TRAP
2015-05-01	57143.99	>20.45	>20.54	20.95(0.32)	>19.93				TRAP
2015-05-12	57154.00	>21.26							TRAP
2015-05-20	57163.00			21.04(0.18)	>20.13				TRAP
2015-06-01	57174.99	>20.37	>20.26	21.18(0.37)	>20.12				TRAP
2015-06-11	57185.00	>20.78							TRAP
2017-03-04[c]	57816±47					23.57(0.22)	22.62(0.24)		DEC

[a] NTT = ESO 3.6-meter NTT+EFOSC2, SOAR = 4.1-meter 'SOAR'+Goodman Spectrograph, TRAP = 0.5-meter TRAPPIST, SMARTS = CTIO 1.3-meter+ANDICAM, SARA = CTIO 0.6-meter+ARC, GEMINI = 8.1-meter Gemini South+GMOS-S, PTF = 1.2-meter 'S. Oschin' Schmidt+PTF survey, PONT = Las Campanas 2.5-meter 'Du Pont'+WFCCD/WF4K-1, PS1 = Haleakala 1.8-meter+Pan-STARRS1 Survey, DEC = CTIO 4-meter 'V. Blanco'+Dark Energy Camera (DECaPS survey), VST = ESO 2.6-meter VST+OMEGACAM.
[b] Converted from Sloan to Johnson photometric system.
[c] For this epoch we also report $r = 22.63(0.18)$.
[d] PS1 i band magnitude, not converted to I.
[e] For this epoch and this instrument we also report $u > 21.40$.
[f] VST r band magnitude, not converted to R.

Table 8.2: NIR photometry of 2013gc.

Date	MJD	J	H	K	Telescope[a]
2013-03-18	56370.00	>19.70	>18.02	>18.32	SOFI
2013-04-04	56386.02	19.29(0.33)	18.84(0.32)	18.08(0.19)	SOFI
2013-04-12	56394.05	19.39(0.26)	18.74(0.40)	17.91(0.25)	SOFI
2013-04-18	56400.05	19.46(0.27)	18.81(0.33)	18.54(0.37)	SOFI
2014-05-30	56807.98	17.29(0.16)	17.15(0.18)	17.55(0.30)	SMARTS

[a] SOFI = ESO 3.6-meter NTT+SOFI, SMARTS = CTIO 1.3-meter+ANDICAM.

Table 8.3: Clear photometry of 2013gc, treated as Johnson-Cousins R. All measurements are obtained with the PROMPT telescopes.

Date	MJD	clear
2011-01-27	55588.07	>18.99
2011-02-01	55593.08	>19.32
2011-02-20	55612.10	>19.72
2011-03-06	55626.06	19.70(0.15)
2011-03-12	55632.03	>19.68
2011-05-02	55683.08	>19.57
2011-09-14	55818.37	>19.01
2011-09-25	55829.34	>19.57
2011-10-17	55851.28	>19.08
2011-10-22	55856.35	>18.49
2011-11-02	55867.24	>19.47
2012-01-04	55930.10	>19.16
2012-01-07	55933.19	20.36(0.36)
2012-01-10	55936.20	>19.27
2012-01-14	55940.21	20.42(0.27)
2012-01-18	55944.18	>20.01
2012-01-24	55950.15	>19.95
2012-01-27	55953.15	20.46(0.41)
2012-01-29	55955.13	>19.72
2012-02-01	55958.20	20.93(0.41)
2012-02-03	55960.16	>19.48
2012-02-06	55963.12	>19.57
2012-02-08	55965.14	19.89(0.45)
2012-02-10	55967.11	19.93(0.37)
2012-02-12	55969.10	20.35(0.34)
2012-02-21	55978.10	>20.16
2012-02-24	55981.07	>19.39
2012-02-25	55982.09	21.09(0.50)
2012-02-26	55983.08	20.00(0.20)
2012-02-27	55984.09	20.65(0.26)
2012-03-02	55988.09	>19.64
2012-03-05	55991.07	>19.90
2012-03-07	55993.05	>19.19
2012-03-09	55995.07	19.96(0.37)
2012-03-11	55997.06	>19.26
2012-03-13	55999.05	>19.95
2012-03-14	56000.06	>18.70
2012-03-16	56002.05	21.27(0.46)
2012-03-18	56004.04	>20.14
2012-03-26	56012.03	>20.12
2012-03-31	56017.01	20.29(0.47)
2012-04-06	56023.01	>19.63
2012-10-11	56211.30	>19.67
2012-10-14	56214.29	>19.71
2012-11-27	56258.22	>19.72
2012-12-01	56262.25	19.93(0.32)
2012-12-04	56265.30	>19.43
2012-12-06	56267.29	>19.75
2012-12-09	56270.15	>19.09
2012-12-13	56274.20	>19.86
2012-12-16	56277.12	>19.80
2012-12-21	56282.12	20.47(0.42)
2012-12-24	56285.16	20.41(0.39)
2012-12-27	56288.23	20.10(0.44)
2012-12-31	56292.22	>19.69
2013-01-04	56296.21	>19.48
2013-01-13	56305.22	>19.62
2013-01-16	56308.12	>19.69
2013-01-23	56315.35	>19.36
2013-01-26	56318.14	>19.37
2013-02-02	56325.21	>19.56
2013-02-08	56331.30	>19.62
2013-02-15	56338.15	>20.02
2013-03-09	56360.23	>19.79
2013-03-10	56361.12	>19.50
2013-03-11	56362.14	>19.01
2013-03-17	56368.08	>19.71
2013-03-19	56370.22	>19.52
2013-03-23	56374.18	>19.21
2013-03-26	56377.18	>19.25
2013-03-28	56379.12	>19.58
2013-04-04	56386.07	>19.51
2013-04-21	56403.03	>19.69
2013-11-07	56603.33	17.59(0.08)
2013-11-08	56604.25	17.78(0.07)
2013-11-09	56605.23	17.77(0.08)
2013-11-11	56607.22	17.83(0.06)
2013-11-14	56610.21	18.15(0.14)
2013-11-17	56613.27	18.31(0.15)
2013-11-19	56615.24	18.52(0.13)
2013-11-21	56617.19	19.06(0.15)
2013-11-24	56620.31	19.10(0.18)
2013-11-26	56622.28	19.08(0.13)
2013-11-30	56626.20	19.14(0.18)
2013-12-02	56628.16	19.16(0.17)
2013-12-06	56632.15	19.19(0.20)
2013-12-12	56638.14	19.29(0.13)
2014-03-12	56728.21	18.21(0.11)
2014-04-10	56757.09	18.13(0.07)
2014-04-11	56758.14	18.34(0.10)
2014-04-16	56763.08	18.50(0.19)
2014-04-17	56764.08	18.70(0.15)
2014-04-19	56766.06	18.61(0.08)
2014-04-20	56767.09	18.77(0.11)
2014-04-22	56769.07	18.64(0.06)
2014-05-13	56790.05	19.14(0.17)
2014-05-16	56793.00	19.07(0.10)
2014-09-07	56907.40	19.99(0.38)
2014-09-24	56924.36	20.05(0.37)
2014-10-03	56933.37	20.11(0.41)
2014-10-09	56939.31	>18.21
2014-10-11	56941.30	>18.47
2014-10-20	56950.28	20.28(0.33)
2014-11-08	56969.22	>18.99
2014-11-13	56974.32	>19.80
2015-01-03	57025.20	>19.54
2015-01-07	57029.19	>19.41
2015-01-10	57032.34	>19.98
2015-01-12	57034.26	>19.98
2015-01-14	57036.31	20.30(0.32)
2015-01-16	57038.29	>20.02
2015-01-21	57043.34	20.38(0.37)
2015-01-22	57044.26	>19.18
2015-01-26	57048.32	>19.79
2015-01-27	57049.26	20.19(0.36)
2015-01-29	57051.28	20.13(0.36)
2015-02-01	57054.26	>19.62
2015-02-03	57056.33	>18.71
2015-02-04	57057.27	>18.60
2015-02-07	57060.15	>19.58
2015-02-08	57061.30	>19.00
2015-02-10	57063.10	>19.64
2015-02-12	57065.22	20.36(0.25)
2015-02-17	57070.30	>19.75
2015-02-18	57071.30	>19.83
2015-02-22	57075.09	>19.78
2015-02-24	57077.09	20.41(0.30)
2015-02-26	57079.27	>18.96
2015-03-06	57087.08	>19.07
2015-03-12	57093.14	>19.71
2015-03-14	57095.18	20.49(0.33)
2015-03-18	57099.22	>19.08
2015-03-28	57109.19	>19.06
2015-03-30	57111.17	>19.02
2015-04-04	57116.04	>19.15
2015-04-11	57123.12	>19.14

Ringraziamenti

Voglio ringraziare A. Pastorello per avermi seguito in questi 9 mesi di lavoro, per il suo tempo speso (anzi, perso...) con me, per tutti i caffè mattutini offerti e per avermi corretto le innumerevoli bozze dell'articolo prima, e della tesi poi. Ringrazio i membri del gruppo Supernove (i 'Supernovari') dell'Osservatorio Astronomico di Padova, Stefano Benetti, Enrico Cappellaro, Massimo Turatto, per i contributi e i suggerimenti elargiti nel lavoro e nella stesura di questa tesi e dell'articolo relativo. Grazie anche al gruppo AGN ('AGNisti'?) del Dipartimento di Astronomia dell'Università di Padova, Enrico Congiu e Marco Berton, in procinto di lasciare l'Italia, e S. Ciroi. Un complimenti a Paolo Ochner, per l'ottimo lavoro di divulgazione e ricerca che svolge, quasi in solitaria, all'Osservatorio di Asiago. Sempre tra i padovani, ma al di fuori dell'ambito scientifico, grazie alla Banda di Selvazzano, per le piacevoli serate passate insieme a suonare. Per i ringraziamenti alle persone coinvolte e alla strumentazione utilizzata in questa ricerca si rimanda alla relativa sezione in Reguitti et al. (2018).

Bibliography

Adams, S.M.; Kochanek, C.S.; Prieto, J.L. et al., 2016, MNRAS, 460, 1645

Agnoletto, I.; Benetti, S.; Cappellaro, E. et al., 2009, ApJ, 691, 1348

Antezana, R.; Hamuy, M.; Pignata, G. et al., 2013, CBET 3699

Aretxaga, I.; Benetti, S.; Terlevich, R.J. et al., 1999, MNRAS, 309 ,343

Aydi, E.; Page, K. L.; Kuin, N. P. M. et al., 2018, MNRAS, 474, 2679

Baade, W.; Zwicky, F., 1934, Contributions from Mt Wilson Observatory, 3, 73

Barbon, R.; Ciatti, F.; Rosino, L., 1979, A&A, 72, 287

Barbon, R.; Buondí, V.; Cappellaro, E.; Turatto, M., 1999, A&AS, 139, 531

Benetti, S.; Cappellaro, E.; Danziger, I.J. et al., 1998, MNRAS, 294, 448

Benetti, S.; Turatto, M.; Cappellaro, E. et al., 1999, MNRAS, 305, 811

Benetti, S., 2000, Mem. Soc. Astron. It., 71, 323

Benetti, S.; Chugai, N.N.; Cappellaro, E. et al., 2016, MNRAS, 456, 3296

Berger, E.; Soderberg, A.M.; Foley, R.J. et al., 2009, ApJ, 699, 1850

Blondin, S.; Tonry, J.L., 2007, AIPC, 924, 312

Bond, H.E.; Bedin, L.R.; Bonanos, A.Z. et al., 2009, ApJ, 695, 154

Botticella, M.T.; Pastorello, A.; Smartt, S.J. et al., 2009, MNRAS, 398, 1041

Cai, Y.Z.; Pastorello, A.; Fraser, M. et al., 2018, MNRAS temporary, 1967

Cappellaro, E.; Benetti, S.; Turatto, M. & Pastorello, A., 2000, IAUC, 7380, 2

Cappellaro, E., 2014, SNOoPY: a package for SN photometry, http://sngroup.oapd.inaf.it/snoopy.html

Cardelli, J.A.; Clayton, G.C.; Mathis, J.S., 1989, ApJ, 345, 245

Carrasco, F.; Hamuy, M.; Antezana, R. et al., 2013, CBET 3437

Chambers, K.C.; Magnier, E.A.; Metcalfe, N. et al., 2016, arXiv, 1612.05560

Chatzopoulos, E.; Wheeler, J.C.; Vinko, J.et al., 2011, ApJ, 729, 143

Chevalier, R.A.; Fransson, C., 1994, ApJ, 420, 268

Chonis, T.S. & Gaskell, C.M., 2008, AJ, 135, 264

Chugai, N.N., 1997, ARep, 41, 672

Chugai, N.N.; Danziger, I.J., 1994, MNRAS, 268, 173

Colas, F. & Yamaoka, H., 2000, IAUC, 7378, 1

Crook, Aidan C.; Huchra, John P. et al., 2007, ApJ, 655, 790

Davidson, Kris; Humphreys, Roberta M., 2012, ASSL, 384, D

De Groot, M.; van Genderen, A. M.; Sterken, C., 1996, IrAJ, 1996, 23, 187

De Vaucouleurs, G.; De Vaucouleurs, A. et al., 1991, RC3, 9, C

Dopita, M.A.; Evans, R.; Cohen, M.; Schwartz, R.D., 1984, ApJ, 287, 69

Elias-Rosa, N.; Benetti, S.; Cappellaro, E. et al., 2018, MNRAS, 475, 2614

Fitzpatrick, E.L., 1999, PASP, 111, 63

Foley, R.J.; Berger, E.; Fox, O.; Levesque, E.M. et al., 2011, ApJ, 732, 32

Fraser, M.; Kotak, R.; Smartt, S. J.; Pastorello, A., 2011, ATel 3574

Fraser, M.; Inserra, C.; Jerkstrand, A. et al., 2013, MNRAS, 433, 1312

Fraser, M.; Magee, M.; Kotak, R. et al., 2013, ApJ, 779, 8

Gal-Yam, A.; Leonard, D.C.; Fox, D.B. et al., 2007, ApJ, 656, 372

Gal-Yam, A.; Leonard, D.C., 2009, Nature, 458, 865

Gal-Yam, A., 2012, Science, 337, 927

Gibson, B.K.; Stetson, P.B.; Freedman, W.L. et al., 2000, ApJ, 529 ,723

Gillon, M.; Queloz, D. et al., 2011, EPJWC, 1106002

Graham, M.L.; Sand, D.J.; Valenti, S. et al., 2014, ApJ, 787, 163

Hamuy, M.; Pignata, G.; Maza J. et al., 2012, Mem. Soc. Astr. It., 83, 388

Heger, A.; Fryer, C. L.; Woosley, S.E. et al., 2003, ApJ, 591, 288

Hoffman, J.L.; Nugent, P.; Kasen, D. et al., 2005, ASPC, 343, 277

Hubble, E.; Sandage, A., 1953, ApJ, 118, 353

Humphreys, R.M.; Davidson, K., 1994, PASP, 106, 1025

Humphreys, R.M.; Davidson, K.; Jones, T.J. et al., 2012, ApJ, 760, 93

Kasliwal, M.M.; Kulkarni, S.R.; Arcavi, I. et al., 2011, ApJ, 730, 134

Kankare, E.; Kotak, R.; Mattila, S. et al., 2017, Nature Astronomy, 1, 865

Kashi A., 2010, MNRAS, 405, 1924

Kashi A., Soker, N., 2010, arXiv, 1011.1222

Keel, W.C.; Oswalt, T.; Mack, P. et al., 2017, PASP, 129, 5002

Kitaura, F.S.; Janka, H.T.; Hillebrandt, W.; 2006, A&A, 450, 345

Kochanek, C.S.; Adams, S.M.; Belczynski, K., 2014, MNRAS, 443, 1319

Kulkarni, S.R.; Ofek, E.O.; Rau, A. et al., 2007, Nature, 447, 458

Landolt, Arlo U., 1992, AJ, 104, 340

Li, W.; Filippenko, A.V.; Van Dyk, S.D. et al., 2002, PASP, 114, 403

Magnier, E.A.; Chambers, K.C.; Flewelling, H.A. et al., 2016, arXiv, 1612.05240

Magnier, E.A.; Schlafly, E.F.; Finkbeiner, D.P. et al., 2016, arXiv, 1612.05242

Mason, E.; Diaz, M.; Williams, R. E., 2010, A&A, 516, 108

Margutti, R.; Milisavljevic, D.; Soderberg, A.M. et al., 2014, ApJ, 780, 21

Mauerhan, J.; Smith, N., 2012, MNRAS.424.2659M

Mauerhan, J.C.; Smith, N.; Filippenko, A.V. et al., 2013, MNRAS, 430, 1801

Mauerhan, J.C.; Smith, N.; Silverman, J.M. et al., 2013, MNRAS, 431, 2599

Moriya, T.; Tominaga, N.; Tanaka, M. et al., 2010, ApJ, 719, 1445

Moriya, T.J.; Sorokina, E.I.; Chevalier, R.A., 2018, SSRv, 214, 59

Mould, J.R.; Huchra, J.P.; Freedman, W.L. et al., 2000, ApJ, 529, 786

Munari, U.; Henden, A.; Zwitter, T. et al., 2002, A&A, 389, 51

Nomoto, K., 1984, ApJ, 277, 791

Ofek, E.O.; Sullivan, M.; Shaviv, N.J. et al., 2014, ApJ, 789, 104

Pastorello, A.; Zampieri, L.; Turatto, M. et al., 2004, MNRAS, 347, 74

Pastorello, A.; Della Valle, M.; Smartt, S.J. et al., 2007, Nature, 449, 1

Pastorello, A.; Mattila, S.; Zampieri, L.; et al., 2008, MNRAS, 389, .113

Pastorello, A.; Botticella, M. T.; Trundle, C. et al., 2010, MNRAS, 408, 181

Pastorello, A., 2012, MSAIS, 19, 24

Pastorello, A.; Cappellaro, E.; Inserra, C. et al., 2013, ApJ, 767, 1P

Pastorello, A.; Kochanek, C.S.; Fraser, M. et al., 2018, MNRAS, 474, 197

Pejcha, O.; Metzger, B.D.; Tyles, J.G.; Tomida, K., 2017, ApJ, 850, 59

Pignata, G.; Maza, J.; Hamuy, M. et al., 2009, RMXAC, 35R, 317

Porter, Alain C.; Filippenko, Alexei V., 1987, AJ, 93, 1372

Prieto, J.L.; Kistler, M.D.; Thompson, T.A. et al., 2008, ApJ, 681, 9

Pumo, M.L.; Turatto, M.; Botticella, M.T. et al., 2009, ApJ, 705, 138

Reguitti, A.; Pastorello, A.; Pignata, G. et al., 2018, arXiv, 1806.08343

Reichart, D.; Nysewander, M.; Moran, J. et al., 2005, NCimC, 28, 767

Richardson, D.; Jenkins, R.L; Wright, J.; Maddox, L., 2014, AJ, 147, 118

Roming, P.W.A.; Pritchard, T.A.; Prieto, J.L. et al., 2012, ApJ, 751, 92

Schlafly, E.F.; Finkbeiner, D.P., 2011, ApJ, 737, 103

Schlafly, E.F.; Green, G.M.; Lang, D. et al., 2018, ApJS, 234, 39

Schlegel, E.M. 1990, MNRAS, 244, 269

Smartt, Stephen J. 2009, ARA&A, 47, 63S

Smith, N.; Hartigan, P., 2006, ApJ, 638, 1045

Smith, N.; Li, W.; Foley, R.J.; et al., 2007, ApJ, 666, 1116

Smith, N.; Miller, A.; Li, W.; Filippenko, A.V.; et al., 2010, AJ, 139, 1451

Smith, N.; Li, W.; Miller, A.A.; Silverman, J.M. et al., 2011, ApJ, 732, 63

Smith, N.; Filippenko, A.V.; Li, W. et al., 2011, MNRAS, 415, 773

Smith, N.; Cenko, S.B.; Butler, N. et al., 2012, MNRAS, 420, 1135

Smith, N., 2014, ARA&A, 52, 487

Smith, N.; Andrews, J.E.; Mauerhan, J.C. et al., 2016, MNRAS, 455, 3546

Smith, N., 2017, RSPTA, 3756, 268

Soker, N.; Tylenda, R., 2003, ApJ, 582, 105

Soker, N.; Tylenda, R., 2006, MNRAS, 373, 733

Spiro, S.; Pastorello, A.; Pumo, M. et al., 2014, MNRAS, 439, 2873

Stathakis, R.A.; Sadler, E.M., 1991, MNRAS, 250, 786

Taddia, F.; Sollerman, J.; Pastorello, A. et al., 2015, A&A, 580, 131

Tammann, G.A.; Sandage, A., 1968, ApJ, 151, 825

Tartaglia, L.; Pastorello, A.; Taubenberger, S. et al., 2015, MNRAS, 447, 117

Tartaglia, L.; Pastorello, A.; Sullivan, M. et al., 2016, MNRAS, 459, 1039

Taubenberger, S., 2017, HSN, 317

Theureau, G.; Hanski, M.O. et al., 2007, A&A, 465, 71

Thompson, T.A.; Prieto, J.L.; Stanek, K.Z. et al., 2009, ApJ, 705, 1364

Theureau, G.; Bottinelli, L. et al., 1998, A&AS, 130, 333

Thöne, C.C.; de Ugarte Postigo, A.; Leloudas, G. et al., 2017, A&A, 599, 129

Tomasella, L.; Cappellaro, E.; Fraser, M. et al., 2013, MNRAS, 434, 1636

Tully, R.B.; Courtois, H.M.; Sorce, J.G., 2016, AJ, 152, 50

Turatto, M.; Cappellaro, E.; Danziger, I.J. et al., 1993, MNRAS, 262, 128

Turatto, M., 2003, LNP, 598, 21

Tylenda, R.; Hajduk, M.; Kamiński, T.; et al., 2011, A&A, 528, 114

Utrobin, V.P.; Chugai, N.N., 2011, A&A, 532, 100

Valenti, S.; Pastorello, A.; Cappellaro, E. et al., 2009, Nature, 459, 674

Valenti, S.; Howell, D.A.; Stritzinger, M.D. et al., 2016, MNRAS, 459, 3939

Van Dyk, S.D.; Filippenko, A.V.; Peng, C.Y. et al., 2000, PASP, 112, 1532

Van Dyk, S.D.; Filippenko, A.V.; Chornock, R. et al., 2005, AAS, 206, 5101

Van Dyk, S.D.; Li, W.; Filippenko, A.V.; Humphreys, R.M. et al., 2006, astro-ph, 3025

Van Genderen, A.M.; Sterken, C.; De Groot, M., 1997, A&A, 318, 81

Wagner, R.M.; Vrba, F.J.; Filippenko, A.V. et al., 2004, PASP, 116, 326

Weis, K.; Bomans, D.J., 2005, A&A, 429L, 13

Wolf, B., 1989, ASSL, 157, 91

Woosley, S.E.; Blinnikov, S.; Heger, A., 2007, Nature, 450, 390

Zampieri, L.; Colpi, M.; Shapiro, S.L.; Wasserman, I., 1998, ApJ, 505, 876